INDUSTRIAL PROCESSING OF AN Al-Zn-Mg-Cu POWDER METALLURGY ALLOY

by

Matthew David Harding

Submitted in partial fulfilment of the requirements
for the degree of Doctor of Philosophy

at

Dalhousie University
Halifax, Nova Scotia
December 2017

Dedicated to my beautiful daughter, Isla.
You've brought more joy to my life than I ever could have imagined.

TABLE OF CONTENTS

List of Tables ..... **vi**

List of Figures ..... **viii**

Abstract ..... **xi**

List of Abbreviations and Symbols Used ..... **xii**

Acknowledgements ..... **xv**

Chapter 1: Introduction **1**

Chapter 2: Background **4**

2.1 Aluminum and its Alloys 4

2.1.1 7xxx Series Wrought Aluminum Alloys 5

2.1.2 Precipitation Hardening in 7xxx Series Aluminum Alloys 6

2.2 Powder Metallurgy Processing 9

2.2.1 Compaction 10

2.2.2 Sintering 15

2.2.2.1 Liquid Phase Sintering 19

2.2.3 Aluminum Powder Metallurgy 22

2.3 Secondary Processing 24

2.3.1 Sizing 24

2.3.2 Shot Peening 26

2.4 Residual Stress 31

2.4.1 Utilizing Diffraction for Stress Measurement 31

2.4.2 X-Ray Diffraction 34

2.4.3 Neutron Diffraction 39

Chapter 3: Effects of Shot Peening on Aluminum Powder Metallurgy Alloys **43**

3.1 Forward to Chapter 3 43

3.2 Abstract 44
3.3 Introduction 44
3.4 Materials 46
3.5 Experimental Techniques 47
3.6 Results and Discussion 50
3.6.1 Surface Characterization 50
3.6.2 Fatigue Testing 54
3.7 Conclusions 59
3.8 Acknowledgments 59

Chapter 4: Characterization of the Microstructure, Mechanical Properties, and Shot Peening Response of an Industrially Processed Al-Zn-Mg-Cu PM Alloy 60

4.1 Forward to Chapter 4 60
4.2 Abstract 61
4.3 Introduction 61
4.4 Materials 63
4.5 Experimental Techniques 64
4.6 Results and Discussion 68
4.6.1 Characterization of T6 Specimens 68
4.6.1.1 Physical and Mechanical Properties 68
4.6.1.2 Microstructural Attributes 70
4.6.2 Effects of Shot Peening 77
4.6.2.1 Surface Assessment 78
4.6.2.2 Surface Residual Stress Measurements 81
4.6.2.3 Through Thickness Residual Stress 82
4.7 Conclusions 90
4.8 Acknowledgements 91

Chapter 5: Effects of Post-Sinter Processing on an Al–Zn–Mg–Cu Powder Metallurgy Alloy 92

5.1 Forward to Chapter 5 92

5.2 Abstract 93

5.3 Introduction 93

5.4 Materials and Methods 97

5.5 Results and Discussion 101

5.5.1 Effects of Sizing on Physical Properties 101

5.5.2 Effects of Sizing on Mechanical Properties 105

5.5.2.1 Hardness 105

5.5.2.2 Fatigue Testing 115

5.5.2.3 Effects of Shot Peening 120

5.5.3 Effects of Thermal Exposure 120

5.6 Conclusions 124

5.7 Acknowledgments 125

Chapter 6: Fatigue Fracture Assessment 126

Chapter 7: Conclusions and Future Work 131

7.1 Suggested Future Work 135

References 139

Appendix A: Copyright Release 144

MPIF Release (Chapter 3) 144

Elsevier Release (Chapter 4) 145

LIST OF TABLES

Table 2-1 Wrought aluminum alloy series. 5

Table 2-2 Chemical compositions of common 7xxx series alloys (wt%) [4]. 6

Table 2-3 Heat treatment designations for aluminum alloys. 8

Table 2-4 Mechanical properties of AA7075 [4]. 9

Table 2-5 Chemical compositions of AC2014, A6061 [8] and PM7075 [3], wt%. 23

Table 2-6 Mechanical properties of AC2014, A6061 [8] and PM7075 [3]. 23

Table 2-7 Mechanical properties of AA2219 (Al-6.3Cu-0.30Mg-0.18Zr-0.10V-0.06Ti) [4]. 25

Table 3-1 Chemical compositions of PM7075 and wrought AA7075 wt%. 46

Table 3-2 Surface roughness for various surface finishes. 55

Table 3-3 Fatigue comparison of wrought AA7075 to peened PM7075 aluminum alloys at various probabilities of failure. 58

Table 4-1 Targeted and measured chemistries of PM7075 (weight %). 64

Table 4-2 Tensile properties of lab and industrially produced specimens of PM7075-T6. 70

Table 4-3 In-plane residual stresses measured at the surface of PM7075-T6 specimens processed with and without shot peening. 81

Table 4-4 Summary of the normal strains and the corresponding measurement depths within peened PM7075-T6 found using Cu and Co radiation. 86

Table 5-1 Measured assays of the raw materials utilized (weight %) relative to the nominal targeted chemistries. 98

Table 5-2 Summary of the post-sinter processing sequences considered. 99

Table 5-3 Summary of the precipitation events observed in Sol-Size and Size-Sol processed specimens. 108

Table 5-4 Summary of the precipitation events observed in Sol-Size-Age and Size-Sol-Age processed specimens. 112

Table 5-5 Fatigue strength of PM7075 after the application of Sol-Age, Sol-Size-Age, and Size-Sol-Age processing. 116

Table 5-6 Fatigue strength of wrought AA7075 processed to Sol-Age and Sol-Size-Age conditions. 119

Table 5-7 Effect of shot peening on the fatigue strength of Size-Sol-Age processed specimens of PM7075. 120

Table 5-8 Effects of thermal exposure (1000 h at indicated temperature) on the tensile properties of PM7075 initially processed into the Sol-Age condition. 122

Table 5-9 Fatigue strength of thermally exposed PM7075 Size-Sol-Age and Size-Sol-Age-Peen. 123

LIST OF FIGURES

Figure 1-1 Aluminum usage in 2015 Ford F150 [2]. 2

Figure 2-1 Die compaction [6]. 11

Figure 2-2 Use of multiple punches to achieve a more uniform green density during compaction [6]. 12

Figure 2-3 - Stages of powder compaction (adapted from [6]). 13

Figure 2-4 Density gradients common in die compaction [6]. 14

Figure 2-5 Effect of Height/Diameter on density gradient [6]. 14

Figure 2-6 Stages in microstructure evolution during solid-state sintering [6]. 16

Figure 2-7 Grain movement and pore isolation during sintering [6]. 19

Figure 2-8 Theoretical phase diagram indicating liquid phase sintering [7]. 20

Figure 2-9 Stages during persistent liquid phase sintering [7]. 21

Figure 2-10 Density versus sintering time, showing PLPS stages [7]. 22

Figure 2-11 Plastic deformation caused by shot peening. 27

Figure 2-12 Typical residual stress profile resulting from shot peening. 28

Figure 2-13 Almen intensity measurement [9]. 30

Figure 2-14 Changes to lattice spacing due to residual stresses. 32

Figure 2-15 Surface stresses during XRD residual stress measurements [10]. 35

Figure 2-16 X-ray diffraction geometry with ψ-inclination during stress measurements. 36

Figure 2-17 Single crystal monochromator used during ND measurements. 40

Figure 3-1 Components of the system utilized in the shot peening of aluminum PM bars, (a) peening cabinet and (b) automated system. 48

Figure 3-2 SEM imaging of peened surfaces prepared at various intensities, (a) unpeened, (b) 0.25 mmN, (c) 0.4 mmN and (d) 0.2 mmA 51

Figure 3-3 Surface topography of aluminum PM7075 – T6 (a) unpeened, and (b) peened to 0.4 mmN. 52

Figure 3-4 Surface roughness of as sintered PM 431D and peened to intensities of 0.25 mmN, 0.4 mmN and 0.2 mmA. 53

Figure 3-5 Cross-sections of peened surfaces, (a) Unpeened, (b) 0.25 mmN, (c) 0.4 mmN, and (d) 0.2 mmA. PSEF shown by arrow. 54

Figure 3-6 Profile scan of fatigue bars, (a) as machined, (b) polished, and (c) peened to 0.4 mmN intensity. 55

Figure 3-7 Surface scan of a fatigue bar radius peened to 0.4 mmN intensity. 56

Figure 3-8 Surface roughness around the circumference of fatigue bar. 57

Figure 4-1 SEM image of PM7075 raw powder. 64

Figure 4-2 Variation in the average apparent hardness over the surface of PM7075-T6. All values reported in the HRB scale. 69

Figure 4-3 Core microstructure of industrially processed PM7075-T6. 71

Figure 4-4 Through thickness variations in the concentrations of (a) zinc, (b) magnesium, (c) copper, and (d) tin within an industrially produced puck of PM7075-T6. 74

Figure 4-5 Hardness profile recorded at the centre of a puck of PM7075-T6 from the top surface (0 mm) inward. 75

Figure 4-6 XRD trace for PM7075-T6. 76

Figure 4-7 Comparison on the {422} diffraction peaks recorded from the central and surface regions of PM7075-T6 puck. 77

Figure 4-8 General surface appearance of PM7075-T6 (a) before (b) after shot peening. 79

Figure 4-9 Subsurface microstructure of heat treated (a) and peened (b) PM7075-T6. 80

Figure 4-10 Hardness profile recorded at the centre of a shot peened puck of PM7075-T6 from the top surface (0 mm) inward. Specimen was peened to 0.4 mmN intensity. 80

Figure 4-11 In-plane and normal strains measured in shot peened PM7075-T6. 83

Figure 4-12 Normal component of strain measured in shot peened PM7075-T6. The first two points correspond to XRD data and the remainder to ND data. 87

Figure 4-13 Residual stress depth profile determined for shot peened PM7075-T6. 90

Figure 5-1 Effect of sizing pressure on % reduction in thickness for Sol-Size-Age and Size-Sol-Age processing sequences. 103

Figure 5-2 Effect of sizing pressure on surface roughness for Sol-Size-Age and Size-Sol-Age processing sequences. 104

Figure 5-3 Effect of sizing pressure on apparent hardness for Sol-Size-Age and Size-Sol-Age processing sequences. 105

Figure 5-4 DSC (differential scanning calorimetry) scans recorded from samples of PM7075 (a) immediately after Sol-Size and (b) immediately after Size-Sol processing. 107

Figure 5-5 DSC scans recorded from samples of PM7075 after (a) Sol-Size-Age and (b) Size-Sol-Age processing. 111

Figure 5-6 Bright field (BF) TEM images of (a) Sol-Size-Age and (b) Size-Sol-Age processed samples with the beam closely aligned to the <112> zone axis. 113

Figure 5-7 Selected area diffraction patterns (SADPs) recorded from (a) Sol-Size-Age and (b) Size-Sol-Age processed samples with the beam closely aligned to the <112> zone axis. 114

Figure 5-8 Surface residual stress measured in PM7075 as a result of Sol-Size-Age and Size-Sol-Age processing. 118

Figure 5-9 XRD traces acquired from Sol-Age samples exposed to 80°C and 160°C for 1000 h. 122

Figure 5-10 Residual stress as a function of elevated temperature exposure for Size-Sol-Age-Peen samples. 124

Figure 6-1 Macroscopic fatigue fractures of Sol-Age and Size-Sol-Age samples. 127

Figure 6-2 Macroscopic fatigue fracture of two Sol-Size-Age samples. 127

Figure 6-3 Surface profiles of Sol-Age and Sol-Size-Age samples. 129

ABSTRACT

The industrial processing of a commercial 7xxx series aluminum powder metallurgy (PM) alloy was studied in this work. Key aspects considered included direct comparisons of laboratory and industrially processed specimens as well as the implementation of post-sinter operations in an effort to increase the mechanical properties of the material. These included sizing, heat-treatment, and shot peening. For the latter, an automated system was developed capable of applying various peening intensities in a controlled manner. A nominal peening intensity of 0.4 mmN was found to be appropriate.

Characterization of industrially processed pucks (100 x 75 x 17 mm) emphasized chemical analyses (bulk and localized measurements), sinter density measurements, tensile testing, fatigue testing, Rockwell and nanoindentation hardness, optical microscopy and SEM. Residual stresses were quantified by x-ray diffraction (XRD) and neutron diffraction (ND) when assessing the near-surface and sub-surface gradients of residual stress respectively. Industrial pucks experienced appreciable losses of Zn via evaporation in sintering. Ultimately, the Zn concentration dropped to 3.1 wt% near surface, before increasing and stabilizing at the bulk composition of 5.6 wt% approximately 3 mm deep into the product. The corresponding through thickness nanoindentation hardness ranged from ≈1.65 GPa at the surface stabilizing to ≈2.50 GPa at a depth comparable to that at which the Zn concentration stabilized. Nominal values for the sintered density (2.74 g/cm^3), Young's modulus (65 GPa), yield strength (459 MPa), ultimate tensile strength (465 MPa) and elongation to fracture (1.0%) were all in-line with previously published results for laboratory processed specimens, attesting to the scalability of the alloy for industrial applications. Peening to an intensity of 0.4 mmN resulted in strain hardening within a surface layer of the material, inducing a maximum compressive residual stress at the surface of 230 MPa, extending to a depth of 60-100 μm prior to transitioning to tensile stresses.

Sizing was incorporated within the post-sinter processing sequence to better represent industrial production of geometrically complex parts from the alloy. The metallurgical effects were principally studied through a combination of differential scanning calorimetry (DSC), transmission electron microscopy (TEM), XRD, and 3-point bending fatigue. In certain instances, sizing was applied directly after sintering and prior to the solutionization and aging stages of T6 heat-treatment. In others, sizing was applied as an intermediate step within heat treatment operations, after solutionizing but prior to artificial aging. Respectively, these two sequences were denoted as "Size-Sol-Age" and "Sol-Size-Age" processes. Application of the former yielded a product with a hardness of 85 HRB and fatigue strength of 228 MPa. As both values were well aligned with the properties of unsized T6 samples, it was concluded that sizing had a neutral impact on these particular attributes when applied in this manner. Interestingly, when the "Sol-Size-Age" process was applied, the apparent hardness (78 HRB) and fatigue strength (168 MPa) were reduced to a statistically significant extent. These declines were ascribed to the partial annihilation of quenched-in vacancies that subsequently altered the nature of precipitates within the finished product as supported by DSC and TEM findings. Research also confirmed that the alloy responded well to shot peening, as fatigue strength was increased to 294 MPa. However, thermal exposure at 80°C and 160°C reduced the fatigue performance to 260 MPa and 173 MPa respectively as a result of residual stress relaxation, and in the case of 160°C exposure, in-situ over-aging.

List of Abbreviations and Symbols Used

NSERC	Natural Sciences and Engineering Research Council of Canada
PM	Powder Metallurgy
wt%	weight percent
Al	Aluminum
Zn	Zinc
Mg	Magnesium
Cu	Copper
Cr	Chromium
Zr	Zirconium
AA	Aluminum Alloy
SSSS	Super Saturated Solid Solution
GP-zone	Guinier-Preston Zone
η’	Semi-coherent precipitate (precursor to η)
η	Incoherent precipitate ($MgZn_2$) formed in 7xxx series aluminum alloys
FCC	Face Centered Cubic
Tx	Heat Treatment Designation
SCC	Stress Corrosion Cracking
UTS	Ultimate Tensile Strength
YS	0.2% Offset Yield Strength
BHN	Brinell Hardness
MPa	Megapascal
E-C	Evaporation Condensation
LPS	Liquid Phase Sintering
PLPS	Persistent Liquid Phase Sintering
TLPS	Transient Liquid Phase Sintering
Si	Silicon
Sn	Tin

HRE	Rockwell Hardness E-scale
HRH	Rockwell Hardness H-scale
HRB	Rockwell Hardness B-scale
XRD	X-Ray Diffraction
ND	Neutron Diffraction
d	Crystallographic Interplanar Spacing
λ	Wavelength (of either x-ray or neutron beam)
θ	Angle of diffraction
{hkl}	Family of crystallographic planes
σ_{ij}	3D stress tensor
C_{ijkl}	Material elasticity tensor
ε_{ij}	3D strain tensor
I_x	The intensity of an x-ray after travelling through x distance of material
I_o	The initial intensity of an x-ray incident on matter
μ/ρ	Mass absorption coefficient of material
ρ	Density of material
Φ	Orientation of stress (σ_φ) relative to the principal stress (σ_1) direction
ψ	Orientation of the bisector of incident and diffracted x-ray relative to the sample normal
E_{hkl}	Young's modulus for the material with regards to the specific grain orientation {hkl}
ν_{hkl}	Poisson's ratio for the material with regards to the specific grain orientation {hkl}
XEC	X-ray elastic constants, S_1 and $½S_2$
CNBC	Canadian Neutron Beam Centre
NRU	National Research Universal reactor
MW	Megawatt
SAE	Society of Automotive Engineers
mmN	Almen peening intensity measured with a 'N' strip

mmA	Almen peening intensity measured with a ‘A’ strip (approximately 3x the intensity of using an ‘N’ strip)
SEM	Scanning Electron Microscope
S_a	Arithmetic mean height over a surface (measure of roughness)
PSEF	Peened Surface Extrusion Folds
R_a	Arithmetic mean height of a line (measure of roughness)
MPIF	Metal Powder Industries Federation
EPMA	Electron-Probe Micro-Analyzer
WDS	Wavelength Dispersive Spectroscopy
FWHM	Full Width Half Max
at%	Atomic Percent
Mo	Molybdenum
DSC	Differential Scanning Calorimetry
TEM	Transmission Electron Microscopy
ICP-OES	Inductively Coupled Plasma Optical Emission Spectrometry
TRS	Transverse Rupture Strength
BF	Bright Field
SADP	Selected Area Diffraction Pattern
<uvw>	Crystallographic Direction
S_q	Root mean squared variation in height over a surface (measure of roughness)
VRC	Vacancy Rich Clusters
Exo	Exothermic reaction
Endo	Endothermic reaction
σ_a (50%)	Fatigue strength with 50% pass rate
n	Number of samples

ACKNOWLEDGEMENTS

First and foremost, I'd like to thank my supervisor, Dr. Paul Bishop, for his continued support over the years. It was a long journey but without his patience and guidance, this would not have been possible. I'd also like to gratefully acknowledge the financial support provided by the Natural Sciences and Engineering Research Council of Canada (NSERC) through the postgraduate scholarship – doctoral program, without which the past few years would have been much more stressful financially.

Special thanks are in order to personnel at GKN Sinter Metals LLC, specifically Ian Donaldson and Rich Hexemer for their aide in preparing samples and providing an industrial focus to this work. Also, all the members within the Powder Metallurgy Research Group at Dalhousie over the years who provided feedback, support and insight into the work, most notably Randy Cooke.

Finally, the utmost thanks and gratitude to my family and friends who have helped over the course of my graduate program, and specifically my beautiful wife Julie, who's endless support and love makes it all worthwhile.

Chapter 1: Introduction

Aluminum alloys offer a very unique blend of physical and mechanical properties to engineers for use in structural applications. While the use of aluminum is relatively new on the world scale compared to other common metallic materials, industrial exploitation has grown steadily since its introduction in the late 1800's [1]. A principal advantage of aluminum alloys is their considerably high strength to weight ratio, allowing them to compete on a strength basis at room temperature with low-medium strength steels while maintaining approximately 1/3 the density of iron. This attribute resonates particularly well with the automotive sector given the continual push towards reduced greenhouse gas emissions now mandated by numerous governments (i.e. USA CAFE Standards). Here, the replacement of ferrous parts with aluminum counterparts and the concomitant weight savings is applied as a means to reduce vehicle weight, and in turn increase fuel economy (and to a lesser extent performance). This is perhaps most evident in the 2015 Ford F150, shown in Figure 1-1, where aluminum alloys make up 25% of the curb weight of the vehicle, representing a weight savings of ≈700lbs over the previous model [2].

While the benefits of reduced weight are substantial, the cost of aluminum is still an issue to overcome. Accordingly, net and near-net shape aluminum forming technologies are of considerable interest to automotive manufacturers. One increasingly popular option is Aluminum powder metallurgy (PM) as the relatively high raw material cost can be offset by the efficiency and high production rates of press-and-sinter processing. This concept is now leveraged in the high-volume serial production of growing list of components including camshaft bearing caps, transmission retainer plates, heat sinks, and planetary carriers to name but a few.

2015 F150 Crew Cab	Lbs. / Vehicle CY2015
Blocks	71
Heads	66
Other Engine	37
Transmission Cases	68
Other Transmission	12
Differential Carriers	17
Drive shafts & Yokes	7
Heat Exchangers	32
Heat Shields and Sinks	10
Wheels	72
Brakes	6
Steering	5
Closures	223
Body Sheet HT	281
Body Sheet NHT	96
Body Shapes	31
Body Tube	37
All other	9
Total	1080

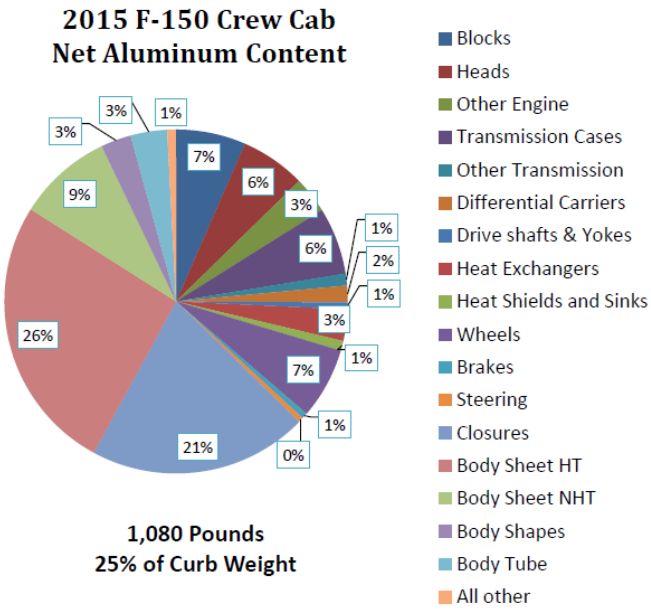

Figure 1-1 Aluminum usage in 2015 Ford F150 [2].

While aluminum PM processing is well accepted in the automotive industry, continued growth hinges on the implementation of alloys with increasingly higher mechanical properties that are competitive with a broader range of ferrous systems. To this end, a 7xxx series aluminum PM alloy based off the wrought system 7075 was devised. Denoted as Alumix 431D by the manufacturer (Kymera International, formerly Ecka Granules) and generally termed PM7075 throughout the entiriety of this work, laboratory studies have demonstrated that the system is responsive to PM processing, sinters to relatively high final density, and exhibits a tensile yield strength on the order of 450MPa in the T6 temper [3] While such traits are unquestionably promising, commercial inception of the alloy has yet to transpire due to an absence of data on the industrial press-sinter processing response of the alloy and how it responds to common post-sinter operations. Hence, the objective of this research was to develop data in these areas so as to establish a comprehensive understanding of the alloy and in turn, an accurate sense of its strengths and weaknesses under an industrial setting. In doing so,

emphasis was placed on an array of industrial compaction and sintering trials, as well as the incorporation of critical secondary processes including sizing, heat-treatment, and shot peening. Advanced means of material characterization were also applied including high magnification electron microscopy, thermal analyses, residual stress measurements, and multiple forms of fatigue testing. As exposure to moderate elevated temperatures are common in under-the-hood applications wherein the alloy could be expected to operate, the effects of thermal exposure were also considered.

Chapter 2: Background

2.1 Aluminum and its Alloys

Aluminum is the most abundant metallic element in the earth's crust. Its discovery was believed to have occurred between 1808-1812 by Sir Humphrey Davy of England with the first small scale production occurring in 1855 [1]. Burdened by inherently challenging thermodynamics, aluminum remained in limited production until the end of the 19th century until key advances in metal extraction technology emerged. Since then, aluminum has grown to be one of the most frequently used metals by weight, ranking only behind iron in global production; if measured by volume, the usage of aluminum now exceeds all other non-ferrous metals combined [1]. Aluminum has unique properties that suit it specifically to several industries, including transportation due to its high strength to weight ratio and lower cost compared to other materials such as titanium, and food processing and packaging due to its high resistance to corrosion and non-toxic properties. Typically, aluminum is combined with other elements to form alloys which can greatly increase mechanical properties. Common elements added include copper, manganese, silicon, magnesium, and zinc among others. Each element will alter the base aluminum in different ways, the complete structure with all added elements can compete with many other metals and still maintain a relatively light weight.

Aluminum and its alloys are usually used in either wrought or cast form. Wrought alloys are pre-formed products that typically require further fabrication. Higher strengths are attainable with wrought alloys over cast alloys, but fabrication is typically costlier with machining usually being required. Due to the increased mechanical properties of wrought products over cast, focus will be placed on comparing the PM system to its wrought counterpart.

The most widely used standard for alloy identification is that of the Aluminum Association, which employs different nomenclature for wrought and cast alloys. Wrought alloys use a four-digit system with the first digit representing the alloy group or "primary" alloying element (shown in Table 2-1), the second indicates modifications of the original alloy or impurity limits in the alloy, with the last two identifying the alloy or the system purity.

Table 2-1 Wrought aluminum alloy series.

Aluminum, 99.0% minimum and greater	1xxx
Aluminum Alloys Grouped by Major Alloying Elements	
Copper	2xxx
Manganese	3xxx
Silicone	4xxx
Magnesium	5xxx
Magnesium and Silicon	6xxx
Zinc	7xxx
Other Element	8xxx
Unused Series	9xxx

2.1.1 7xxx Series Wrought Aluminum Alloys

The material of interest during this work was of the 7xxx series. The major alloying element in 7xxx series alloys is zinc, with magnesium and copper also commonly playing very important roles, with some of the highest strength aluminum alloys (at room temperature) belonging to the aluminum-zinc-magnesium-copper family. Table 2-2 shows the chemical compositions for some common members of this series.

Table 2-2 Chemical compositions of common 7xxx series alloys (wt%) [4].

Alloy	%Zn	%Mg	%Cu	%Cr	%Other
7001	7.4	3.0	2.1	0.26	--
7050	6.2	2.2	2.3	--	0.12 Zr
7075	***5.6***	***2.5***	***1.6***	***0.23***	***--***
7475[1]	5.6	2.5	1.6	0.23	--

1 – 7475 has the same chemical composition as 7075, but lower impurity limits.

The PM system considered throughout this study was designed as a PM counterpart to aluminum alloy (AA)7075, which has very high strength and is typically used for highly stressed parts where weight is of primary concern. This leads AA7075 to be commonly used in the aerospace industry, specifically in aircraft structures and fittings. Although corrosion resistance is less then 5xxx and 6xxx alloys it exceeds that of 2xxx, which leads to its use in high stressed components where corrosion can be an issue. It is also typically bolted or riveted since the alloy is not considered to be weldable.

2.1.2 Precipitation Hardening in 7xxx Series Aluminum Alloys

Certain aluminum alloy systems can benefit from substantial gains in strength caused by precipitation hardening. These heat-treatable systems rely on the formation of a fine network of a secondary phase (precipitates) within the aluminum matrix upon thermal treatment. These precipitates will interfere with dislocation movement within the aluminum matrix during deformation, resulting in increased strength, while ductility of the system will typically decrease. AA7075 is heat-treatable, with the primary strength gains coming from the formation of $MgZn_2$ precipitates, through the reaction outlined in Eq 2-1:

$$SSSS \rightarrow GP\ Zone \rightarrow \eta' \rightarrow \eta\ (MgZn_2) \qquad (Eq\ 2-1)$$

The first requirement in the heat-treatment is to dissolve alloying additions (Zn, Mg, Cu) in the aluminum matrix. Due to the solubility limits of these elements, this requires raising the temperature of the component to a point where the solvent atoms (Zn, Mg, Cu) will dissolve in the solute (Al) matrix, thereby creating a solid solution. For AA7075 this requires stabilization of the component in the range of 470°C. Once the component is homogenized at this temperature, it is then quenched in water in an effort to preserve the solid solution at room temperature and thereby create a non-equilibrium super-saturated solid-solution (SSSS). At this point, the concentrations of dissolved solvent atoms exceed their respective saturation limits in aluminum, and will spontaneously precipitate out of the base matrix. Depending on the kinetics of this reaction and the desired nature of precipitates, the material may be naturally aged, meaning it is held at ambient temperature for a period of time to allow precipitation to take place. Alternatively, it may be re-heated to a moderate temperature to expedite the precipitation reaction; a process termed artificial aging. The precipitates within aluminum alloys will typically progress through various stages akin to Eq 2-1. In the case of 7xxx series alloys, the precipitate reaction commences with GP Zone formation, characterized by the migration and grouping of solvent atoms within the aluminum matrix. At this point the atoms remain in solid solution and are thought to retain the underlining aluminum lattice structure of face centered cubic (FCC). With continued aging, the Zn and Mg atoms begin to coalesce to form semi-coherent η' particles with a composition close to MgZn and thin-disc shape [1]. With increased ageing, the incoherent η precipitate will eventually form with a composition of $MgZn_2$. Although this is the traditional precipitation reaction believed to occur in 7xxx series aluminum, this model is highly contested and has been revised by several researchers which will be discussed in Section 5.3.

The four-digit alloy identification code is invariably followed by hyphenated designation that indicates the nature of the final processing applied. In many instances, this refers to a prescribed heat treatment. Generally shown as Txx, there are several subdivisions that identify how the heat treatment was accomplished as listed in Table 2-3.

Table 2-3 Heat treatment designations for aluminum alloys.

Temper	Process
T1	Cooled from fabrication temperature and naturally aged
T2	Cooled from the fabrication temperature, cold worked, and naturally aged
T3	Solution-treated, cold-worked, and naturally aged
T4	Solution-treated and naturally aged
T5	Cooled from the fabrication temperature and artificially aged
T6	Solution-treated and artificially aged
T7	Solution-treated and stabilized by overaging
T8	Solution-treated, cold-worked, and artificially aged
T9	Solution-treated, artificially aged, and cold-worked
T10	Cooled from the fabrication temperature, cold-worked, and artificially aged

In the case of AA7075, the maximum strength of the material is usually obtained after a T6 treatment, with precipitation having progressed to a point dominated by GP Zone/η' formation. With further progression along the precipitation reaction (as completed through T7 tempering), to the point of η formation, the material is in an overaged state, with slightly reduced strengths when compared to a T6 product. The T7 temper is commonly encountered, especially in aerospace applications, as a T6 product will suffer from an increase in stress corrosion cracking (SCC) as a result of sustained stress, either from stable loads in service or residual stresses within the component along with a corrosive environment. As this work focuses on an aluminum PM alloy of similar

composition to 7075, Table 2-4 shows the mechanical properties of AA7075 in various tempers.

Table 2-4 Mechanical properties of AA7075 [4].

Alloy-Temper	UTS (MPa)	YS (MPa)	Elongation (%)	Hardness (BHN)[1]	Fatigue Life (MPa)[2]
7075-0	230	105	17	60	115
7075-T6	570	505	11	150	160
7075-T73	505	435	13	--	150

1 – 500kg load, 10mm ball
2 – 500 000 000 cycles reversed stress R.R. Moore type machine

2.2 Powder Metallurgy Processing

PM is a fast-growing fabrication technique that can offer significant cost savings when compared to other more traditional metal forming means such as machining, forging and casting. In this process metal powder is used as the raw stock which is ultimately formed into a coherent final product. This can be accomplished by a number of means but always involves high pressure and heat to form the final solid product. The economical savings come from the process producing near-net shape components that typically require little to no machining or secondary operations, along with very high production rates in traditional press-and-sinter processing. There is also very high material utilization during the PM process, with approximately 97% of the starting powder converted to the final product [5].

Where the aerospace industry was the main target for new developments of traditional aluminum, the automotive industry is largely targeted for utilization of aluminum PM. The automotive sector would benefit greatly from the weight savings that aluminum can offer over steel and they maintain the high volume required for press-and-sinter PM

production to be economical, whereas the aerospace industry deals with significantly lower production numbers.

There are several means that powder may be formed to a final product, the following will outline the conventional, most widespread method - die compaction followed by sintering.

2.2.1 Compaction

Typically, it is desired to produce a final component with maximum density, as this is generally synonymous with the highest mechanical properties. The first step in densification of the bulk powder is shaping and compaction. This produces a “green compact” which is strong enough for handling, while still of a chalk-like consistency and has the approximate shape of the final product. The most common method of compaction (and that considered in this study) is die compaction. Other forms include injection molding, isostatic pressing and direct powder forging.

During die compaction, powder is pressed uni-axially in rigid tooling under pressures commonly ranging from 100-700 MPa. The tooling (die, punches, core rods, etc.) required is typically very expensive and of material with exceptional wear resistance. The cyclic rubbing of powder on tooling surfaces amounts to a very abrasive environment, which often mandates highly durable materials such as tool steels and tungsten carbide in tooling fabrication. Typically, compaction is achieved by means of “double action die compaction” as depicted in Figure 2-1. Here, pressure is applied to the powder from both the bottom and top punches, opposed to single action compaction,

wherein pressure is only be applied from one direction. The advantage of double action compaction will be discussed later in the section.

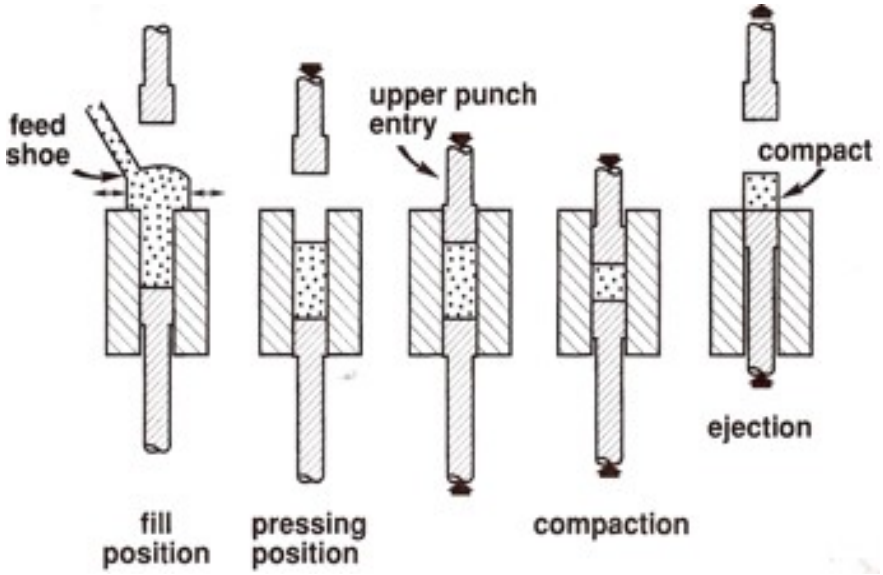

Figure 2-1 Die compaction [6].

When the complexity of the component increases, sections of different thickness are frequently encountered. In such scenarios, multiple punches are generally required to apply different pressures to the separate sections in order to obtain a more uniform density throughout the component as illustrated in Figure 2-2.

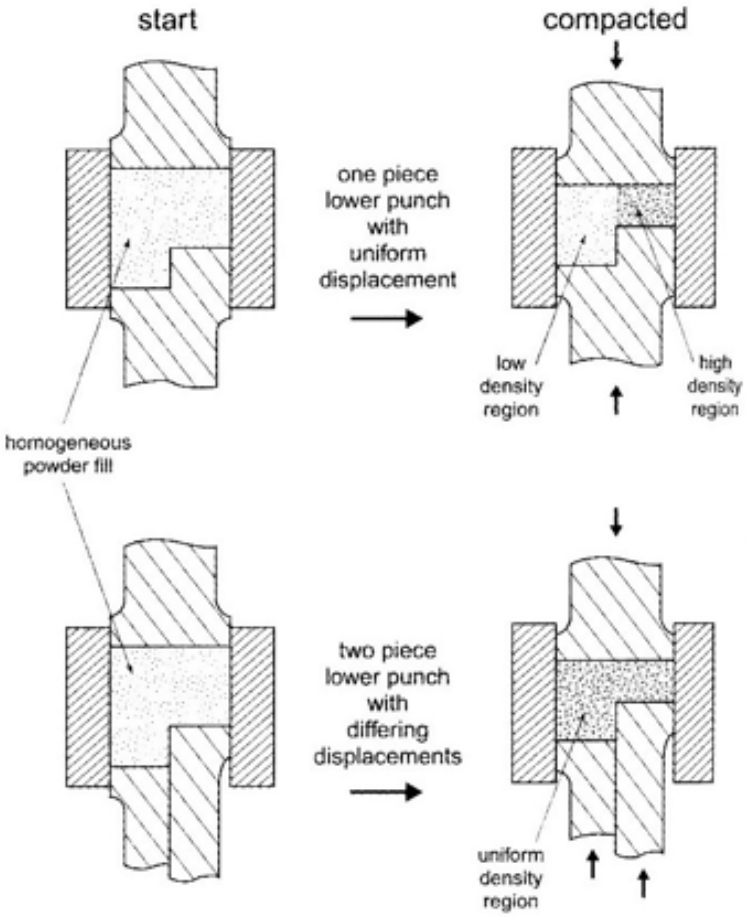

Figure 2-2 Use of multiple punches to achieve a more uniform green density during compaction [6].

During the pressing of the powder, there are several stages that occur. Figure 2-3 is a graphical representation of these, starting with the bulk powder itself (i.e. apparent density) and finishing with a green compact of maximum density. During rearrangement, particles are forced together with the finer particles filling the voids between those that are coarser in size. Individual contact points between the particles then begin to plastically deform, increasing contact area between particles thereby giving rise to localized deformation. During homogeneous deformation, the entire powder particles begin to deform. For example, spherical particles would begin to take on polygonal shapes, further increasing contact area. The powder compact then starts to behave as a

solid body, which can only undergo bulk compression. Minimal deformation and densification occurs during this final stage. The resultant green body typically exhibits a final density ranging from 90 to 95% of full theoretical density in the case of aluminum powders.

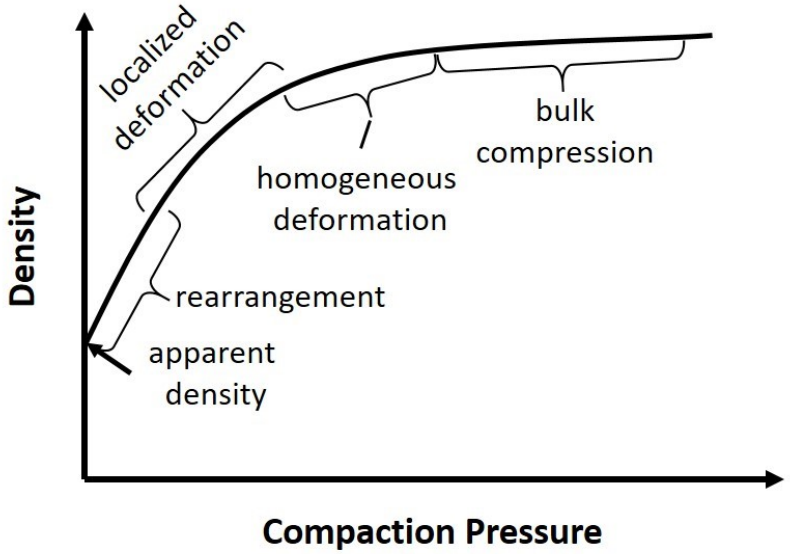

Figure 2-3 - Stages of powder compaction (adapted from [6]).

A very significant issue in die compaction is the presence of density gradients within the formed green body. This is a result of die wall and punch face friction. Figure 2-4 shows a typical density gradient within a pressed green body. This example is copper powder with density units of g/cm^3. This also reveals the difference between single and double action compaction, in that double action imparts a more homogenous green density throughout the product. Indeed, density gradients become increasingly problematic when attempting to press long, narrow components. Figure 2-5 shows the effect of Height/Diameter on the density gradient present in a component pressed in single action die compaction.

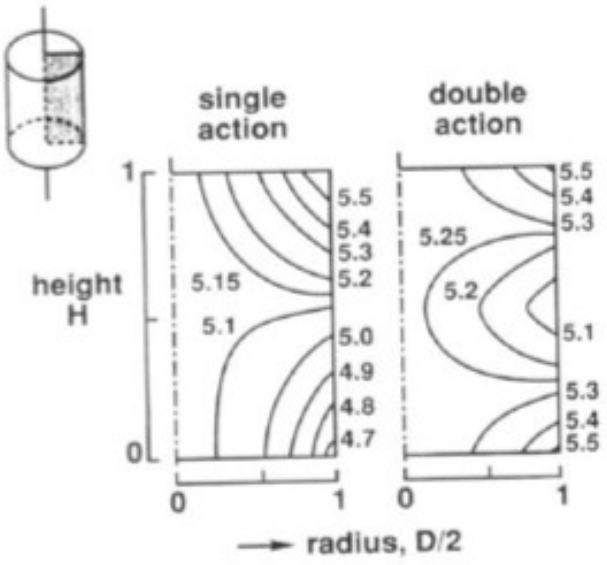

Figure 2-4 Density gradients common in die compaction [6].

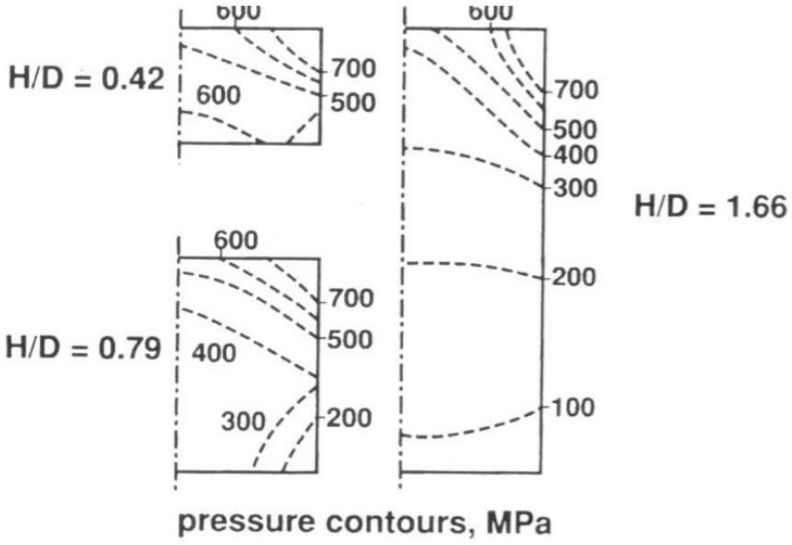

Figure 2-5 Effect of Height/Diameter on density gradient [6].

In an effort to reduce the density gradient present in a compact, lubrication is typically applied. This can be added mainly in two forms, the most common is by mixing a powdered lubricant into the powder mixture, while a second option is coating the die walls with a sprayed-on lubricant. In an industrial setting, it is rather complex and costly to apply a lubricant coating on the die walls between each component press, which is

why a powdered lubricant addition is more commonly utilized. In use, the powdered lubricant melts due to frictional heat generated between the powder and die wall. This liquid then reduces the coefficient of friction between the powder and the die wall so as to improve green density uniformity and extend tooling life. One down side to lubrication is that the addition can result in lower overall green densities when high compaction pressures are applied.

2.2.2 Sintering

Once a green body is formed, the next step in the PM process is sintering. Here, the individual powder particles are bonded to one another, which results in greatly improved mechanical properties. There are two main forms of sintering; namely, solid state and liquid phase. The main difference being that during the latter, a liquid is formed in the powder mixture, yet such a constituent is absent in the former.

The means by which the particles bond together during solid state sintering are mass transport mechanisms between adjacent powder particles, where mass from adjacent particles will shift and form a neck. This diffusion of material is thermally driven, with sintering temperatures typically ranging from 60 – 80% the materials melting point. When heating is applied to a green compact, diffusion is a result of the compact attempting to reduce its overall energy by reducing its surface area.

There are two key forms of mass transport that can occur during solid state sintering, surface transport and bulk transport. Surface transport results in atomic movement along the surfaces of both particles, accomplished by atoms moving into void locations. This will cause neck growth between particles, while particle spacing remains

unchanged (no densification occurs) [6]. The sub-mechanisms that enable the flux of atoms in this manner include evaporation-condensation (E-C), surface diffusion and volume diffusion. Surface diffusion dominates at low temperatures with evaporation-condensation also playing an important role, especially in low stability metals (e.g. lead). Bulk transport mechanisms involve volume diffusion, grain boundary diffusion and plastic flow. Here, mass is transported from the interior of a particle to the surface. Bulk transport also results in the compact shrinkage, which is due to a reduction in inter-particle porosity. Visually, the sinter process can be broken into three stages, initial, intermediate and final. The typical microstructures of a component observed during these three stages can be seen in Figure 2-6.

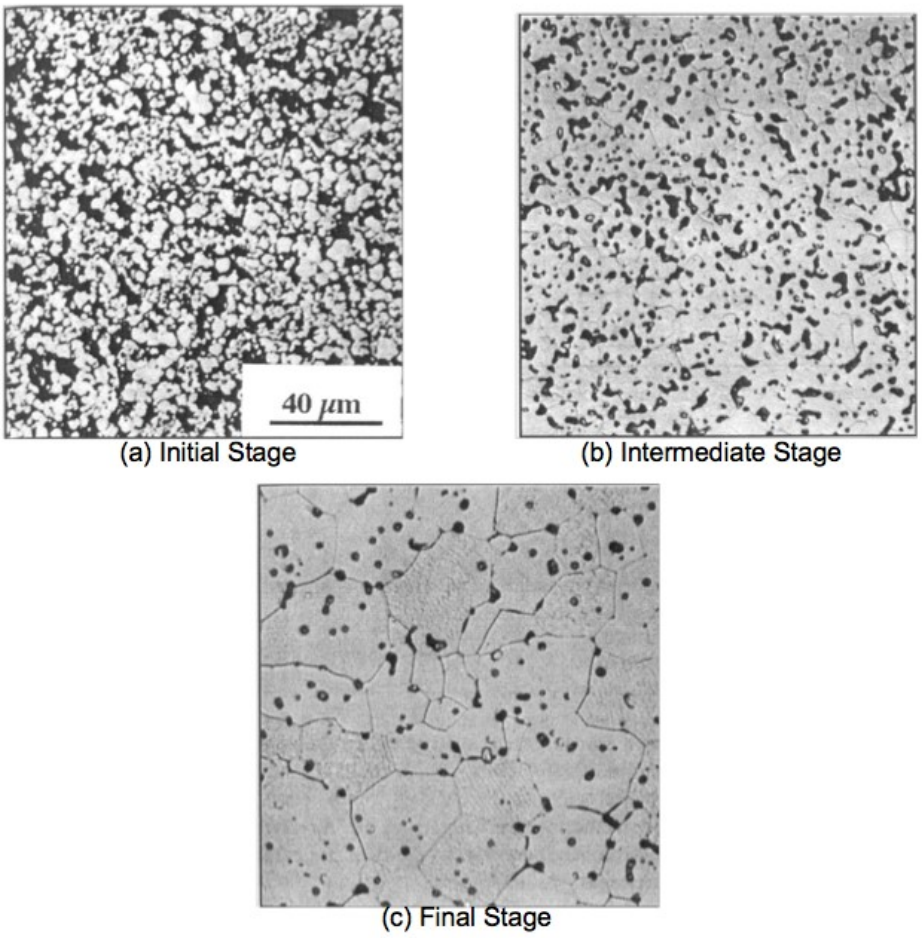

Figure 2-6 Stages in microstructure evolution during solid-state sintering [6].

From Figure 2-6 there is a significant amount of densification occurring between the initial stage and final stages. The main feature of the initial stage of sintering is neck formation between particles. All mass transport mechanisms occur during this process, yet E-C and surface diffusion are generally predominant. With regards to the former, all surfaces have a vapour pressure associated with them. However, when two particles are adjacent a relatively low pressure will exist in the contact area (concave neck) as compared to that present on the remainder of each particles exterior surface. This thereby establishes a pressure gradient, prompting the transport of vapour into the lower pressure neck region. As this “over-pressurizes” the region beyond its equilibrium condition, vapour will then condense and impart neck growth. During the sintering process, a common measurement in assessing the stage of sinter reached is the shape and size of the pores present. During the initial stage of sintering the pores are rather coarse and remain highly irregular in shape. At this point the compact is said to be “under sintered” and exhibits low strength.

The intermediate stage is typically considered to be the most important during the solid-state process. This stage is characterized by simultaneous pore rounding, grain growth and densification, which have a profound effect on the final properties of the component (especially densification). During the preceding initial stage, much of the curvature-induced gradients from neck formation are eliminated. The mechanisms effective during this stage deal with minimization of surface area and energy through changes in the pore structure within the microstructure. The pores present between powder particles can be thought of as regions with high concentrations of vacancies present. In an effort to reduce surface energy, these vacancies will migrate into the particles, being replaced by atoms (mass) flowing to fill the pore, which results in the pores shrinking and taking on a highly rounded shape, this causes an increase in density.

Compared to the initial and intermediate stages, the final stage is considerably slower, so much so that in press-and-sinter PM it is rarely attained during sintering of green compacts. At this point closed rounded pores are present at grain boundary intersections. As in the intermediate stage, the compact tries to reach a state of lower surface area and energy, but with much of the surface area eliminated other mechanisms begin to further densify the compact, mainly pore interaction along grain boundaries, termed “Ostwald Ripening”. Pores exist predominantly along grain boundaries as they effectively reduce the boundary area, resulting in a reduced energy state of the compact. The grain boundaries also act as a quick route for mass transport and thereby enable meaningful rates of pore elimination. Ostwald Ripening effectively leads to the larger pores growing while the smaller pores become smaller, resulting in a progressively higher density. However, as higher temperatures and/or longer sintering times are realized, grain growth will begin and can lead to the grains breaking away from the pores. Figure 2-7 describes how this occurs. With slow grain growth, the pore will begin to deform in an effort to remain affixed to the grain boundary (Figure 2-7 (b)). A pressure gradient is then developed given the differing states of curvature on the opposing flanks of the deformed pore. This causes E-C to diffuse molecules from the right side of the pore (the higher pressure surface) to the left side (lower pressure surface). Initially, this mass flux is sufficiently adequate for the pore to keep up with the advancing grain boundary. However, as the kinetics of grain growth increase, a point is reached where this is no longer the case and the grain boundary breaks away from the pore. When this occurs, densification ceases from a practical standpoint. During the final sinter stage, a microstructure similar to Figure 2-7 (c/d), could be reached.

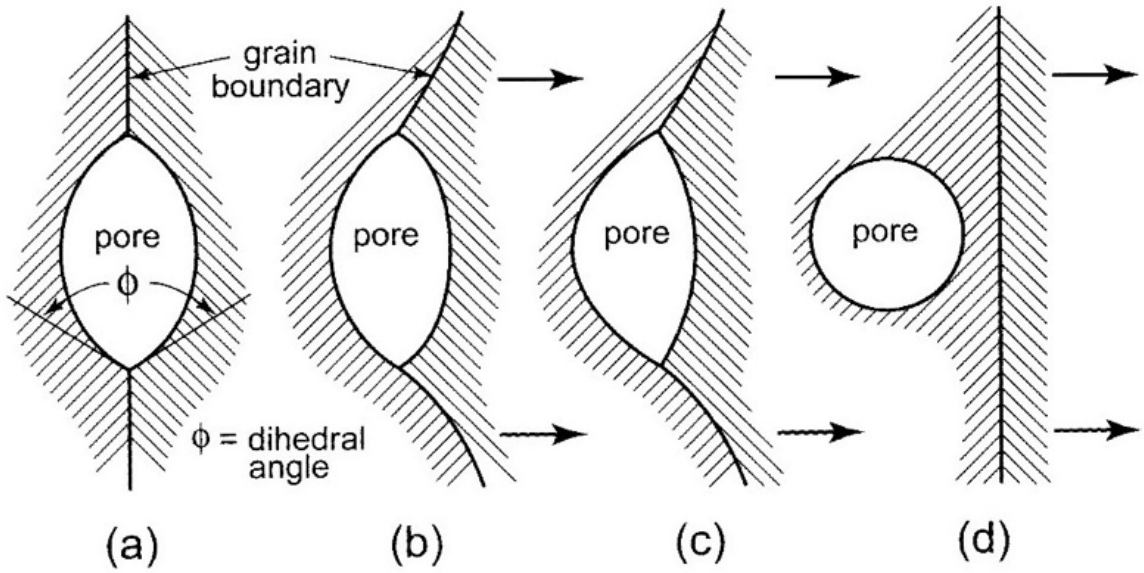

Figure 2-7 Grain movement and pore isolation during sintering [6].

2.2.2.1 Liquid Phase Sintering

During sintering, the means by which bonds are formed involve diffusion of material between particles, this is very critical for a properly sintered final product. If the diffusion rate is increased, the sintering rate can also be greatly increased, in an industrial setting this can be very beneficial and allow for a more homogeneous sinter in a shorter period of time. With liquid phase sintering (LPS) a liquid is formed during the sintering process. As diffusion is typically between 100-1000x faster through a liquid then a solid this can result in much more efficient and intense densification. While there are a number of different variants of LPS, two of those more commonly encountered are persistent liquid phase sintering (PLPS) and transient liquid phase sintering (TLPS). The “classical” liquid phase sintering is that of PLPS. During this process the liquid remains during the entirety of the sintering process, and solidifies as a separate phase upon cooling.

In order to form a liquid phase, typically there will be multiple powders present in the mixture with one having a relatively low melting point. Sintering takes place at a

temperature so the additive powder will form a liquid within the mixture, Figure 2-8 shows this on a theoretical phase diagram. There are three main requirements that must be met for this process to proceed effectively, which are, a high solubility of the solid in the liquid, low solubility of the liquid in the solid and the liquid must readily wet the solid (no beading). PLPS is often utilized when sintering refractory metals such as tungsten and molybdenum due to their high melting point, when dealing with hard to sinter metals such as aluminum or magnesium, and when enhanced densification is sought.

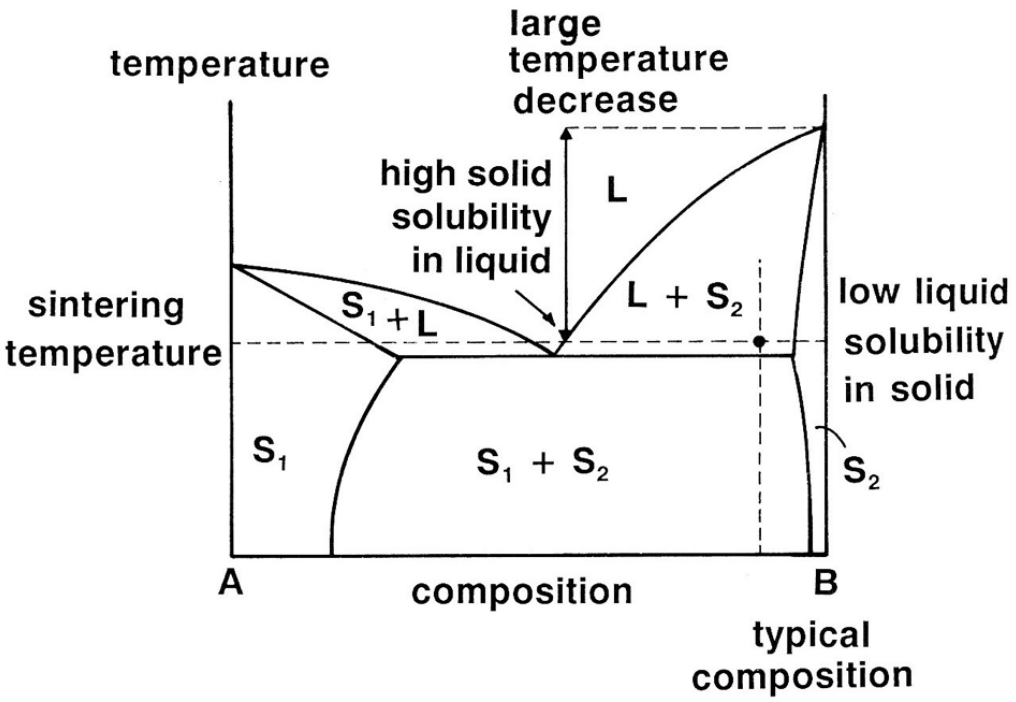

Figure 2-8 Theoretical phase diagram indicating liquid phase sintering [7].

There are four main stages during PLPS, heating, rearrangement, solution-reprecipitation, and final stage. An illustration of these can be seen in Figure 2-9 below. During the heating phase the lower melting point particles will begin to form a liquid, which will wet the solid particles. Once this occurs rearrangement of the solid particles will begin, this results in a burst of densification, as can be seen in Figure 2-10, showing

a graphical representation of compact density versus sintering time. During solution-reprecipitation the smaller grains will be dissolved in the liquid, which will then be reprecipitated onto the larger particles. As the larger grains grow, the contact area between adjacent particles will increase displacing liquid into the pore areas. During the final stage the main means for further densification is effectively that of solid state sintering between the contacting solid particles. The amount of liquid formed during the process is very critical, if too little liquid forms inadequate densification will be likely yet if too much liquid is present, it is possible for the compact to become excessively fluid to the point where the net shape of the component can be lost.

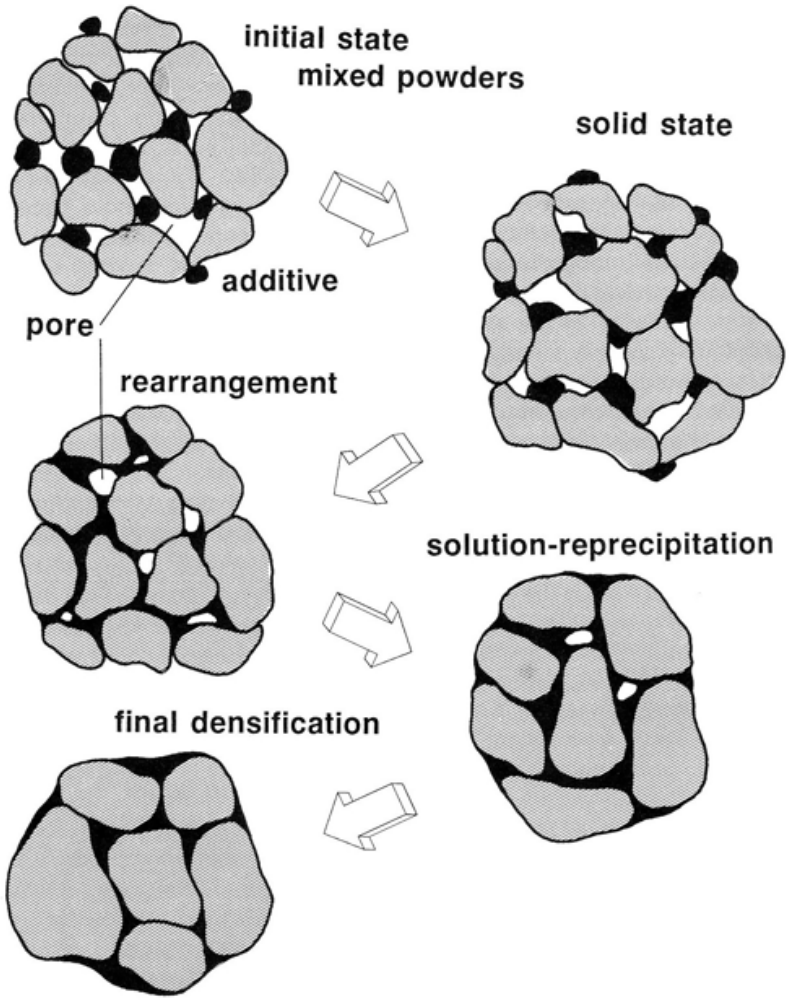

Figure 2-9 Stages during persistent liquid phase sintering [7].

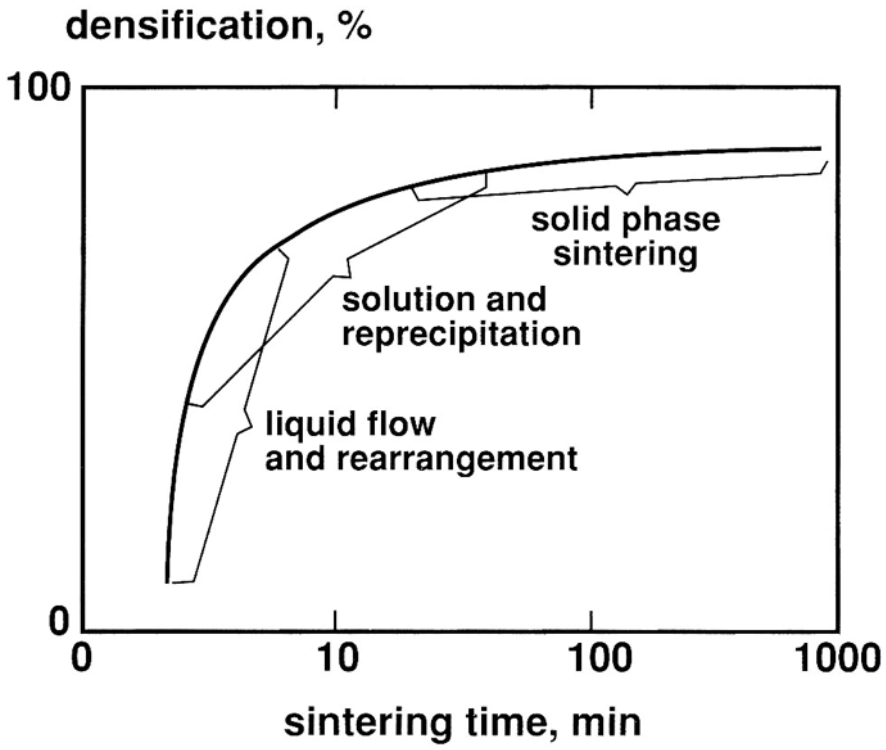

Figure 2-10 Density versus sintering time, showing PLPS stages [7].

TLPS differs from PLPS in that the liquid which is formed during heating does not remain during the entire sintering process. Here, the liquid has a high solubility within the solid particles. This means that as the sintering time is increased, the liquid will form a separate phase with the solid, with a resulting higher melting point, and in turn, solidification will occur.

2.2.3 Aluminum Powder Metallurgy

The use of aluminum PM has been dominated by two early material systems (AC2014 and A6061), designed for press-and-sinter processing and based off the wrought systems AA2014 and AA6061 respectively. With growing demand for aluminum PM components, much effort has been placed on developing new alloy compositions that offer improved mechanical/physical properties and can meet industry demands for a

growing list of new product opportunities. Ecka Granules (Velden, Germany), one of the world's largest manufacturers of aluminum metal powders, have developed a family of alloys (termed "Alumix" Alloys) to offer press-and-sinter processing with increased properties over the industry standard AC 2014 and A6061. Table 2-5 shows the chemical compositions of one of these Alumix alloys (denoted as grade 431D and generally termed PM7075 throughout this work) along with those of AC2014 and A6061 per ASTM. Typical mechanical properties of these same materials are provided in Table 2-6.

Table 2-5 Chemical compositions of AC2014, A6061 [8] and PM7075 [3], wt%.

PM Alloy	Al (min)	Cu	Mg	Si	Zn	Sn
AC2014	91.5	3.5-5.0	0.2-0.8	1.2 max	--	--
A6061	96.0	<0.5	0.4-1.2	0.2-0.8		
PM7075	balance	1.6	2.5	--	5.5	0.2

Table 2-6 Mechanical properties of AC2014, A6061 [8] and PM7075 [3].

PM Alloy (Temper)	Compaction Pressure (MPa)	Density (g/cm^3)	UTS (MPa)	Hardness	Elongation (%)
AC2014 (T1)	--	>2.6	172	55-60 HRE	3.0
AC2014 (T6)	--	>2.6	290	80-85 HRE	2.0
A6061 (T1)	--	2.45-2.6	128	80-85 HRH	6.0
A6061 (T6)	--	2.45-2.6	207	65-70 HRE	2.0
PM7075 (T1)	600	2.75	323	67 HRB	1.4
PM7075 (T6)	600	2.75	448	86 HRB	0.9

PM7075 (which is the focus of this work) is designed as a PM equivalent to the common high strength wrought alloy AA7075, with the addition of 0.2wt% Sn along with 1.5wt% lubricant. The lubricant included in PM7075 aides in powder compaction, increasing the green density of the compact and reducing the density gradients present as a result of uni-axial compaction. While the Sn addition in the alloy acts as a liquid forming

secondary phase during sintering, allowing for LPS to be achieved, greatly increasing the quality of the final sintered product.

2.3 Secondary Processing

Although PM produces a near net shape component, secondary operations after sintering are typically required to obtain the dimensional tolerances which are commonly demanded in components. There are also secondary operations utilized to increase the mechanical properties and performance of parts. Common processes include machining, grinding, sizing, repressing, and forging to name a few. As this work was undertaken to show the industrial feasibility of PM7075, care was taken to simulate an industrial process as closely as possible. For this reason, sizing was one critical secondary process incorporated, along with shot peening in an effort to increase the fatigue properties of the PM material.

2.3.1 Sizing

During LPS of aluminum green compacts, distortion will typically be present to some extent, either in the form of shrinkage in the part due to densification during sintering, or in some instances swelling can result. To achieve the tight tolerances required within final part geometry, sizing is completed to alleviate these sintered distortions within parts. Although sizing is incorporated in essentially all aluminum PM produced parts, there is virtually no literature available regarding the effects that sizing has, if any, on final part performance. Much of aluminum PM products produced industrially are in a T2 temper, with sizing applied to the sintered product once it has cooled to room temperature. Much of the effort in aluminum PM development emphasizes the use of precipitation hardening to increase the mechanical performance of aluminum PM

materials by means of applied heat treatments. Hence, the incorporation of sizing introduces an interesting challenge as the sequence of post-sinter events includes sizing in addition to the steps required for heat treating - solutionization, quenching and aging (either natural or artificial). When sizing is applied first and all heat treatment operations follow thereafter, the product temper would be the T4 or T6 condition (depending on whether natural or artificial aging was utilized). On the other hand, sizing could be included as an intermediate stage within the sequence of heat treatment operations. For instance, the sintered product could be solutionized and quenched, then sized, and finally, naturally or artificially aged. Under these sequences, the resultant temper is then either T3 or T8 (again, depending on the manner of aging). Industrially, sizing in the quenched state provides a few advantages versus sizing in the sintered (T1 state). The material is more malleable in the quenched state compared to the partially precipitation hardened T1 state, resulting in lowered press capacity. Also, by applying sizing following solutionization and quench, any quench induced distortion would be addressed. Deformation processing between quenching and artificial aging (T8 processing) has been shown to increase the mechanical properties of certain aluminum alloys and is widely used in industry. For example, the strengths of alloy AA2219 (Al-6.3Cu-0.30Mg-0.18Zr-0.10V-0.06Ti) in both the T62 and T87 tempers are shown in Table 2-7. Conversely, T8 processing of 7xxx series wrought alloys will affect the aging response of the material and generally result in lowered achievable strengths compared to T6 processing [4].

Table 2-7 Mechanical properties of AA2219 (Al-6.3Cu-0.30Mg-0.18Zr-0.10V-0.06Ti) [4].

Temper	UTS (MPa)	YS (MPa)	Elongation (%)	Hardness (BHN)
T62	415	290	10	115
T87	475	395	10	130

2.3.2 Shot Peening

Shot peening is a cold working technique mainly utilized to increase the fatigue properties of metallic materials. This is accomplished by impacting the surface of a component with a stream of spherical balls, termed “shot”. When impact occurs, the surface will plastically deform, inducing a thin compressive residual stress layer in the surface of the specimen. The process was first developed in the 1920’s and 1930’s concurrently in the United States and Germany. Engineers at Buick Automotive Company completed a great amount of early work in the 1930’s when it was noticed that shot blasting (used for cleaning a surface) resulted in increased fatigue strength.

Shot peening is based off shot blasting (or abrasive blasting) where so-called shot are propelled against the surface of a component. While the two processes are very similar, the intent is different in that shot peening is utilized to plastically deform the surface layer, whereas shot blasting is used for stripping or cleaning the surface. There are three main types of shot peening machines, differing in the way the shot is propelled, including compressed air, suction, and wheel, with compressed air being the most common. Typically peening will be completed in a cabinet to retain the shot for reuse.

When shot impacts the surface of the component, plastic deformation ensues, creating a dimple or crater in the surface, as shown in Figure 2-11.

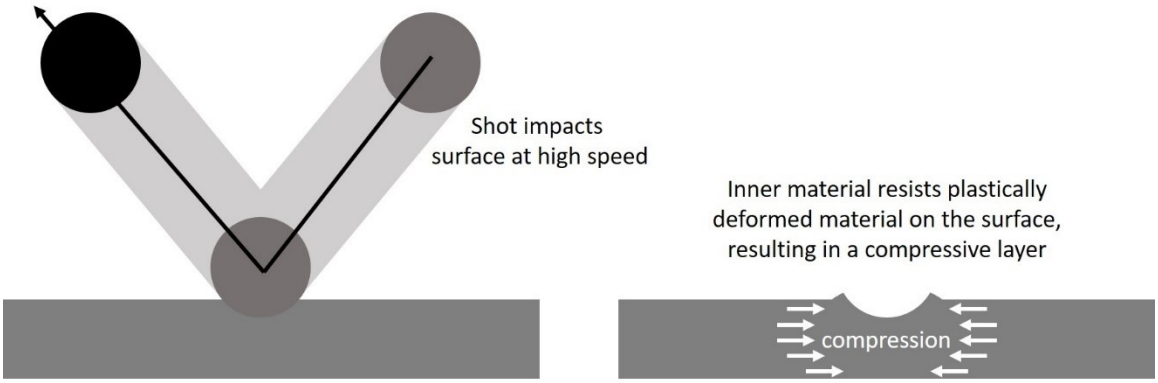

Figure 2-11 Plastic deformation caused by shot peening.

This plastic deformation at the treated surface is resisted by the inner material, resulting in a thin layer of compressive residual stress to form along the treated surface. Figure 2-12 depicts a typical residual stress profile caused by shot peening. As the body is in equilibrium, a tensile force opposes this compressive layer, but at a greater depth in the surface. It is this surface compressive layer that results in increased fatigue strength. Mechanistically, failure in metals is mainly due to tensile forces. With a compressive residual layer present, in-service tensile loads must thereby overcome this compressive force before the applied load will begin to deform the component. Hence, the maximum tensile stress actually developed within the material is reduced thereby invoking enhanced fatigue performance.

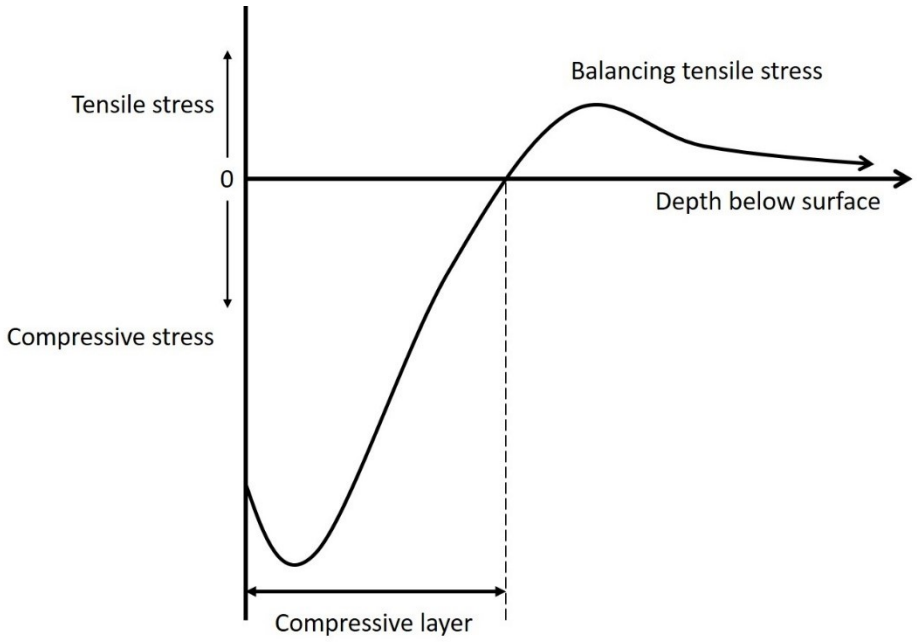

Figure 2-12 Typical residual stress profile resulting from shot peening.

The residual stress profile instilled through shot peening will vary depending on the intensity of peening and material being peened. For instance, depths of compressive residual stress can vary from tens of microns to over a millimeter, while the magnitude of peak compressive residual stresses held within the body will largely depend on the strength of the material being treated (generally, ~50% the materials static yield strength but can approach the yield strength of the material).

A number of different shot media types, in terms of size and chemistry, are utilized for peening. These include ferrous and nonferrous cast shot, cut wire shot, glass beads and ceramic shot. Cast steel shot is the most widely used, being made by water atomization. When ferrous contamination is a concern glass bead or ceramic shot may be utilized, or materials such as copper, aluminum or zinc alloys. Typical media sizes range from 0.18 mm to 2.4 mm. One major concern when selecting a shot type is to have hardness greater than that of the component to be peened as this will minimize the

damage to the shot, which is typically recirculated, screened for broken media and reused.

While working at Buick, John Almen realized the need to quantify the energy of the shot stream a component was subjected to. This energy is mainly due to the velocity of the shot. With this being rather difficult to measure, Almen developed a simple way to classify the intensity of peening, termed Almen intensity. Almen noticed that when a thin strip of metal was subjected to shot peening the compressive stress introduced would cause the strip to arc. Hence, standard steel Almen strips are subjected to the shot stream and arcing is then measured using an Almen gage, as depicted in Figure 2-13. The intensity is stated as an arc height, followed by the strip used. There are three standard Almen test strips, identified as A, C and N, with A being the standard strip, N used for light peening, and C used for aggressive peening. These differ in thickness and are utilized for different intensities (e.g. for an A intensity of less than 0.1 mm, an N strip should be used). An arc height of 0.4 mm using an N test strip would be classified as 0.4N intensity. Similarly, if English units are used, an arc height of 0.017” measured using an A strip would be 17A intensity.

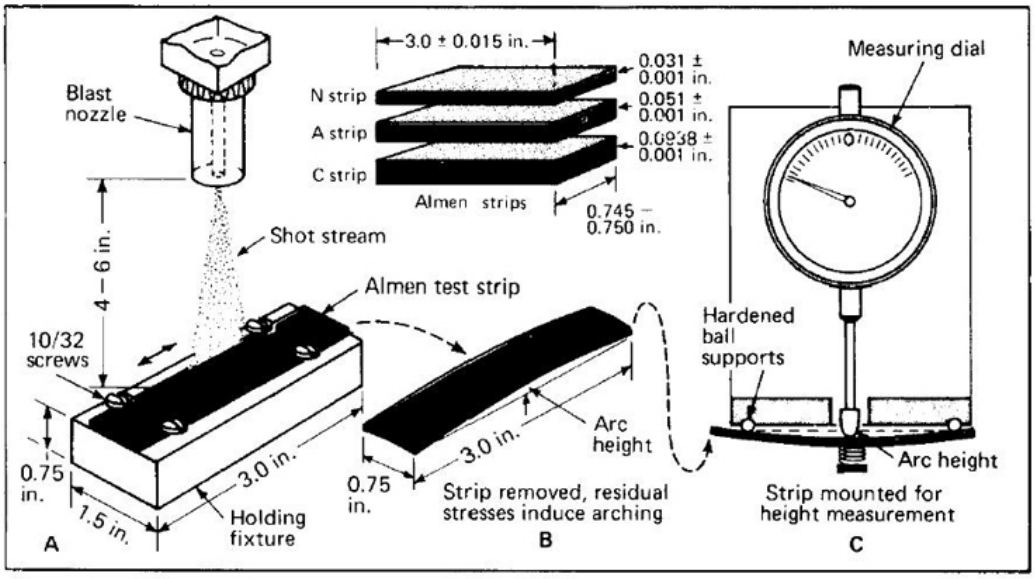

Figure 2-13 Almen intensity measurement [9].

Another important measurement is coverage. This is typically completed using a magnifying glass or microscope and is checked visually. Coverage is used to ensure the complete surface of the component is peened. The time of peening required to cover 98% of the surface is termed 100% coverage. Typically, coverage specifications will be anywhere from 100 to 300%. At 200% coverage, the component would be subjected to the shot stream for twice the time required to obtain 100% coverage. This ensures complete coverage. Throughout the duration of this work, coverage was maintained at >150%.

Shot will typically be analyzed visually with the aid of a microscope to ensure the shape and size of the media. This is usually completed before usage and at predetermined intervals. It is very important that fractured shot not be used during peening as this can damage the part surface. Usually there is some sort of screening system to remove damaged shot, but inspections are required periodically to ensure proper functioning.

2.4 Residual Stress

Residual stresses are stresses within a material that exist with no external forces acting on the body. These stresses are a result of different processes, commonly being due to either nonuniform plastic deformations within a component, or temperature gradients caused by various thermal processes such as welding or heat treatment. Several methods can be used to quantify the residual stress present within material. The first group of tests are destructive or semi-destructive and rely on the removal of bulk material and measuring the relaxation that takes place within the body. The second group of tests, which were utilized in this work and will be discussed, are non-destructive and rely on using the crystalline lattice of the material as a strain gauge. Two such tests include X-ray diffraction (XRD) and neutron diffraction (ND), which were utilized in this work. In the case of XRD, the measurements are limited to the near surface of metallic materials (on the order of tens of microns) due to the absorptivity of x-rays with matter. Depth profiling is possible, but requires the removal of material, resulting in destructive or semi-destructive testing. Neutrons on the other hand are considerably more penetrating, allowing for depth profiling non-destructively.

XRD is the most common method for measurement of residual stresses, being widely used in industry due to the availability of XRD systems, while ND requires a neutron source, usually requiring government facilities with considerably higher costs.

2.4.1 Utilizing Diffraction for Stress Measurement

Both XRD and ND rely on diffraction to use the crystal structure of a material as a very accurate strain gauge. This means that there needs to be some repeating structure within the material, therefore this is only useful on crystalline/polycrystalline structures

and cannot be used for measurement on amorphous materials. If residual stresses exist, the lattice spacing will be slightly different then the unstressed state, Figure 2-14.

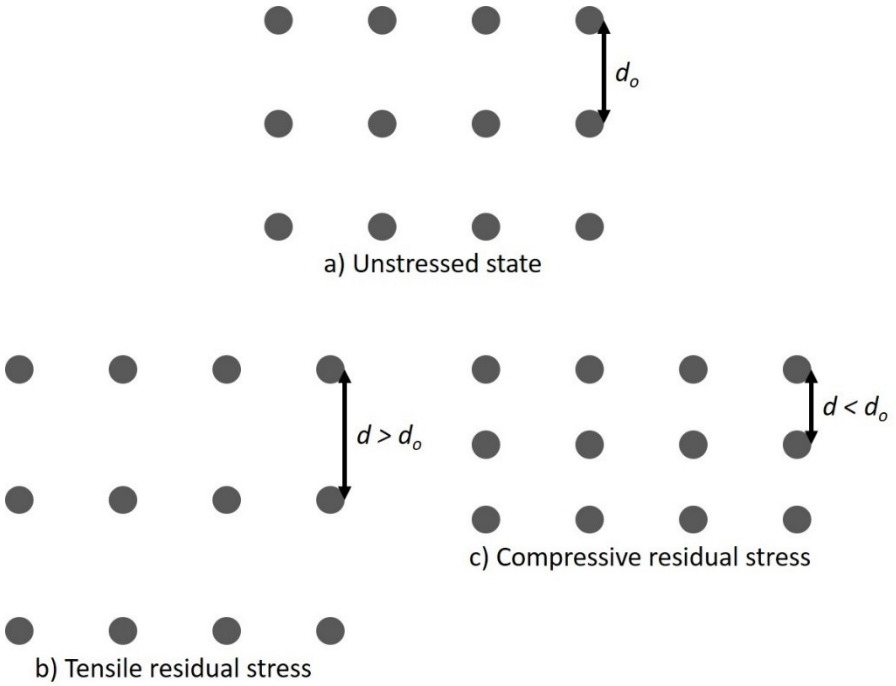

Figure 2-14 Changes to lattice spacing due to residual stresses.

The lattice spacing of a family of planes within the atomic structure is determined by measuring the angle of diffraction of the incident x-ray and applying Bragg's law, Eq 2-2.

$$\lambda = 2d_{hkl} \sin \theta_{hkl} \qquad (Eq\ 2-2)$$

Where λ is the wavelength of the x-ray (or neutron), d_{hkl} is the interplanar spacing of the family of planes {hkl}, and θ_{hkl} is the measured angle of diffraction caused by the family of planes {hkl}.

It should be clear that in order to measure the induced strain (and in turn determine the residual stress) caused by shot peening, an unstressed measure of the lattice parameter

of the system is required. It should also be noted that a sample that has been prepared for peening, for example including heat treatment, may have residual stresses present prior to peening due to material processing. If one compares the heat treated sample to the peened sample they will be determining the amount of residual stress induced by the peening process, and not necessarily the total amount of residual stress within the body. To determine the true residual stress within the material one would need an unstressed reference sample, ensuring the material processing for this sample did not result in any residual stress being introduced to the sample. For XRD measurements this can be avoided and will be discussed in Section 2.4.2.

The stress state at a point within a body can be expressed as a second order tensor, shown in Eq 2-3:

$$\sigma_{ij} = \begin{bmatrix} \sigma_{11} & \sigma_{12} & \sigma_{13} \\ \sigma_{21} & \sigma_{22} & \sigma_{23} \\ \sigma_{31} & \sigma_{32} & \sigma_{33} \end{bmatrix} \qquad (Eq\ 2-3)$$

Which can be related to the second order strain tensor by the elasticity tensor of the material C_{ijkl} through Eq 2-4:

$$\sigma_{ij} = \begin{bmatrix} \sigma_{11} & \sigma_{12} & \sigma_{13} \\ \sigma_{21} & \sigma_{22} & \sigma_{23} \\ \sigma_{31} & \sigma_{32} & \sigma_{33} \end{bmatrix} = C_{ijkl}\varepsilon_{kl} \qquad (Eq\ 2-4)$$

The elasticity tensor is of forth order and is a material property. From the stress tensor, there are six unknowns, as the off diagonal shear stress terms (e.g. σ_{12} and σ_{21}) must be equal for equilibrium to exist in the body. To solve the system of equations with six unknowns, six independent measurements must be taken. Usually some simplification

is possible knowing the stress state during measurement (e.g. plane-stress condition, knowing the principle directions, etc.) which will be discussed for the case of XRD and ND in the following sections.

2.4.2 X-Ray Diffraction

In the case of XRD, it is important to realize the measured lattice parameter (determined by Bragg's law and the angle of diffraction for a given family of planes) is limited to the near surface of the scanned component. This is a result of the absorptivity of matter to x-rays, with the penetration depth found using Eq. 2-5.

$$I_x = I_o e^{-\left(\frac{\mu}{\rho}\right)\rho x} \qquad (Eq\ 2-5)$$

Where I_x is the intensity of the x-ray after passing through a distance of x of the material, I_o is the incident intensity of the x-ray, μ/ρ is the mass absorption coefficient of the material, and ρ is the density of the material. It must also be noted that due to the exponential function in Eq. 2-5, much of the diffraction is coming from near-surface in the material. For example, based on Eq. 2-5, along with the geometry of diffraction, it can be found that the average depth of diffraction within aluminum comes from the top 20 μm of the sample for high angle diffraction (this calculation will be discussed in more detail in Section 4.6.2.3).

Typically, the main goal of XRD residual stress measurements is to determine the in-plane stress that exists on the surface of the sample in a specific direction, shown in Figure 2-15 as σ_φ.

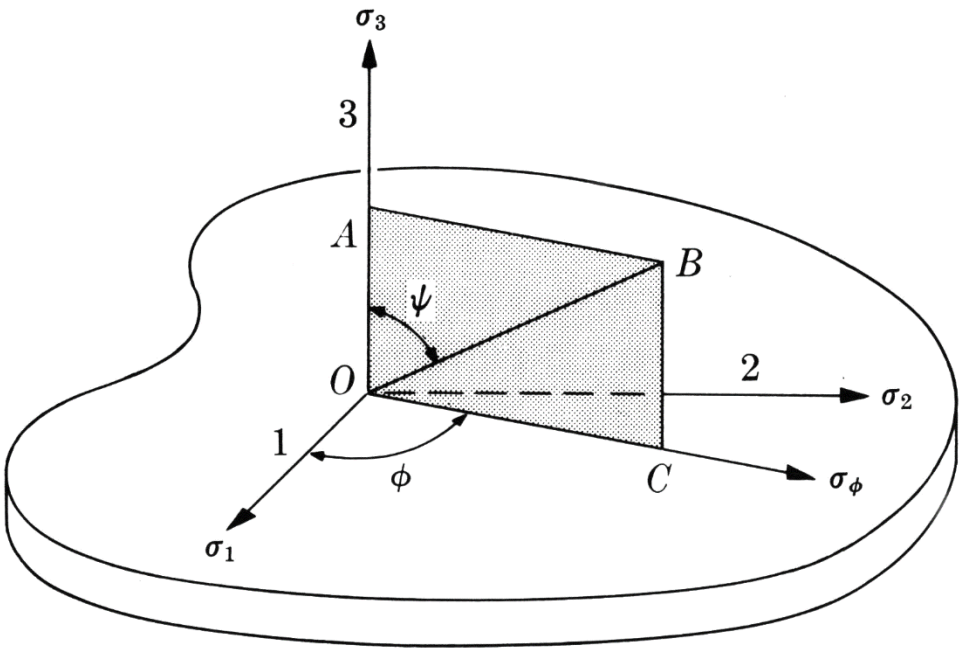

Figure 2-15 Surface stresses during XRD residual stress measurements [10].

Due to the near surface nature of XRD measurements, the volume with which diffraction takes place can be taken as in a plane-stress condition (i.e. the stress normal to the sample surface, σ_3, will be zero). Due to the assumption of σ_3 being zero, the principal stress directions will lie such that σ_3 is normal to the sample surface, and σ_1 and σ_2 will be in-plane with the sample surface.

Being concerned with the in-plane stress σ_φ, the d-spacing of primary importance would be of planes lying normal to the sample surface (normal to the vector OC in Figure 2-15 for example). Due to the geometry of XRD, measurement of the d-spacing of planes normal to the sample surface is virtually impossible, so measurements are made by rotating the bisector of the incident and diffracted x-ray off normal, as shown in Figure 2-16 for an inclination of ψ and in-plane tensile stress.

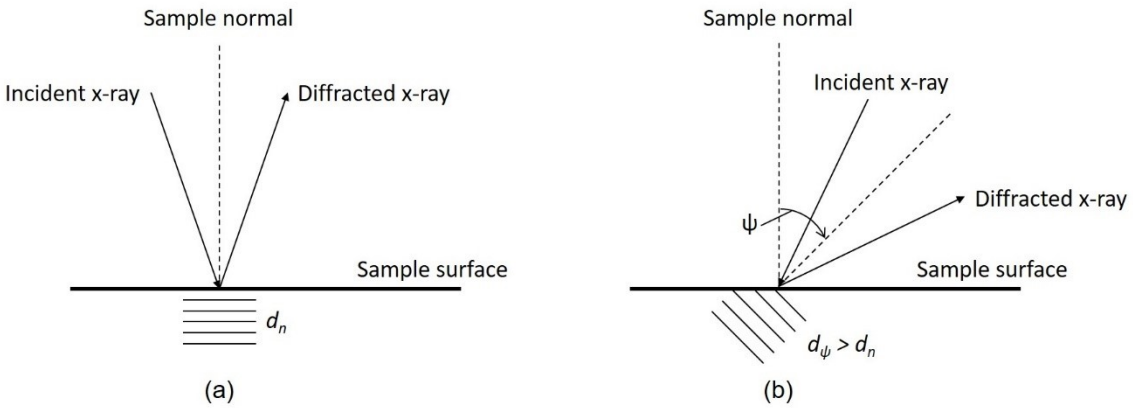

Figure 2-16 X-ray diffraction geometry with ψ-inclination during stress measurements.

This orientation shown in Figure 2-16 (b) would lie in the plane OABC in Figure 2-15. During these measurements, linear elastic theory is used to relate the strain value to stress, requiring the material properties of Young's modulus (E) and Poisson's ratio (v). In the case of diffraction work, the bulk properties of the material, which would typically be used in stress analysis are not suitable due to the anisotropic behavior of a single crystal. This is due to the measurements of planer spacing (d) being completed in a specific orientation within the anisotropic crystal lattice. For this reason, specific values of E and v are required for the d-spacing orientation in question and are denoted E_{hkl} and v_{hkl}. Common terms found in XRD residual stress measurements incorporate these specific orientation values of E_{hkl} and v_{hkl}, termed x-ray elastic constants (XEC) and defined as:

$$S_1 = -\left(\frac{\nu}{E}\right)_{hkl} \qquad (Eq\ 2-6)$$

$$½S_2 = \left(\frac{1+\nu}{E}\right)_{hkl} \qquad (Eq\ 2-7)$$

The strain in direction OB, or ε_ψ can be found based on elasticity theory for isotropic materials, as shown in Eq 2-8.

$$\varepsilon_\psi = \left(\frac{1+\nu}{E}\right)_{hkl} \sigma_\varphi \sin^2\psi - \left(\frac{\nu}{E}\right)_{hkl} (\sigma_1 + \sigma_2) \qquad (Eq\ 2-8)$$

The planer spacing d_ψ is what can be determined directly from Bragg's law and the angle of diffraction, which can be related to ε_ψ by:

$$\varepsilon_\psi = \frac{d_\psi - d_o}{d_o} = \left(\frac{1+\nu}{E}\right)_{hkl} \sigma_\varphi \sin^2\psi - \left(\frac{\nu}{E}\right)_{hkl} (\sigma_1 + \sigma_2) \qquad (Eq\ 2-9)$$

Rearranging for d_ψ yields:

$$d_\psi = \left[\left(\frac{1+\nu}{E}\right)_{hkl} \sigma_\varphi d_o \sin^2\psi\right] - \left[\left(\frac{\nu}{E}\right)_{hkl} d_o(\sigma_1 + \sigma_2)\right] + d_o \qquad (Eq\ 2-10)$$

Where d_ψ is measured based on the angle of diffraction at inclination ψ, σ_1 and σ_2 are constant for a sample (although unknown), v and E are material properties, d_o is the unstressed planer spacing, at this point unknown for the system, and σ_φ is to be solved for. Based on Eq 2-10, d_ψ will vary linearly vs. $\sin^2\psi$, shown by taking the differential of Eq 2-10 with regards to $\sin^2\psi$:

$$\frac{d d_\psi}{d \sin^2\psi} = \left(\frac{1+\nu}{E}\right)_{hkl} \sigma_\varphi d_o \qquad (Eq\ 2-11)$$

Solving for σ_φ yields:

$$\sigma_{\varphi} = \left(\frac{E}{1+\nu}\right)_{hkl} \frac{1}{d_o}\left(\frac{dd_{\psi}}{d\sin^2\psi}\right) \qquad (Eq\ 2-12)$$

If the material properties E_{hkl} and v_{hkl} are known, the slope of d_ψ vs. $\sin^2\psi$ can be found by making various measurements of d_ψ at different inclinations, ψ. At this point, to solve for σ_φ all that is required is d_o. To get a true unstressed planer spacing for the material is not trivial and an assumption can be made which introduces minimal error in the measurements. Back to the fact that the surface is in a plane-stress condition, the strain normal to the sample surface (ε_3) will be a result of Poisson's effect due to the principal stress σ_1 and σ_2, as shown in Eq 2-13.

$$\varepsilon_3 = -\nu(\varepsilon_1 + \varepsilon_2) = -\frac{\nu}{E}(\sigma_1 + \sigma_2) \qquad (Eq\ 2-13)$$

The strain ε_3 can also be related to the unstressed d-spacing of the material (d_o), along with the measured d-spacing normal to the sample surface (d_n):

$$\varepsilon_3 = \frac{d_n - d_o}{d_o} = -\frac{\nu}{E}(\sigma_1 + \sigma_2) \qquad (Eq\ 2-14)$$

Rearranging to solve for d_n finds:

$$d_n = d_o\left[1 - \left(\frac{\nu}{E}\right)(\sigma_1 + \sigma_2)\right] \qquad (Eq\ 2-15)$$

Since $E >> (\sigma_1 + \sigma_2)$ in the elastic region, the value of d_n will differ only slightly from d_o. As an example, considering E and v of 71 GPa and 0.33 (values for bulk aluminum), and

principal stresses of $\sigma_1 = \sigma_2 = -300$ MPa (relatively high for residual stresses within aluminum), from Eq 2-15 we find:

$$d_n = 0.9972 d_o \qquad (Eq\ 2-16)$$

With d_n being so close to d_o, the measurement of d_n, with the incident and diffracted x-ray bisector being normal to the sample surface (or $\psi = 0°$) can be substituted directly into Eq 2-12 with minimal error introduced:

$$\sigma_\varphi \cong \left(\frac{E}{1+\nu}\right)_{hkl} \frac{1}{d_n}\left(\frac{d d_\psi}{d \sin^2 \psi}\right) \qquad (Eq\ 2-17)$$

At this point, if various measurements of d_ψ are made, typically from -45° to +45°, including measurement at $\psi=0°$, the slope can be found and Eq 2-17 can be solved for σ_φ.

2.4.3 Neutron Diffraction

When dealing with ND, a beam of neutrons is used to probe a material, similar to an x-ray beam used in XRD analysis. As these measurements rely on the phenomenon of diffraction, the beam of neutrons is treated as a wave.

There are two main ways that neutrons are produced for the purpose of neutron scattering. The first is essentially the exact same as nuclear power generation, where a fission reaction is used. The second is rather different requiring a spallation source. Measurements were completed at the Canadian Neutron Beam Center (CNBC) (Chaulk

River, ON) on their National Research Universal (NRU) reactor. The NRU reactor is a 135 MW fission reactor operated partially as a research tool supplying neutrons for nuclear, materials and engineering work.

Similar to produced x-rays, a neutron source produces a polychromatic or “white” beam, meaning there is a wide range of neutrons with varying speeds, and in turn, varying associated wavelengths. As these measurements rely on diffraction of the incident wave of neutrons, Bragg’s law is utilized and a monochromatic beam is desired. There are various methods to obtain a monochromatic beam from the neutron source, although the main method used at CNBC on the stress measuring spectrometer, is that of a single crystal monochromator. Here, the incident neutron beam encounters a single crystal, shown in Figure 2-17, which will cause diffraction to occur at a defined angle, θ, consisting of a very narrow range of wavelengths that satisfy Bragg’s law.

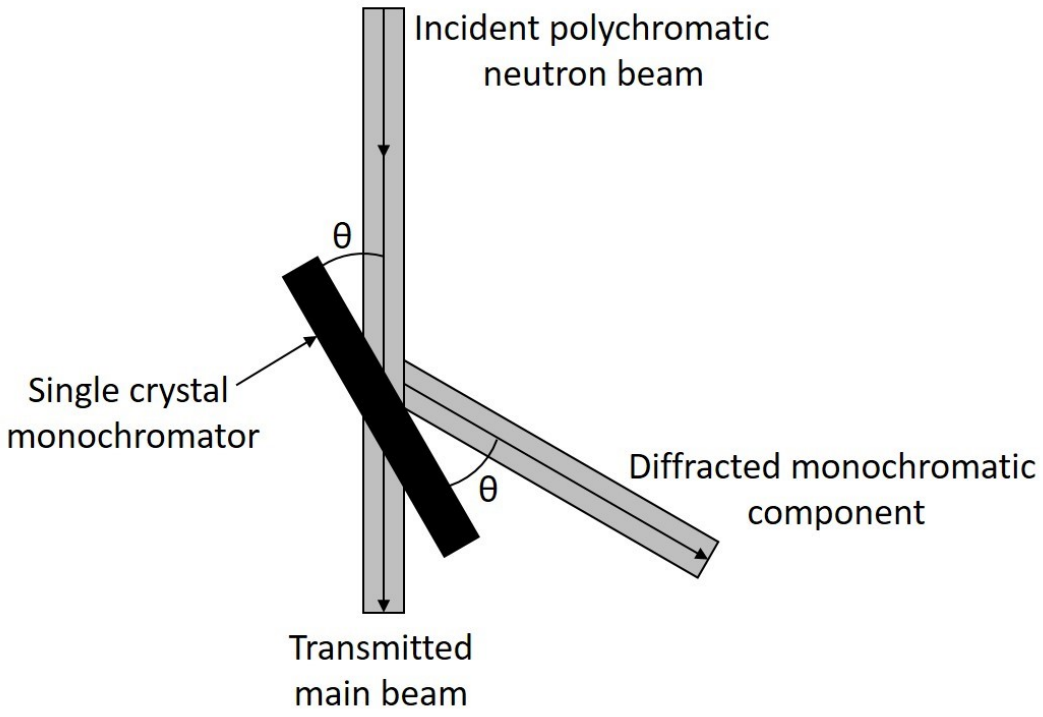

Figure 2-17 Single crystal monochromator used during ND measurements.

Knowing the lattice spacing of the single crystal monochromator used, *d*, one can select an angle, θ, which will result in a known wavelength, λ.

Where x-rays are scattered by the electron cloud of an atom, neutrons interact and are scattered by the nucleus of an atom. Since a neutron is neutral in charge, and much more massive than an electron, there is very little interaction with orbiting electrons. An incident beam of neutrons can be thought of as a plane wave, which when coming in contact with the nucleus of an atom scatters spherically in all directions. The nucleus acts as an ideal point scatterer, producing spherical waves.

In order to determine residual stresses, residual strains within the lattice are measured. These residual stresses will cause shifts in the diffraction peak position. The strain within a body can be related to the measured d-spacing from diffraction, along with the unstressed d-spacing of the system:

$$\varepsilon = \frac{d - d_o}{d_o} \qquad (Eq\ 2-18)$$

Where: d is the lattice spacing of the material while d_o is the unstressed lattice spacing. Substituting Bragg's law, strain as a function of diffraction angle can be found:

$$\varepsilon = \frac{\sin(\theta_o)}{\sin(\theta)} - 1 \qquad (Eq\ 2-19)$$

As we are primarily concerned with measurement of the residual stresses present within the body, this measure of strain must be related to the stress by linear elastic theory.

With a suitable number of strain measurements in various orientations, the stress tensor can be solved by:

$$\sigma_{1,2} = \frac{E}{(1+\nu)(1-2\nu)}\left[(1-\nu)\varepsilon_{1,2} + \nu\left(\varepsilon_{2,1} + \varepsilon_3\right)\right] \qquad (Eq\ 2-20)$$

$$\sigma_3 = \frac{E}{(1+\nu)(1-2\nu)}\left[(1-\nu)\varepsilon_3 + \nu(\varepsilon_1 + \varepsilon_2)\right] \qquad (Eq\ 2-21)$$

Where $\sigma_{1,2}$ and $\varepsilon_{1,2}$ are the in-plane stresses/strains on the surface of the part, while σ_3 and ε_3 are the stress/strain values normal to the sample surface. E and v represent Young's Modulus and Poisson's ratio of the material in question, and similar to XRD measurements, as the strain values are measured in a specific orientation of the crystal, the values of E and v should represent the material response in a specific loading orientation of the crystal.

One of the major benefits of working with neutrons over x-rays is their much higher degree of penetration within materials. It is due to this that the measurements of strain can be made directly normal to the sample surface, where this is impossible with x-rays, and required the ψ rotation normal to the sample surface during XRD measurements.

Chapter 3: Effects of Shot Peening on Aluminum Powder Metallurgy Alloys

Matthew D. Harding and Donald P. Bishop
Department of Process Engineering and Applied Science
Dalhousie University
Halifax, NS B3J 2X4

Ian W. Donaldson
GKN Sinter Metals LLC
Auburn Hills, MI 48326

Status: M.D. Harding, I.W. Donaldson, and D.P. Bishop, "Effects of Shot Peening on Aluminum PM Alloys", Proceedings of the 2010 International Conference on Powder Metallurgy and Particulate Materials, MPIF, Vol. 6, 29-40 (2010).

Author Contributions: The experimental procedure was developed jointly by M.D. Harding and D.P. Bishop, with input from I.W. Donaldson. All experimental work was carried out and compiled by M.D. Harding, along with first draft of the manuscript. The current state of the manuscript is a result of editing by all three authors.

3.1 Forward to Chapter 3

This project began primarily as a study to determine the gains in fatigue strength achievable from shot peening of an aluminum PM alloy. This particular aluminum alloy had been largely characterized previously in the research group, including sintering and heat treatment response, so material processing was followed in accordance with these previous studies. As shot peening was new to the research group, an automated system was developed to ensure consistent peening between samples, as well as considering suitable peening intensities for the material in question. Rotating bending fatigue (RBF) was completed in a non-controlled, open atmosphere.

3.2 Abstract

As concerns over environmental impact on our planet grow there is a continued push to decrease carbon dioxide and other pollutant emissions to the atmosphere. The automotive industry feels this drive for increased efficiency more than any other. A technology that may increase vehicle fuel economy is aluminum powder metallurgy (PM) by reducing the overall weight of vehicles via the expanded use of lightweight aluminum PM components. In an effort to increase the mechanical properties of conventional aluminum PM alloys the effects of shot peening have been studied. Various peening intensities were considered by analyzing the general surface condition, roughness, and sub-surface attributes. This was completed on specimens pre and post peening using a combination of non-contact optical profilometry, optical microscopy, and scanning electron microscopy. A suitable peening intensity was chosen and the effects of peening were quantified with a focus on fatigue life. Comparisons to equivalent wrought aluminum alloys are also made.

3.3 Introduction

Vehicle emissions are a major contributor to global pollutant levels and with the continued increase in public awareness the automotive industry is continuously feeling the push for more environmentally friendly vehicles. Automakers are searching for ways to increase fuel economy, and one major area for improvement is the reduction in vehicle weight. According to Ducker Worldwide, an independent research firm specializing in the global automotive industry, weight reduction including segment shift will contribute 25% of the improvement in fuel economy and CO_2 reduction required by 2020 [11]. The movement from large vehicles to more compact models will be a significant amount of this reduction (segment shift), but the use of lightweight materials

in place of heavy steel will also be a major contributor. Some of the leading materials for replacement of steel components are aluminum alloys. One processing method of aluminum that has shown increased benefits in the way of economic gains and unique mechanical properties over other traditional routes is powder metallurgy (PM). The main benefit of aluminum PM is a reduction in processing costs due to the “near net shape” approach that minimizes machining and the amount of wasted material. One downside to these PM alloys is residual porosity within the material, which results in decreased mechanical properties. Porosity is typically reduced to an amount where the material is considered fully dense by hot forging. This process adds to the cost of production, but can result in mechanical properties that actually outperform wrought equivalents, in particular, those of fatigue [12].

Another process that holds great potential in increasing the fatigue properties of aluminum PM alloys is shot peening. This technique has been used for some time to increase the performance of components produced from wrought aluminum alloys and forged PM steels but little to no information is available with respect to its effects on aluminum PM materials. Shot peening is a process by which a material is bombarded with small spherical balls, termed “shot”. The impact of these shot against a materials surface prompts the formation of small dents on the surface via plastic deformation. The net result is a narrow layer of compressive residual stress induced at the surface. As fatigue cracks initiate and propagate in tension, this layer of compressive residual stress will resist tensile forces. Hence, an applied load must first overcome this barrier of compressive residual stress before crack initiation can occur. By this means, the fatigue strength of a material can be increased by the shot peening process.

Shot peening is typically used as a method to resist fatigue and stress corrosion failures. The extent of increase can vary largely due to a number of parameters including the peening process and the material in question. Shot peening has the added benefit of closing surface pores of press and sinter components, which can act as stress raisers. According to the ASM Metal Handbook, an increase of at least 20% in endurance limit due to shot peening can be seen with PM press and sinter steel components with small cross sections (6 x 6 mm) [13]. It has also been found that increases in fatigue strength in the range of 20 – 50% can be achieved on powder forged steel components [14, 15] while gains in wrought aluminum alloys typically amount to improvements on the order of 20 – 35% [16]. With increases to this extent shot peening of aluminum PM alloys holds great potential and may be able to make aluminum PM more competitive with wrought equivalents on a performance basis.

3.4 Materials

The main material of interest in this study was PM7075, a commercial PM alloy developed as an equivalent to wrought aluminum 7075. This PM blend was produced by Ecka Granules and is designed for press and sinter processing. Details on this blend are given elsewhere [3]. The nominal chemical compositions for PM7075 and AA7075 are shown in Table 3-1.

Table 3-1 Chemical compositions of PM7075 and wrought AA7075 wt%.

	Al	Zn	Mg	Cu	Sn
PM7075	Bal.	5.5	2.5	1.6	0.2
Wrought AA7075	Bal.	5.6	2.5	1.6	--

3.5 Experimental Techniques

The PM processing route followed was a two-stage approach of uni-axial die compaction and controlled atmosphere sintering. To compact the powder blends, an Instron 5594-200HVL load frame was used in conjunction with self-contained tooling. Here, powders were briquetted at 600 MPa into Charpy bars (75 x 12.7 x 12.7 mm). All bars were then sintered in a controlled atmosphere tube furnace. The heating cycle included a 20 minute dwell at 400°C for de-lubrication purposes followed by sintering at 605°C (20 minutes), and finally, a gas quench to ambient in a water-jacketed cooling section. A flowing atmosphere of ultra-high purity nitrogen (>99.999%) was maintained throughout the entire cycle. All compacts were sintered to a final density of 2.77 g/cm^3, this equated to 98.6% of the full theoretical density (2.81 g/cm^3). A T6 heat treatment was then applied to all sintered bars prior to peening. This was a three-stage process that included solutionization at 470°C for 90 minutes followed by a water quench, and artificial aging at 125°C for 24h.

Shot peening was quantified by use of Almen Intensity. Here, standard Almen strips were peened in the same manner as PM substrates. The amount of arcing that was measured in the Almen strip indicated the Almen intensity of the peening process. Two types of Almen strips had to be utilized in this study, A and N. A – type strips are considered to be the standard, while N – type strips are used for lighter peening intensities. As the considered intensities varied between the range for N and A strips as per SAE standards [9] both had to be utilized. For comparison, the common rule of thumb is that the Almen intensity measured using an N strip is approximately three times that measured using an A strip (e.g. 0.2 mmA is approximately 0.6 mmN).

In order to achieve consistent, repeatable peening results an experimental shot peening apparatus was designed. The peening unit utilized, shown in Figure 3-1 (a), was a pressurized, self-contained cabinet that allowed for control of shot flow through the use of an in-stream pinch valve and control over shot velocity using regulated air pressure. The automated system utilized an electric motor driven linear actuator coupled with a linear track and various sample holders. This unit, seen in Figure 3-1 (b), ensured that the time of exposure to the shot stream could be accurately controlled.

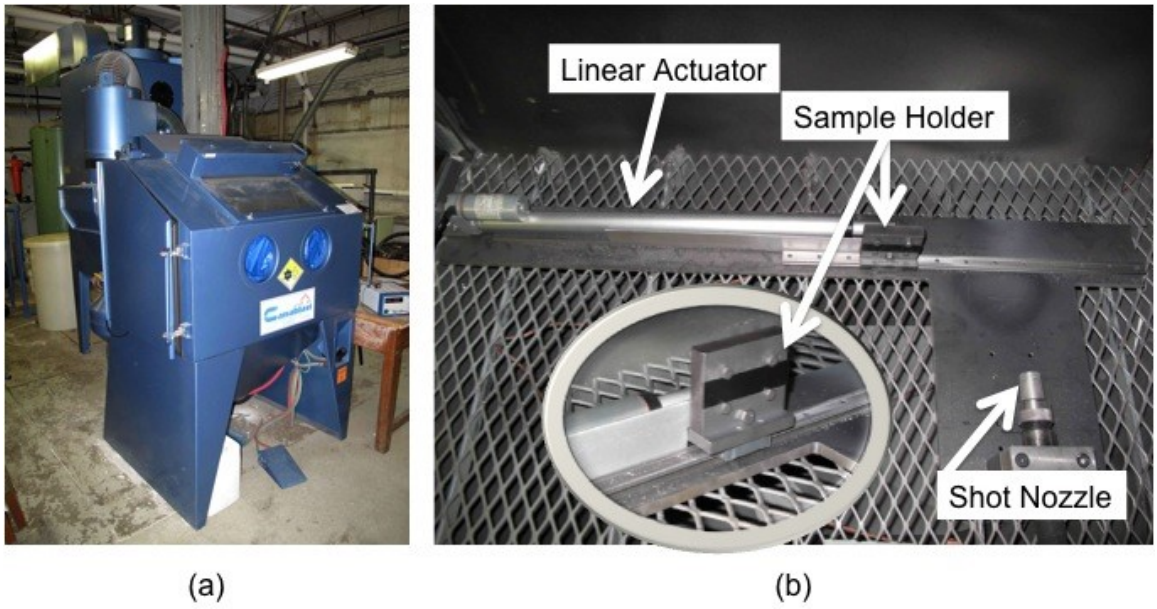

Figure 3-1 Components of the system utilized in the shot peening of aluminum PM bars, (a) peening cabinet and (b) automated system.

In order to assess the surface characteristics of the peened material, as sintered and T6 heat treated Charpy bars were peened at various intensities and analyzed using a combination of optical and scanning electron microscopy (SEM) as well as non-contact optical surface profilometry. In order to study the sub-surface condition of the peened samples cross sections were mounted under vacuum in an epoxy resin. Cured mounts were then ground and polished using a Buehler Vector Power Head auto-polisher and various diamond pastes and extender from 9 μm down to 1μm and finished using 0.05

μm colloidal silica, finished mounts were then examined using optical imaging. The SEM unit utilized was a Hitachi S-4700 cold field system operated at an accelerating voltage of 10 kV and a beam current of 15 μA. Optical images were captured using a Unitron Optical Microscope equipped with a Micro Metrics digital camera at various magnifications ranging from 50x to 500x. The non-contact surface profiler used was a Nanovea Micro-Profiler, model PS50 with a 130 μm sensor. Nanovea 3D software package was used for data acquisition and Nanovea Mountains Pro 3D for surface analysis. Surface scans were conducted over a 1.5 x 1.5 mm area with a step size of 1.5 μm in the x and y direction and averaging set to 2. A 4 mm profile scan was completed on fatigue bars in the center radius with a step size of 0.1 μm and averaging set to 2.

To complete fatigue testing aluminum PM Charpy bars were machined down to 6.35 mm diameter hourglass specimens. Wrought AA7075 – T6 samples were also machined to the same configuration for comparison purposes. To alleviate circumferential scratches in the surface due to machining, all samples were polished longitudinally using a Dremel Multipro Model 395 and 1 μm diamond paste and extender. As the peening setup only allowed for purely linear motion, the machined and polished PM bars had to be peened using a series of linear sweeps. Here, samples were peened at 90° intervals, meaning that the bar would be peened traveling longitudinally past the shot stream, rotated 90° and then peened again. This peen/rotate sequence was then repeated until the full circumference of the bar was treated. The surface topography and roughness of the peened fatigue bars was then measured at 30° intervals around the circumference to ensure consistency in peening.

Samples were tested for fatigue strength using a fatigue dynamics rotating-bending fatigue test frame operated at 50 Hz. A total of 10 polished samples of wrought AA7075 – T6 were tested followed by 10 polished then peened bars of the PM equivalent, PM7075 Fatigue strength was then found according to the staircase method [17] using an endurance life of 5 million cycles and a step size of 9 MPa.

3.6 Results and Discussion

3.6.1 Surface Characterization

Before the effect of peening on the fatigue properties could be studied a suitable peening intensity had to be determined. According to SAE and ASTM, suggested peening intensities for aluminum alloys range from 0.15 mmA to 0.25 mmA [18, 19]. When an excessive intensity is used during peening the surface of the material can become damaged, called over peening. This can be very detrimental and even cause surface cracking to begin, resulting in pre-mature failure. In an attempt to determine a suitable peening intensity three Charpy bars were peened to intensities of 0.25 mmN, 0.4 mmN, and 0.2 mmA. These samples were then analyzed using SEM, the images generated can be seen in Figure 3-2.

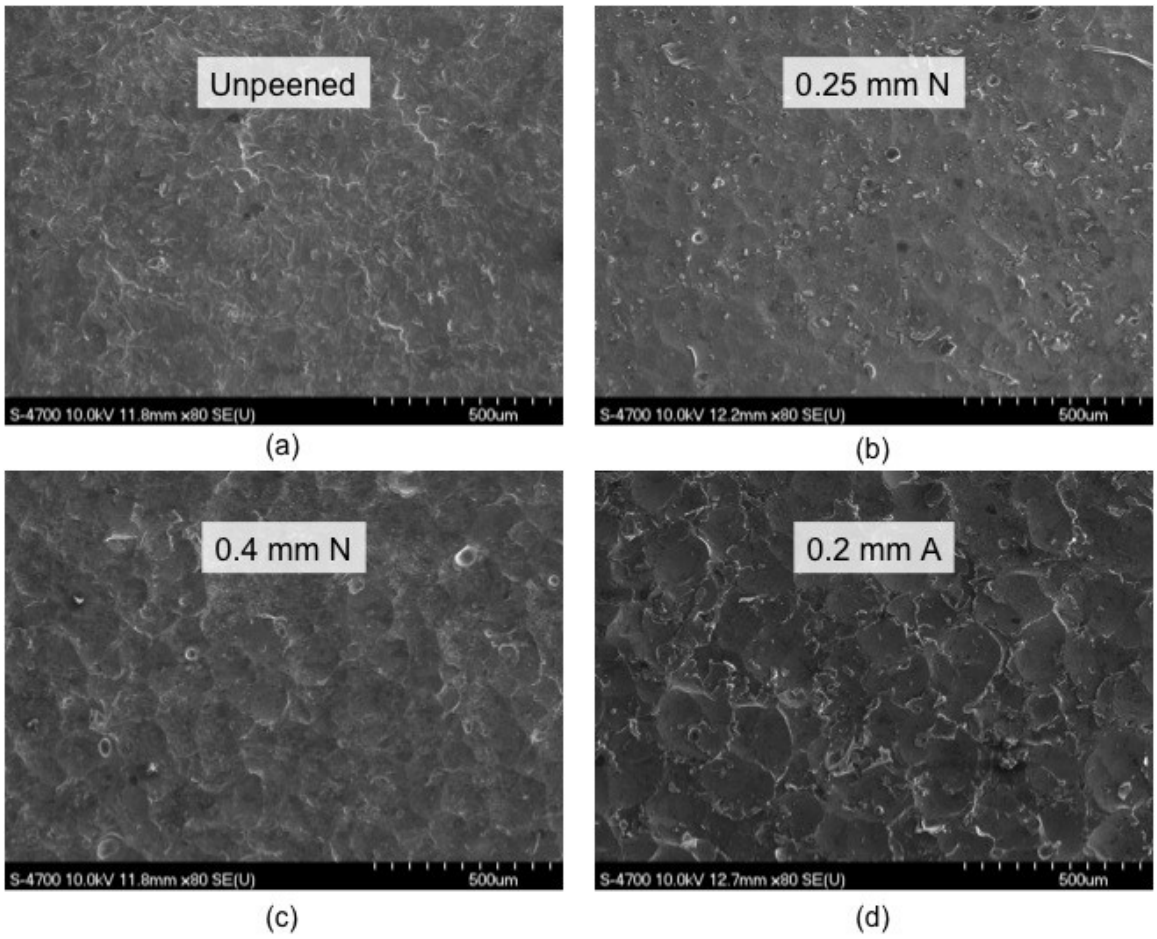

Figure 3-2 SEM imaging of peened surfaces prepared at various intensities, (a) unpeened, (b) 0.25 mmN, (c) 0.4 mmN and (d) 0.2 mmA

From Figure 3-2 (d) it appeared that there was considerable surface damage occurring at 0.2 mmA intensity. From Figure 3-2 (c), 0.4 mmN intensity did not appear to be damaging the surface of the material, while clear denting can be seen, indicating plastic deformation and in turn, that compressive residual stress has been introduced. The lower peening intensity of 0.25 mmN (Figure 3-2 (b)) also had noticeable denting, but much less than the higher intensities.

Using a non-contact optical profiler, the surface topography of the unpeened and peened 431D samples was obtained. Sample 3D images of the PM 431D material unpeened

and peened to 0.4 mmN intensity are shown in Figure 3-3. This allowed for the surface roughness of the material to be found using the software suite Nanovea Mountains Pro 3D. The measured roughness values for the as sintered/heat treated material, as well as those peened at various intensities are shown in Figure 3-4. It was found that peening to intensities of 0.25 mmN and 0.4 mmN had little to no effect on the surface roughness, while a substantial increase occurred at a peening intensity of 0.2 mmA. It is typically regarded that a smoother surface will perform better than a rough surface in fatigue due to stress raisers present in a roughened surface.

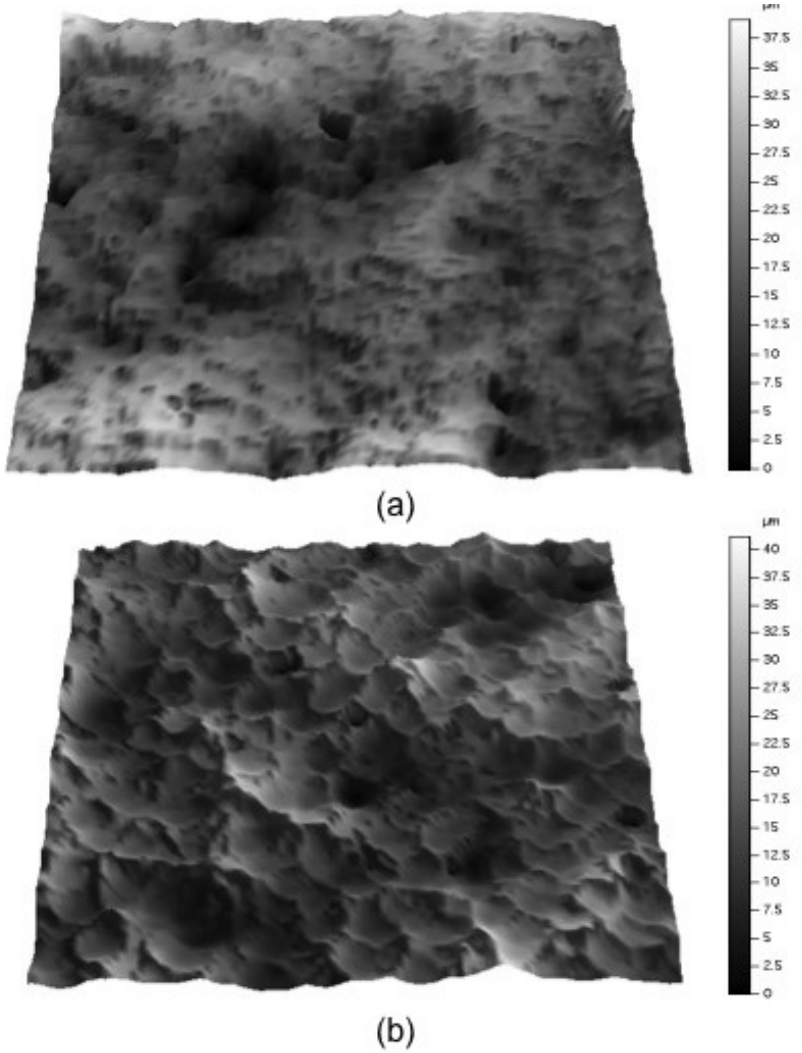

Figure 3-3 Surface topography of aluminum PM7075 – T6 (a) unpeened, and (b) peened to 0.4 mmN.

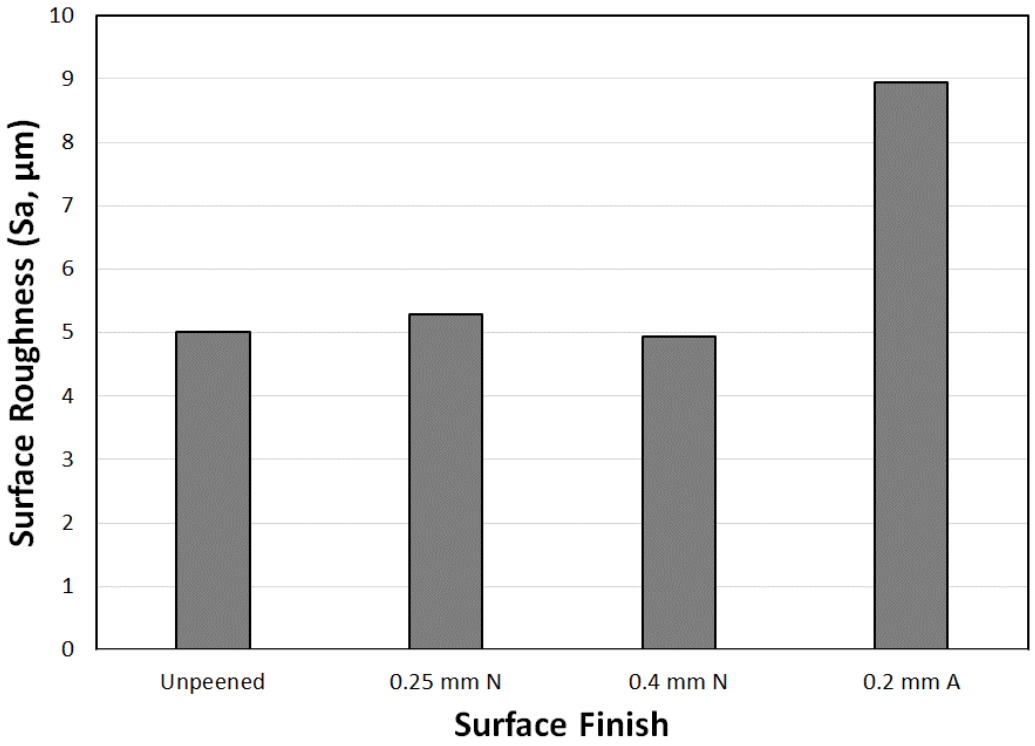

Figure 3-4 Surface roughness of as sintered PM 431D and peened to intensities of 0.25 mmN, 0.4 mmN and 0.2 mmA.

To understand the effects of peening on the sub-surface material, cross sectional mounts were examined. The resultant micrographs are shown in Figure 3-5. Similar to the SEM surface images, a peening intensity of 0.2 mmA appeared to damage the surface. This was evident as material folded over adjacent material, which resulted in sub surface cracking. When over peening occurs one form of damage that can transpire is peened surface extrusion folds (PSEF). PSEF are a result of excessive material flow lateral to the peened surface, and can cause premature fatigue failure due to acceleration in crack nucleation [20]. This showed strong indication that a peening intensity of 0.2 mmA was too aggressive for the PM alloy. Noticeable denting was also observed with 0.4 mmN intensity, yet no PSEF had occurred. At an intensity of 0.25 mmN very minimal surface change was seen between the peened and unpeened surfaces, consistent with SEM observations.

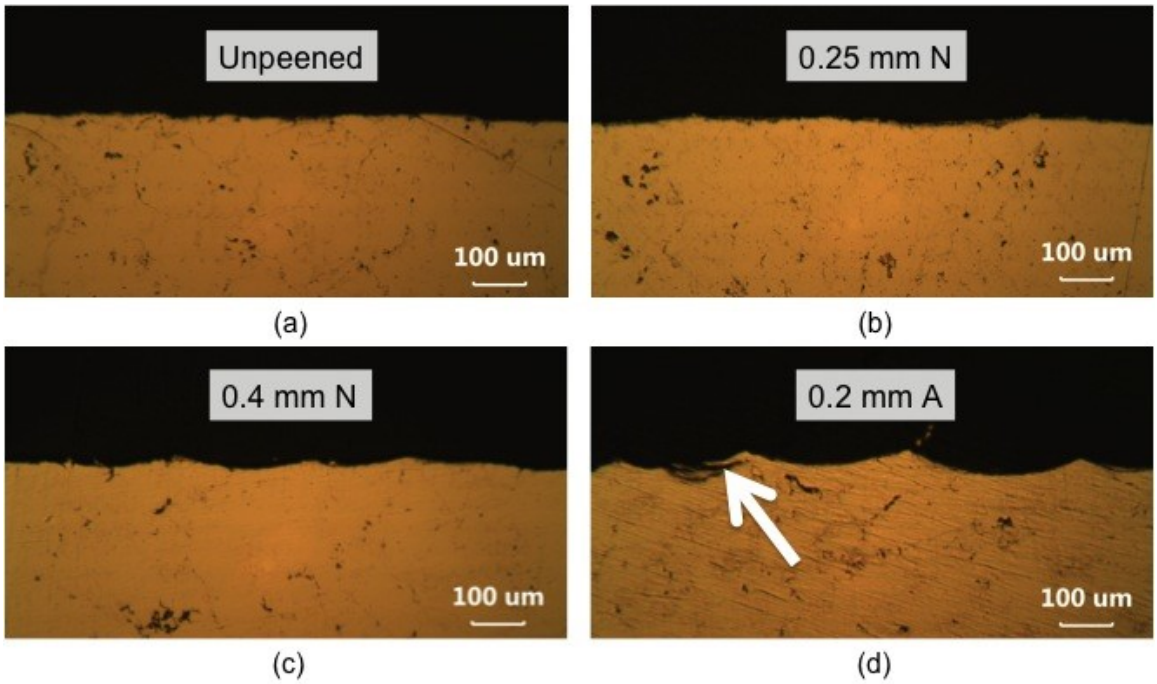

Figure 3-5 Cross-sections of peened surfaces, (a) Unpeened, (b) 0.25 mmN, (c) 0.4 mmN, and (d) 0.2 mmA. PSEF shown by arrow.

3.6.2 Fatigue Testing

From the surface characterization, a peening intensity of 0.4 mmN was chosen for further analysis, specifically the effects of this intensity on the fatigue strength of PM 431D. According to a previous study conducted at Dalhousie University the fatigue strength of PM7075 at 5 million cycles is approximately 130 MPa [12], the samples used in the current study were prepared in a similar manner for comparison sake.

Prior to fatigue testing the machined samples (wrought and PM) were polished to alleviate the circumferential cut marks from machining. Figure 3-6 shows the profile scans of fatigue bars as machined, polished and peened to 0.4 mmN intensity, in these figures the radius of the fatigue bar was removed to show purely the surface roughness. From the profile scans the corresponding roughness values were found as shown in Table 3-2.

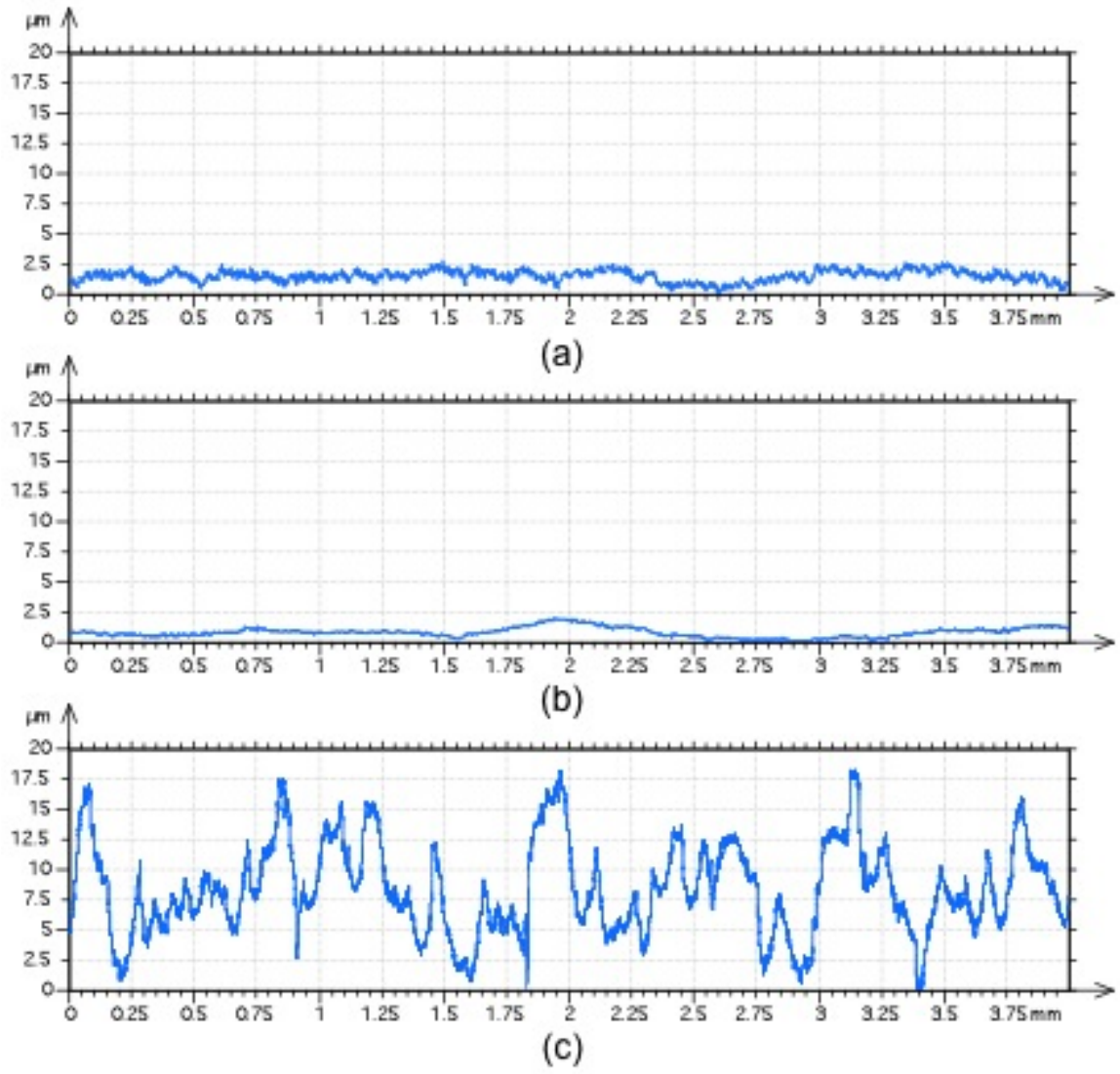

Figure 3-6 Profile scan of fatigue bars, (a) as machined, (b) polished, and (c) peened to 0.4 mmN intensity.

Table 3-2 Surface roughness for various surface finishes.

Surface Finish	Machined	Polished	Peened to 0.4 mmN
Roughness (Ra)	0.257 µm	0.104 µm	2.399 µm

Before samples were tested the consistency of circumferential peening had to be validated. Using the non-contact optical surface profiler, the center radius of the fatigue

bars was scanned to show the surface topography. A consistent roughness around the circumference would indicate an even amount of peening induced plastic deformation and in turn it is speculated an even amount of residual stress introduced. Figure 3-7 shows a sample scan of the fatigue bar radius.

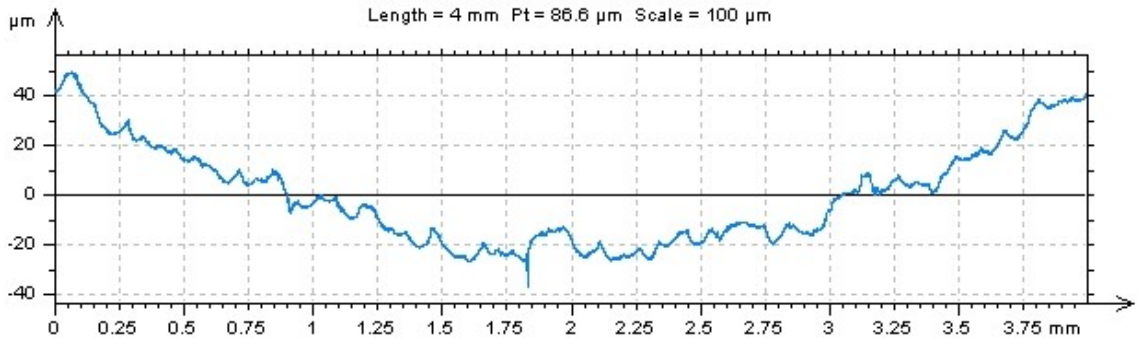

Figure 3-7 Surface scan of a fatigue bar radius peened to 0.4 mmN intensity.

Software was then used to find the surface roughness. This was completed at 30° intervals around the bar on two separately peened specimens. The results are shown in Figure 3-8, showing the angle of rotation vs. roughness.

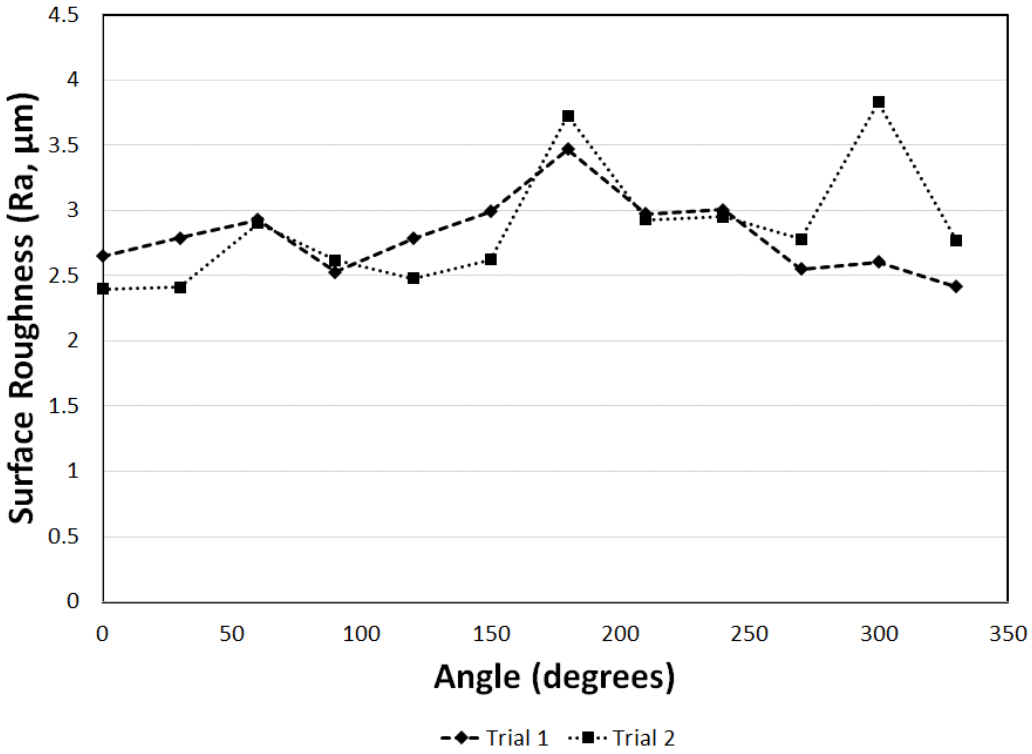

Figure 3-8 Surface roughness around the circumference of fatigue bar.

Although there were a few points where the roughness was slightly higher the most important observation was that there was no pattern of an increased surface roughness at certain intervals, e.g. it was not seen that when the shot stream was perpendicular to the sample being peened (at 0°, 90°, 180° and 270°) a higher surface roughness occurred, which would have indicated uneven peening. With this, it was believed that consistent peening was achieved around the circumference of the bar.

Fatigue testing was conducted on wrought AA7075 and peened PM7075 aluminum alloys in accordance with MPIF Standard 56 [17]. The staircase method was applied and statistical analyses enabled the calculation of the fatigue strengths at various probabilities of failure, as shown in Table 3-3.

Table 3-3 Fatigue comparison of wrought AA7075 to peened PM7075 aluminum alloys at various probabilities of failure.

Material	50%	90%	10%
Wrought AA7075-T6	258 MPa	243 MPa	273 MPa
Peened PM7075-T6	177 MPa	146 MPa	208 MPa
PM7075-T6 [12]	130 MPa	---	---

It was found that peened PM7075 was out performed by the wrought AA7075 material, but of more importance to this study is the increase seen in PM7075 through shot peening. When compared to the fatigue strength found in previous studies an improvement of 36.2% was seen. This is a very significant gain, which decreased the gap in performance between the PM and wrought materials. This increase was in the high end of gains seen in wrought aluminum alloys by shot peening (20 – 35%) and considerably higher than that known to occur in wrought AA7075 – T6, 25% [16]. The considerably higher increase in fatigue strength seen in PM over wrought is possibly due to a two-fold effect: peening induced residual stresses, plus the closing of surface porosity. The latter was an added benefit with peening PM materials as it is well known surface pores can act as stress risers and lead to premature failure.

An important note is that the peening intensity of 0.4 mmN may not be optimal for the PM7075 material. Even greater improvements in fatigue strength can be expected with further study into various peening intensives. Although wrought AA7075 – T6 still out performs peened PM7075 – T6 studies have shown that forged PM7075 – T6 actually out performs wrought AA7075 – T6 [12]. Therefore, shot peening of forged PM7075 material has the potential to significantly outperform wrought AA7075 while maintaining the benefits of the PM process, specifically reducing production costs and material waste.

3.7 Conclusions

From the completed work, it has been concluded that:

1. 0.2 mmA peening intensity resulted in noticeable surface and sub-surface damage occurring to Alumix 431D in the as-sintered and T6 heat treated state, indicating over peening was occurring.
2. A peening intensity of 0.4mm N showed noticeable surface denting, while little to no surface or sub-surface damage was seen.
3. Peening of a round sample in a linear fashion can produce consistent surface roughness and in turn, it is speculated that a consistent state of residual stresses is induced.
4. Shot peening of 431D – T6 PM alloy to 0.4 mmN intensity resulted in an increase in fatigue strength of approximately 36%.
5. Higher gains were seen in shot peening of PM material over literature of improvements in wrought material. This may be an indication that peening is reducing the surface porosity, an added benefit in peening of PM materials.

3.8 Acknowledgments

The authors would like to acknowledge the financial support provided by the Natural Sciences and Engineering Research Council (NSERC) of Canada via Strategic Grant 350505-07. Also, the provision of all powdered metal material by Ecka Granules is graciously acknowledged.

Chapter 4: Characterization of the Microstructure, Mechanical Properties, and Shot Peening Response of an Industrially Processed Al-Zn-Mg-Cu PM Alloy

M.D. Harding[a], I.W. Donaldson[b], R.L. Hexemer Jr.[c], M.A. Gharghouri[d], D.P. Bishop[a,*]

a - Department of Process Engineering and Applied Science, Dalhousie University, Halifax, NS, B3J 2R4, Canada
b – Tech Center, GKN Sinter Metals LLC, Auburn Hills, MI, 48326, USA
c - GKN Sinter Metals LLC, Conover, NC, 28613, USA
d - Canadian Neutron Beam Center, Chalk River Laboratories, Chalk River, ON, K0J 1J0, Canada
* Corresponding Author – Paul.Bishop@dal.ca; Phone 1.902.494.1520

Status: Published. Journal of Materials Processing Technology, (2015), vol. 221, pp. 31-39.

Author Contributions: The experimental procedure was developed jointly by M.D. Harding and D.P. Bishop, with input from I.W. Donaldson and R.L Hexemer Jr, apart from neutron diffraction work, where experimental procedure was developed by M.A. Gharghouri and M.D. Harding. The neutron diffraction work was carried out by M.A. Gharghouri with M.D. Harding helping, and industrial processing (compaction and sintering) was completed by R.L Hexemer Jr. All other experimental work was carried out and compiled by M.D. Harding, along with first draft of the manuscript. The current state of the manuscript is a result of editing by all five authors.

4.1 Forward to Chapter 4

At this point the scope of the project expanded, with focus heavily placed on industrial processing of the alloy. Prior work largely resulted from lab-based processing, and to verify the alloy would respond in a similar manner in an industrial setting, industrially

processed samples were studied. Shot peening response was further analyzed by measuring the induced residual stresses within the sample.

4.2 Abstract

The objective of this study was to characterize the mechanical/physical properties of an industrially processed Al-Zn-Mg-Cu powder metallurgy (PM) alloy and assess the subsequent effects of shot peening. The research involved a number of experimental techniques, including density measurements, tensile testing, Rockwell hardness measurements, nanoindentation, and optical and scanning electron microscopy. Residual stress measurements were completed using a combination of x-ray diffraction (XRD) and neutron diffraction (ND). Industrially produced specimens attained near full theoretical density and exhibited a nominal yield strength on the order of 460 MPa in the T6 condition. It was discovered that zinc had preferentially evaporated from the surface of the components during sintering. The depleted region persisted to a depth of ≈3 mm and resulted in reduced nano-hardness of 1.65 GPa at the surface versus 2.50 GPa in the bulk. Shot peening increased the surface hardness of the alloy and resulted in a peak compressive residual stress of 232 MPa at the treated surface.

4.3 Introduction

As the automotive industry continuously strives to reduce vehicle emissions there is an increasing desire for high performance, lightweight materials that can be produced in an economical manner. One option that has become progressively more attractive is that of aluminum powder metallurgy (PM). The commercial inception of this technology began in the mid 1990's with the introduction of aluminum PM camshaft bearing caps. In recent years, significant effort has been put into developing aluminum PM materials that can be

used to expand the scope of automotive applications. With 7xxx series wrought aluminum systems having some of the highest mechanical properties among all aluminum alloys, it is not surprising that alloys with similar chemistries have been devised for PM processing. One such alloy that has now matured into a commercial product is referred to as Alumix 431D. This blend was developed for press-and-sinter processing by Ecka Granules and was seemingly designed on the basis of the wrought alloy AA7075.

The open literature on this alloy is exclusively focused on laboratory processing, and more specifically, the development of optimized sintering schedules. Various studies have found that the blend responds very well to traditional press-and-sinter processing with both Martin and Castro [21] as well as Azadbeh and Razzahi [22] achieving sintered densities >98% with proper sinter temperature and time, while Pieczonka et al. [23] compared the effects of various sintering atmospheres, finding that nitrogen produced a superior sinter quality when compared to both argon and a nitrogen-hydrogen mixture. Additional studies have shown the heat treatment response to be similar to that of wrought AA7075, with LaDelpha et al. [3] finding the yield strength of the PM system in the T6 state to be approximately 91% that of the wrought system.

While there has been a considerable amount of sintering-based research dedicated to Alumix 431D, minimal data exists on its response to critical secondary operations such as shot peening. Shot peening has been extensively used in industry for years to improve the fatigue performance of wrought aluminum alloys with numerous studies published to ascertain the effects of shot peening on wrought AA7075 with varying results. Both Benedetti et al. [24] and Wagner et al. [25] saw gains in fatigue strength of approximately 50% with select peening parameters. However, others including Honda

et al. [26] and Grendahl et al. [27] saw little to no improvements in the fatigue strength of AA7075 by peening, while Oguri [28] saw no gains from conventional shot peening, but slight improvements with a fine particle shot peening process. Although there have been varying results describing the effectiveness of shot peening as a means to extend the fatigue life of AA7075, it is clear that with proper peening parameters, appreciable gains can be realized by shot peening aluminum alloys.

Overall, it is clear that Alumix 431D is a promising PM material. However, an acute lack of data in the areas of industrial processing behaviour and value-added secondary operations remain as impediments to widespread exploitation. Hence, the objective of this research was to simultaneously address both shortfalls by producing samples of the alloy in a high volume industrial production cell and then conducting a detailed metallurgical assessment of sintered specimens both before and after a conventional shot peening operation.

4.4 Materials

The material of interest in this study was the commercial Al-Zn-Mg-Cu system referred to as Alumix 431D. The blend was produced by ECKA Granules (Fürth, Germany) through air atomization and is generically denoted as PM7075 throughout the study. An SEM image of the raw powder can be seen in Figure 4-1, showing the irregular morphology typical of air atomized materials. This particular powder blend was designed for direct press and sinter processing and was formulated from a mixture of a master alloy powder containing aluminum and all alloying additions, pure aluminum powder, as well as a powdered lubricant (Licowax C; Clariant Corporation) added to aid die compaction. The

targeted and measured compositions of the PM system, found by atomic absorption, can be seen in Table 4-1.

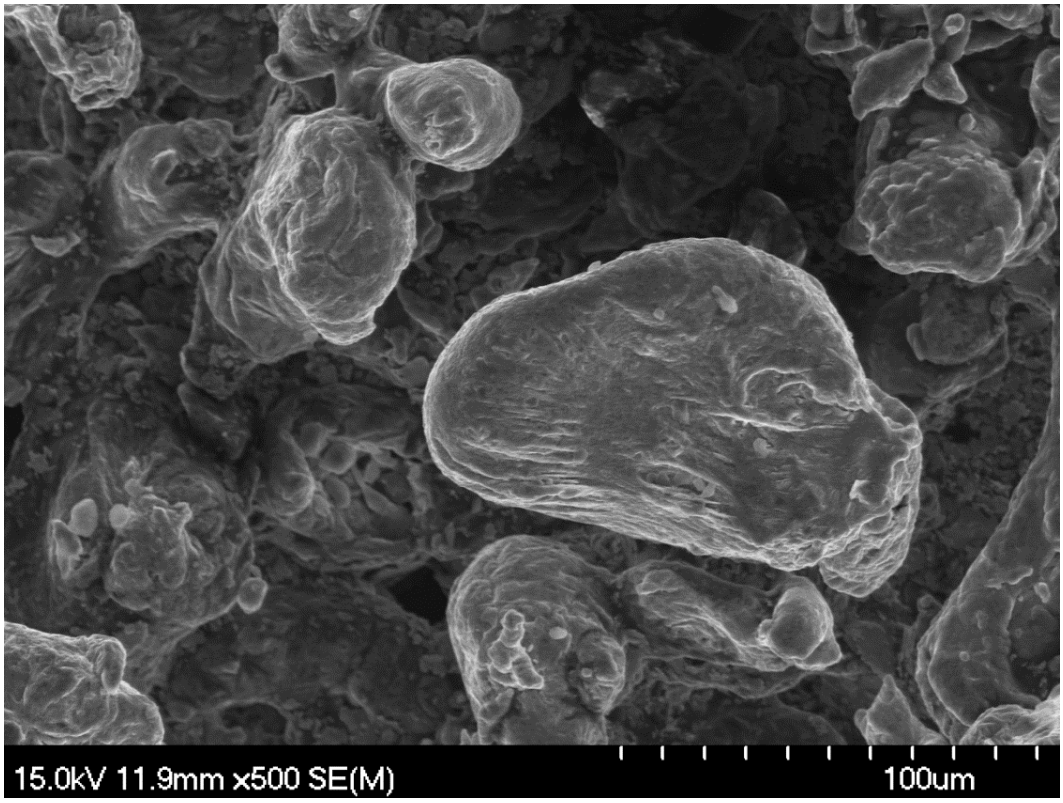

Figure 4-1 SEM image of PM7075 raw powder.

Table 4-1 Targeted and measured chemistries of PM7075 (weight %).

	Al	Cu	Mg	Zn	Sn
Target	Bal.	1.6	2.5	5.5	0.2
Measured	Bal.	1.60	2.62	5.59	0.14

4.5 Experimental Techniques

The samples for study were prepared industrially using a conventional die compaction and sintering approach. Initially, green compacts were produced through double action die compaction under an applied pressure of 400 MPa. All compacts were plate-shaped with nominal dimensions of 100 x 75 x 17 mm. The green compacts were then sintered

in a continuous mesh belt furnace under a high purity nitrogen atmosphere. The nominal thermal cycle consisted of a 20 minute dwell at 400°C for de-lubrication, followed by sintering at 605°C ± 5°C for 20 minutes and gas quenching to ambient temperature in a water jacketed section of the furnace. During the sintering process the atmospheric oxygen content was held <10 ppm while the dew point was <-60°C. All sintered plates were then heat treated to the T6 condition. This process included solutionization at 470°C for 90 minutes followed by water quenching and artificial aging at 125°C for 24 hours. Both thermal stages of heat treatment were conducted in air.

To study the effects of shot peening on the T6 material, the pucks were sectioned to a size appropriate for the automated peening system (approximately 50 x 50 mm) and the surface was peened to an Almen intensity of 0.4 mmN. Harding et al. [29] found this intensity to produce noticeable plastic deformation in the treated surface while minimizing excessive damage to the material. The tolerance on the intensity was + 0.02 mmN, - 0.00 mmN (+ 5%, - 0%) and was verified using standard N-S Almen strips before and after peening of the PM plates according to SAE J442 [30]. To minimize surface contamination of peened specimens, zirconium oxide shot was utilized as the peening media. This resulted in uniform deformation of the treated material without any obvious material transfer or damage to the shot.

Characterization of the pucks began with measurements of sintered density, apparent hardness and tensile properties. The sintered density of the samples was measured by a standard Archimedes approach coupled with oil infiltration. Hardness measurements were completed with Rockwell and nano-indentation systems. Rockwell data were gathered from the surface of T6 pucks in the HRB scale using a Leco R600 Rockwell Hardness Tester. Nano-indentation was employed to assess sub-surface hardness

gradients using an Agilent G200 system equipped with a continuous stiffness measurement module. Indentations penetrated to a depth of 1000 nm with the hardness being determined from an indentation depth of 400 to 900 nm. To determine the tensile properties of T6 specimens, heat treated pucks were sectioned and machined into threaded-end round tensile bars per ASTM E8-M [31]. Tensile testing was completed using an Instron 5594-200HVL hydraulic frame equipped with a 50 kN load cell. All specimens were loaded at a rate of 5 MPa/s with strain data collected using an Epsilon model 3542 axial extensometer that remained attached to the specimen through fracture. As such, the reported values for elongation represent the sum of elastic and plastic strain components.

The next means of characterization emphasized microstructure assessment. Here, optical and electron microscopy were employed together with x-ray diffraction (XRD) and optical profilometry. To characterize the surface condition of both the heat treated and peened materials a combination of scanning electron microscopy (SEM) and non-contact optical profilometry was utilized. Surface imaging was completed using a Hitachi S-4700 cold field emission SEM operated at an accelerating voltage of 15 kV and beam current of 10 μA. Surface topography was studied using a Nanovea Micro-Profiler, model PS50, equipped with a 1.2 mm sensor. Data acquisition was completed using Nanovea 3D software with Nanovea Mountains Pro 3D used for analysis including surface roughness measurements. For subsurface analysis, samples were sectioned perpendicular to the free sintered surface and mounted in epoxy. Mounts were then ground and polished through standard metallographic procedures. The microstructure was analyzed optically using an Olympus model BX51 optical microscope. In addition, chemical analyses were completed using a JOEL JXA-8200WD/ED electron-probe micro-analyzer (EPMA) operated at an accelerating voltage of 15 kV and equipped with

wavelength dispersive spectroscopy (WDS) detectors. XRD was employed to assess the phases present within a particular specimen and also to conduct lattice parameter measurements. Here, filings were ground from a heat treated puck, and screened to a size <45μm. The screened filings were scanned using a Bruker D8 Advance XRD equipped with a LynxEye silicon strip detector. The incident beam was Cu Kα radiation generated at 40 kV and 40 mA. The lattice parameter of the system was calculated from the peak position associated with the {422} diffraction plane. In cases where a small amount of material was required, the Nanovea Micro-Profiler, model PS50, with a 1.2 mm sensor was utilized to determine the precise volume from which the filings were extracted. These samples were then placed on a silicon single crystal zero background holder prior to XRD analyses.

To quantify the extent and gradient of residual stresses caused by shot peening, a combination of XRD and neutron diffraction (ND) was utilized. The XRD measurements were completed by Proto Manufacturing (Oldcastle, Ontario, Canada) with an LXRD 2 system using Co Kα radiation generated with an applied tube voltage and current of 25 kV and 20 mA, respectively. The measurements were completed using the {331} plane for aluminum by the psi-splitting technique with 22 tilt angles, giving an in-plane normal stress measurement as well as a shear stress value both at the surface of the sample. The x-ray elastic constant used for stress determination was a general value used for aluminum alloys, $\frac{1}{2}s_2 = 18.56 \times 10^{-6}$ MPa^{-1}. Residual stresses at depth were obtained using ND at the Canadian Neutron Beam Centre (CNBC) using the L3 spectrometer. The incident and diffracted beams were defined using 0.3 x 25 mm slits, giving a gauge volume of nominally 0.3 x 0.3 x 25 mm^3 that was stepped through the material, making measurements every ≈50 μm. A germanium single crystal monochromator was used to obtain a neutron beam with a nominal wavelength of 1.7269 Å, which yielded a

diffraction angle (2θ) of ≈90° for the {311} aluminum plane which is the preferred diffraction plane for aluminum when conducting ND measurements. A more detailed description of the technique is given by Clapham et al. [32].

4.6 Results and Discussion

Industrially processed samples of PM7075 were subjected to detailed metallurgical characterization in the conventional heat treated (T6) state and again after shot peening. Research on the former focused on mechanical properties and microstructural constituents. For the latter, efforts shifted to the characterization of peening-induced changes in surface topography and the sub-surface transitions in microstructure, hardness and residual stress.

4.6.1 Characterization of T6 Specimens

4.6.1.1 Physical and Mechanical Properties

During the industrial processing of any PM-derived component, the density of the sintered product and its uniformity are critical. As such, the industrially processed pucks were sectioned into four quadrants for discrete density measurements. The densities of the four segments were very consistent with one another, showing an average value of 2.743 ± 0.002 g/cm^3, which corresponded to 98.3% of full theoretical density (2.79 g/cm^3). Published data from LaDelpha et al. [3] for smaller lab-produced specimens showed a comparable sinter density of 2.749 g/cm^3 representing 98.4% theoretical density. Hence, despite the relatively large size of the industrially fabricated pucks, a sintered density close to full theoretical was achieved throughout the entire volume.

The variation in apparent hardness throughout heat treated pucks was also assessed. A total of 99 hardness measurements were made in 9 quadrants on the surface. The average apparent hardness and standard deviation for each quadrant are shown in Figure 4-2. Quadrant averages ranged from 82 to 86.5 HRB. Such variations were minimal and overall, good agreement was seen across the surface of the heat treated product. Interestingly, the average apparent hardness for quadrants on the left and right sides of the puck are modestly yet consistently lower than those in the quadrants in the central third of the puck, with the hardness for the quadrants at the left edge showing a slightly larger decrease in average hardness than those for the quadrants at the right edge. The orientation of the flowing nitrogen during sintering is indicated in Figure 4-2, and as will be seen in the following section may explain these hardness variations.

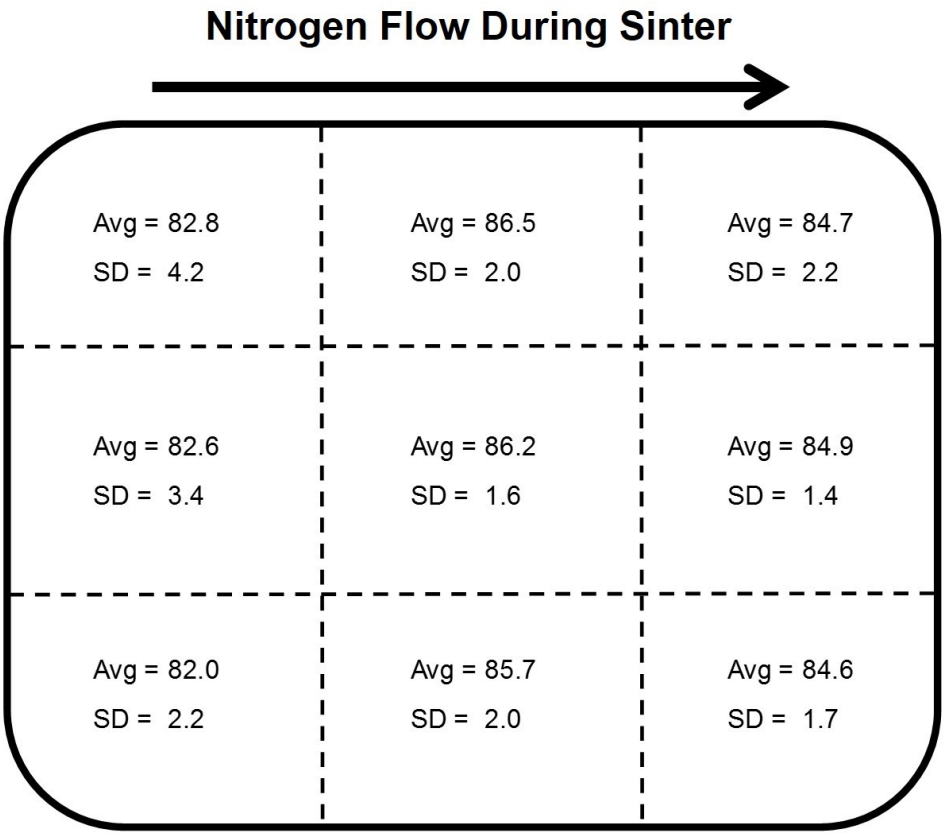

Figure 4-2 Variation in the average apparent hardness over the surface of PM7075-T6. All values reported in the HRB scale.

The tensile properties were measured using multiple specimens machined from a single industrially produced puck. Table 4-2 shows the average properties measured, as well as previously published data from LaDelpha et al. [3] derived from smaller specimens sintered in a controlled laboratory environment. Data from the industrially processed pucks were highly consistent and in excellent agreement with lab-based findings. This spoke favourably to the prospects of industrial implementation and to the scalability of laboratory developed materials.

There was no discernible trend in tensile properties as a function of position within the puck. This was in agreement with the measured uniformity of sintered density but somewhat inconsistent with the subtle trends in hardness. Thus, the differences in hardness were either too small to be reflected in the bulk tensile properties or the differences were a surface related effect that did not persist through to the core of the puck from which the tensile bars were extracted. This point was addressed in greater detail during the next stage of characterization, microstructural assessment.

Table 4-2 Tensile properties of lab and industrially produced specimens of PM7075-T6.

	Lab Produced [3]	**Industrially Produced**
Young's Modulus (GPa)	65 ± 2	65 ± 0.5
Yield Strength (MPa)	444 ± 8.1	459 ± 0.6
Ultimate Tensile Strength (MPa)	448 ± 11	465 ± 6.1
Max Elongation (%)	0.9 ± 0.1	1.0 ± 0.1

4.6.1.2 Microstructural Attributes

Optical microscopy was conducted at the centre of an industrially processed puck. The microstructure (Figure 4-3) was consistent with LaDelpha et al. [3] on laboratory processed specimens. Key attributes of the microstructure included a matrix of α-

aluminum grains (A) as the dominant feature together with isolated porosity (B), and the sporadic presence of a grey secondary phase (C). The pores were closed and rounded, indicating that a high quality sinter was obtained.

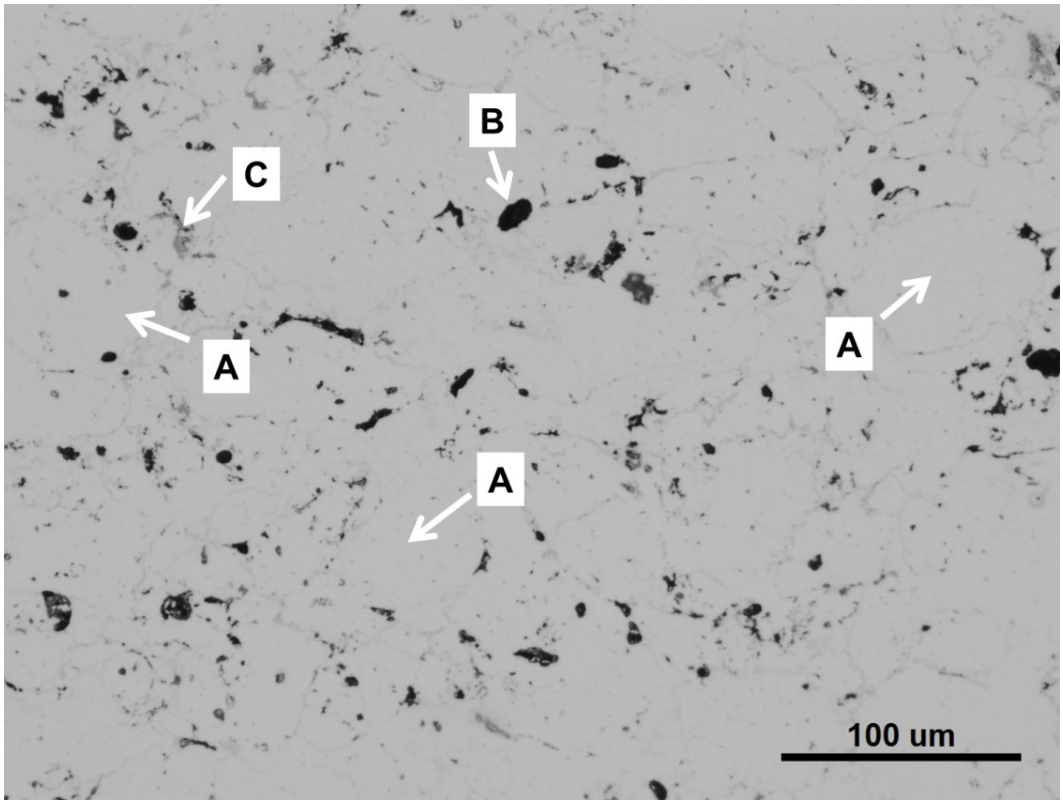

Figure 4-3 Core microstructure of industrially processed PM7075-T6.

During prior lab processing, zinc build up was observed within the exhaust of sintering furnaces. This implied that zinc was being lost to the atmosphere during sintering and that a chemical gradient may exist near the surface of both laboratory and industrially sintered specimens. To assess this possibility, a section was removed from the center of an industrial processed T6 puck, mounted, polished and examined through EPMA/WDS. Through-thickness variations in the concentrations of zinc, magnesium, copper and tin extending from the free surface during sintering (0 mm) completely through to the belt facing surface (17 mm) are shown in Figure 4-4. The data shows that

the puck had lost a significant amount of zinc in the vicinity of the free surface (Figure 4-4 (a)) during processing. The zinc concentration began with an appreciable decrease at the free surface dropping to a value of approximately 3.1 wt%. The concentration increased with depth, stabilizing at a depth of ≈3 mm within the sample to a value consistent with the bulk assay of the alloy (≈5.6 wt% as indicated in Table 4-1). The concentration decreased again near the surface that was in contact with the furnace belt, though it did not reach as low a value as was observed at the free surface (4.7 wt.% vs 3.1wt.%). The magnesium concentration, Figure 4-4 (b), showed a considerable amount of scatter, but there were no clear trends near either surface as seen in the zinc profile. This was also the case for copper and tin contents, although less scatter was observed. For each spike in magnesium concentration, there is a corresponding increase in tin concentration, Figure 4-4 (d). It is postulated that these particular points were close to grain boundaries within the system, where locally higher concentrations of magnesium and tin often exist in sintered aluminum alloys owing to the formation of the thermodynamically stable phase Mg_2Sn as found by MacAskill et al. [12].

Of all the elements present in PM7075, zinc has by far the highest vapour pressure at the sintering temperature employed (1640 Pa). Aluminum, copper and tin are relatively non-volatile, exhibiting vapour pressures of only 5.51×10^{-8}, 3.72×10^{-9} and 5.06×10^{-8} Pa, respectively, calculated based on properties given by Brandes [33]. Magnesium has a vapour pressure of 144 Pa, which is still an order of magnitude less than that for zinc. Based on these values it is clear that zinc had the greatest propensity for evaporation among the elements present. As such, the observed near-surface loss of zinc was a valid result well supported by fundamental thermodynamic concepts.

The Al-Zn-Mg-Cu alloy family exhibits some of the highest strengths of all aluminum based systems. This largely stems from the η-type precipitation sequence wherein meta-stable variants of $MgZn_2$ are formed in the α-aluminum grains. Delasi and Adler [34] showed these precipitates evolve according to Eq 4-1.

$$SSSS \rightarrow GP\ Zones \rightarrow \eta'(MgZn_2) \rightarrow \eta(MgZn_2) \qquad (Eq\ 4-1)$$

In the T6 temper, the system represents a peak hardened state wherein a high concentration of Guinier-Preston (GP) Zones and the semi-coherent η' precipitate phase reside within the alloy. The noted decrease in zinc concentration at the exterior surfaces of sintered pucks would invariably reduce the concentrations of these phases, thereby weakening the system at the exterior surface. As noted earlier, the industrial processed plates were sintered in a continuous mesh belt furnace. Here, pucks are placed on the belt that draws them into the heated zones of the furnace in a direction that is counter-current to the flowing nitrogen atmosphere. In this situation, the zinc vapour would be swept away from the puck as it evolved, prompting continual growth of the zinc lean surface layer. Furthermore, this effect should be particularly intense on the leading edge of the puck and along any other free surfaces for which evaporation is not inhibited by obstructions such as the furnace belt itself. Lower average hardness values were consistently noted along the leading edge of pucks (Figure 4-2), consistent with these observations.

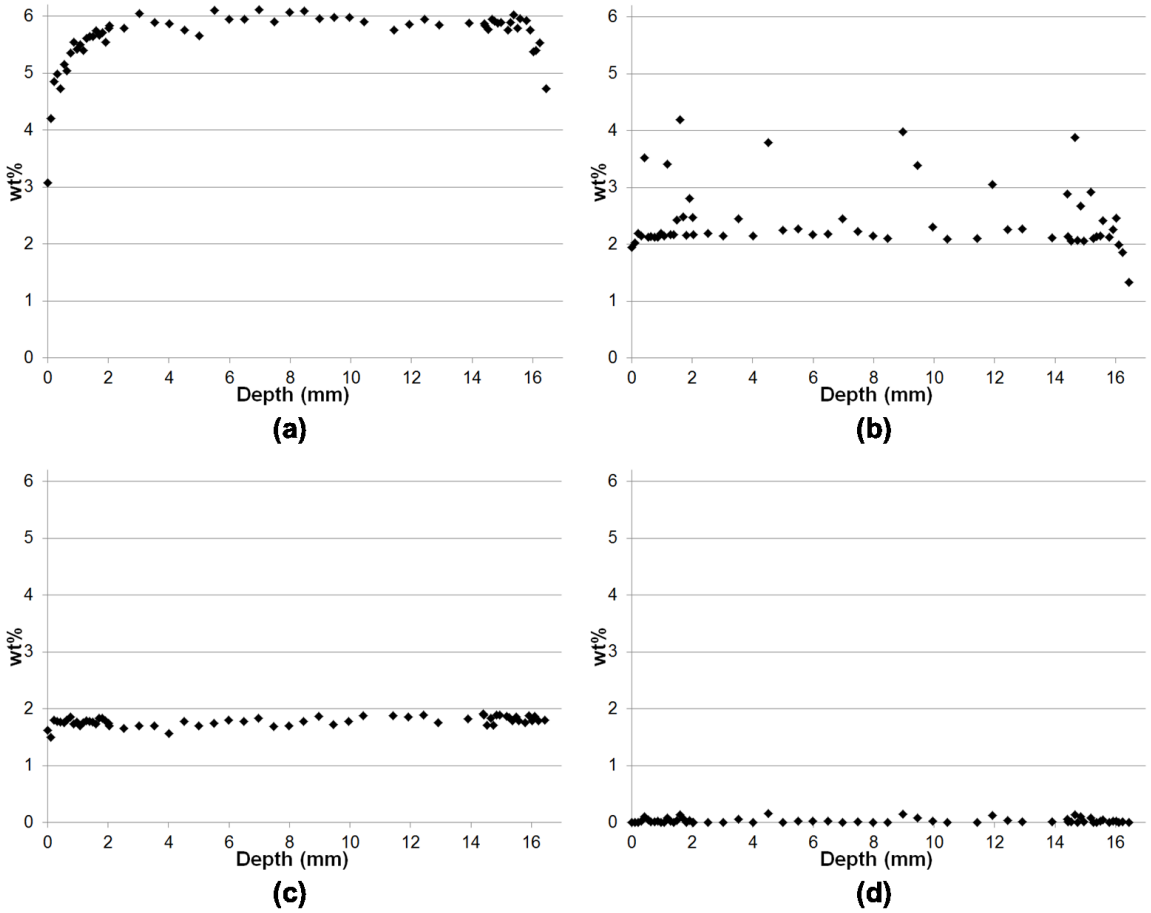

Figure 4-4 Through thickness variations in the concentrations of (a) zinc, (b) magnesium, (c) copper, and (d) tin within an industrially produced puck of PM7075-T6.

To assess the effect of near-surface zinc loss in greater detail, hardness was measured as a function of depth via nano-indentation (Figure 4-5). The puck showed a decreased hardness at the surface (≈1.65GPa) which then stabilized at a value of approximately 2.50 GPa. Interestingly the trend did not continue to a depth similar to the zinc loss seen in Figure 4-4 (a), with the drop being present only to a depth of ≈1 mm where the zinc gradient was seen to exist to a depth of ≈3 mm.

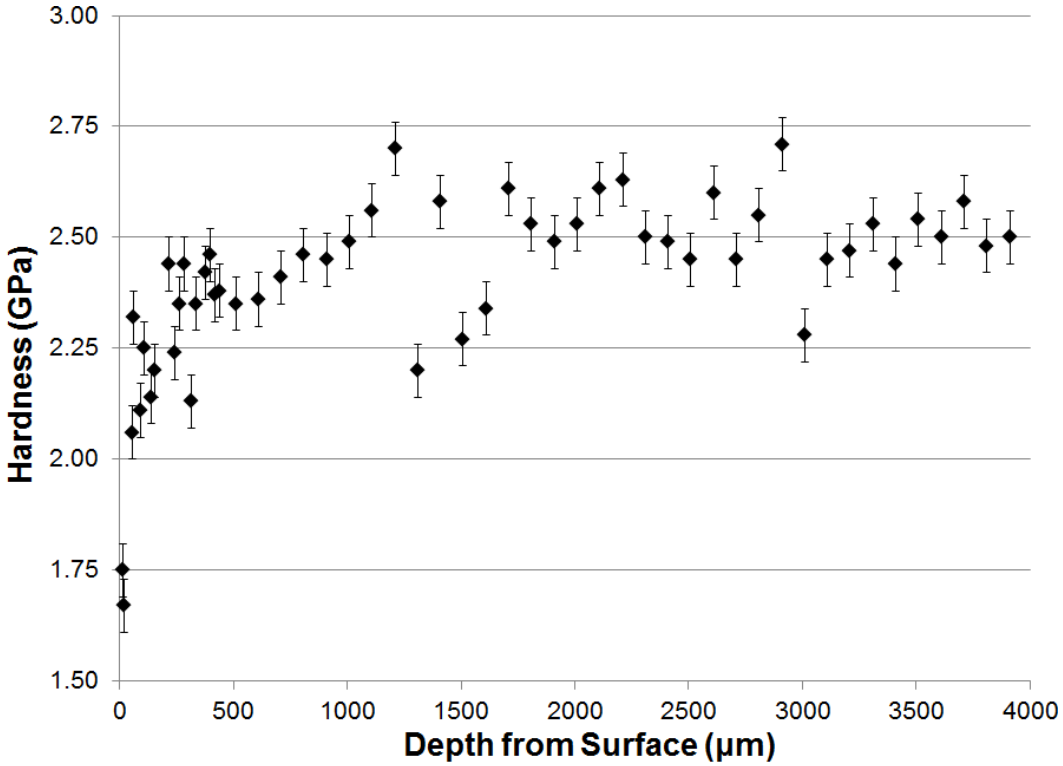

Figure 4-5 Hardness profile recorded at the centre of a puck of PM7075-T6 from the top surface (0 mm) inward.

As a further indication of the effect this zinc loss has on the system, the lattice parameter was measured using XRD. Figure 4-6 shows the XRD trace for filings taken from the centre of aT6 puck. All the diffraction peaks agreed closely with the theoretical peak positions for pure aluminum. This was a further indication of the heat treatment producing largely a GP zone structure, as no secondary η' or η precipitate phases were detected. It also agrees with the micrographs of the system (Figure 4-3) showing largely α-aluminum, with only trace amounts of secondary phases present.

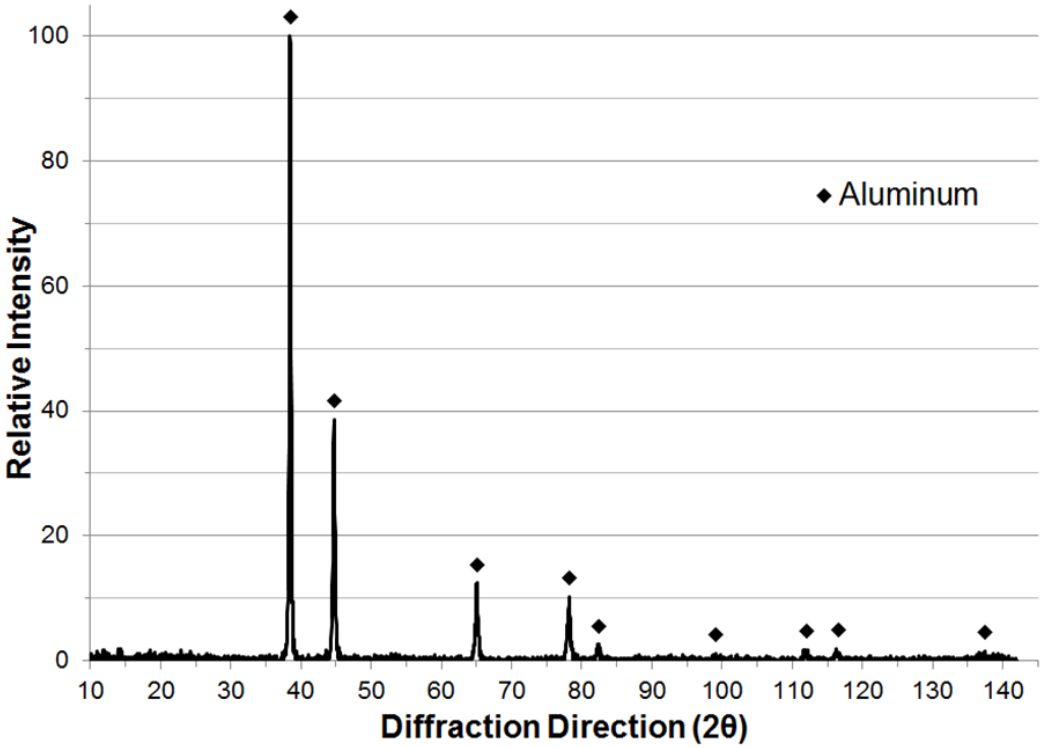

Figure 4-6 XRD trace for PM7075-T6.

To assess the effect of zinc loss on the lattice parameter, filings were taken from the centre, away from the zinc depleted region as well as from the surface, where the sharpest gradient was measured. Using a non-contact surface profiler, it was determined that the surface filings came from the upper 30 μm of the specimen. The screening of the filings resulted in particles with a size below 45 μm, which Noyan and Cohen [35] state should result in particles that would not have any macroscopic residual stresses present. Therefore, it should have been evident if the noted loss in zinc had caused any changes to the lattice parameter of the material. The {422} diffraction peaks for filings taken from the centre and the surface of the material are shown in Figure 4-7. The centres of the peaks were found by the chord midpoint at full width half max (FWHM). There was very little change seen in the peak positions, with the centre filings showing a peak position of 137.088° and the surface filings showing a peak position of

137.072°. Using Bragg's Law along with the cubic structure of the system, the lattice parameter of the system (*a*) was found to be 4.0547 Å in the centre, and 4.0549 Å at the surface. This variation in peak position is also within the stated accuracy of the XRD system, 0.02°. From this, the zinc depletion did not appear to have any significant effect on this crystallographic attribute. This was not surprising, as Hatch [4] shows zinc as having a very small effect on aluminum, changing the lattice parameter of the system by only -0.0075 Å/at%.

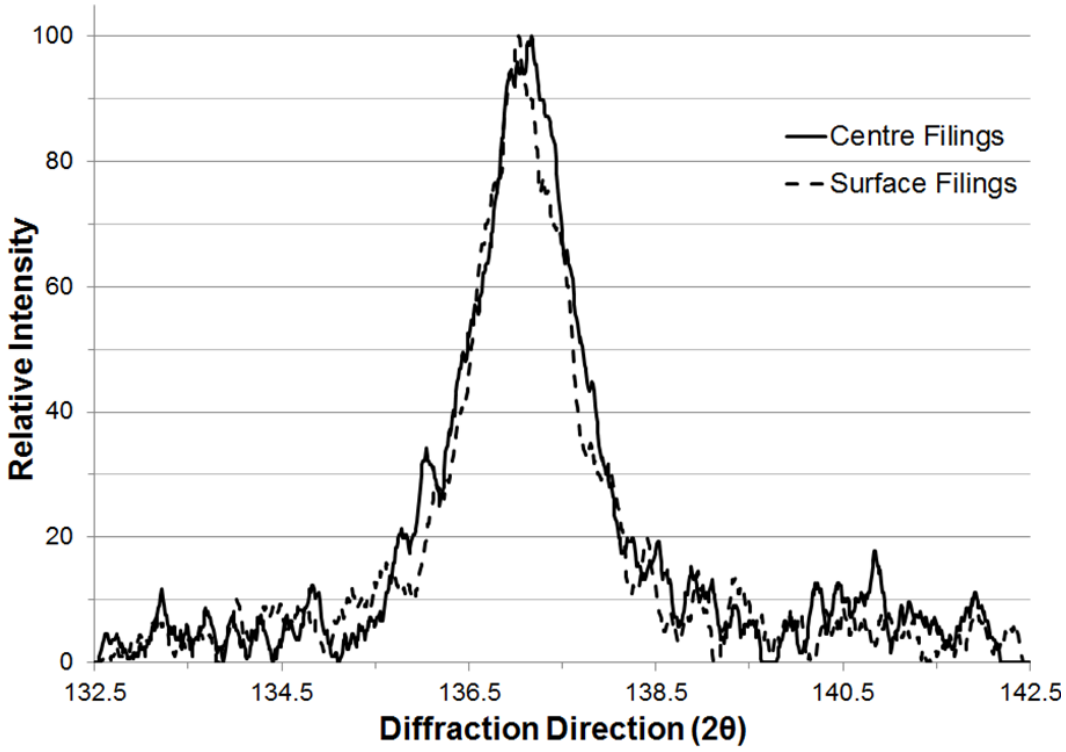

Figure 4-7 Comparison on the {422} diffraction peaks recorded from the central and surface regions of PM7075-T6 puck.

4.6.2 Effects of Shot Peening

To assess the response of PM7075-T6 to shot peening, heat treated pucks were peened to an intensity of 0.4 mmN and characterized. Core means of assessment included a

characterization of the general surface attributes and the measurement of sub-surface gradients in hardness and residual stress.

4.6.2.1 Surface Assessment

SEM images of the heat treated as well as peened surfaces can be seen in Figure 4-8. Noticeable deformation caused by shot peening was observed. Although there appeared to be some damage around the impact craters, it was not deemed excessive as observed with higher intensity peening shown by Harding et al. [29]. The surfaces of both materials were scanned using optical profilometry to quantify the surface roughness (S_a), resulting in a measured value of 6.61 μm for the T6 sample and 6.12 μm for the T6/peened specimen. The modest decrease in surface roughness due to peening was viewed as beneficial as it could be associated with fewer and less severe stress concentrators at the surface

Shot peening of ferrous PM materials has given rise to significant sub-surface densification in some instances, with Molinari et al. [36] finding shot peening to create essentially a fully dense surface layer continuing to a depth of approximately 50 μm in a Cr-Mo steel with bulk sintered density of ≈90%. In an attempt to determine if a similar phenomenon had occurred in PM7075-T6, the microstructures beneath sintered and sintered/peened surfaces were examined using optical metallography (Figure 4-9). In this instance, there was no clear evidence that sub-surface densification had taken place. However, a localized peening-induced density increase would not be readily discernible given that the material had sintered to a density that approached full theoretical (> 98%).

To determine if the peening process caused any sub-surface hardening, hardness was measured as a function of depth via nano-indentation on a shot peened specimen. The resultant profile is shown in Figure 4-10. The hardness varied little with depth, maintaining a constant level of ≈2.5 GPa. Although hardness values were not obviously higher in the zone immediately adjacent to the peened surface (which is commonly seen in peened materials as a result of strain hardening, as reported by both Was et al. [37] and Rodopoulos et al. [38]), the softened layer noted in the unpeened specimen (Figure 4-5) was no longer present. This indicated that the plastic deformation associated with peening had work hardened the surface to an extent that offset the softening imparted by the preferential volatilization of zinc.

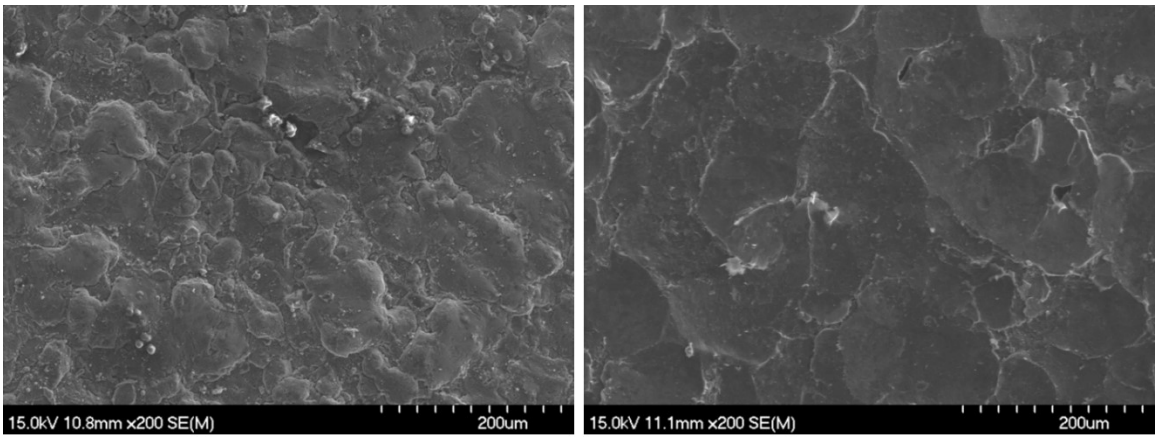

(a) (b)

Figure 4-8 General surface appearance of PM7075-T6 (a) before (b) after shot peening.

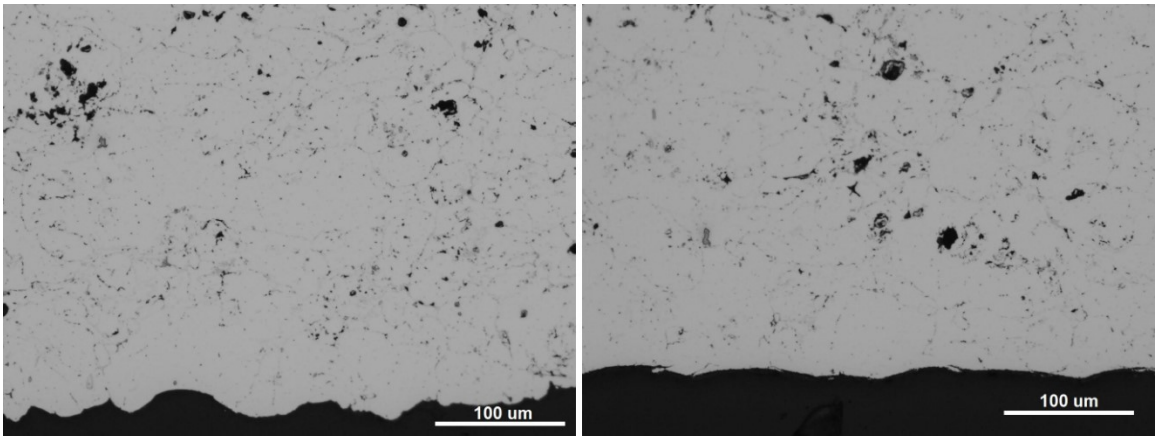

(a) (b)

Figure 4-9 Subsurface microstructure of heat treated (a) and peened (b) PM7075-T6.

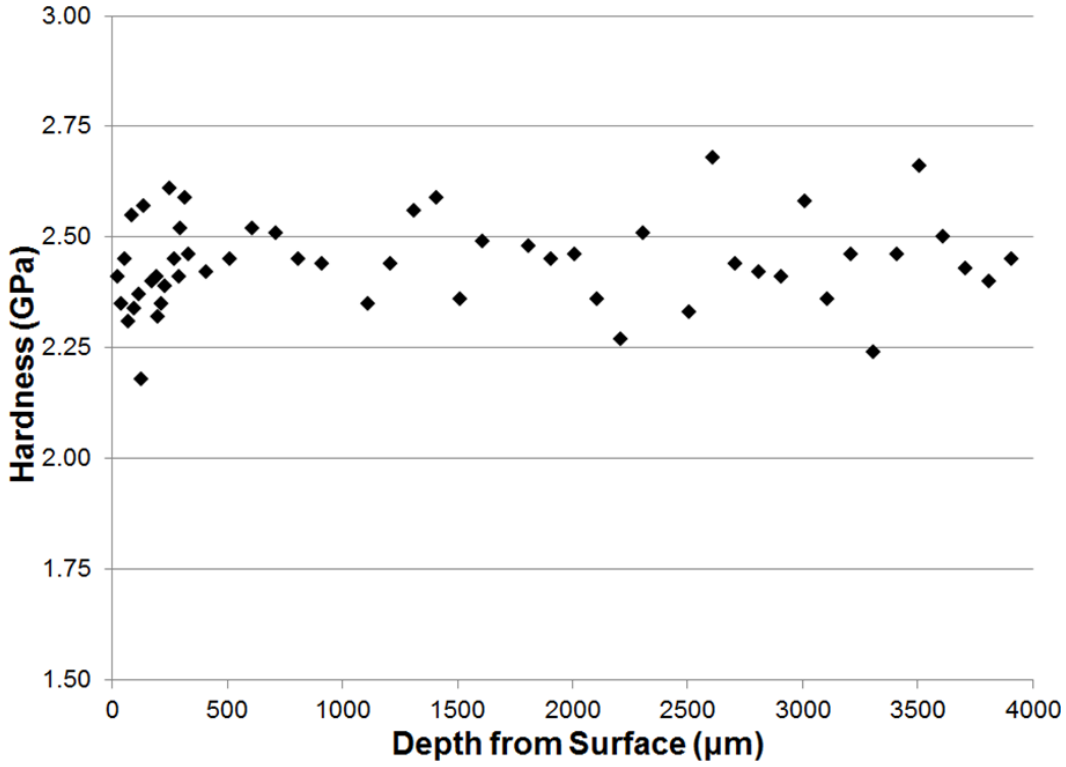

Figure 4-10 Hardness profile recorded at the centre of a shot peened puck of PM7075-T6 from the top surface (0 mm) inward. Specimen was peened to 0.4 mmN intensity.

4.6.2.2 Surface Residual Stress Measurements

XRD was used to measure the in-plane stress in the surface layer of PM products. A specimen in the T6 heat treated condition was scanned as was a sample peened to 0.4 mmN intensity. Three scans were completed on the surface of each specimen at 45° to one another to determine the isotropy of the surface in-plane stresses present. The resultant values are given in Table 4-3. As is expected, the heat treatment process itself resulted in an appreciable level of compressive residual stress at the surface of the component. This phenomenon has been well documented for wrought aluminum alloys and studied in depth by Robinson et al. [39, 40] as well as Becker et al. [41], and is largely driven by the quenching stage of the heat treatment sequence. After solution heat treatment at an elevated temperature the material is quenched into water. Upon contact with water differential cooling invariably occurs between the surface and bulk of the material. When equilibrium is eventually reached, the interior material is in a state of tension, while the outer surface is in compression. During ageing, these residual stresses may be reduced, but short of fully stress relieving the material, they will persist.

Table 4-3 In-plane residual stresses measured at the surface of PM7075-T6 specimens processed with and without shot peening.

Sample Condition	Residual Stress (MPa)		
	0°	45°	90°
T6	-64 ± 9	-58 ± 9	-60 ± 8
T6 + Peening	-232 ± 3	-234 ± 3	-231 ± 2

The shot peening process resulted in a factor of four increase in the level of compressive residual stress at the surface over the heat treated sample. This level of stress was comparable to values reported by Benedetti et al. [24] for wrought AA7075-T6, and represents approximately 50% of the yield strength of the material. It was also noted

that the residual stress was consistent throughout the surface of the peened samples. This was a result of the isotropic deformation that took place upon shot impact and indicated that the specimens responded to peening in an isotropic manner in the treated surface (i.e. there was no anisotropic behavior which may result from, for instance, texture within the surface).

4.6.2.3 Through Thickness Residual Stress

Through thickness residual stress measurements were completed by ND. Two normal strain components were measured, one parallel to the free surface, and one perpendicular to it. It was assumed that the near surface in-plane strains due to peening were isotropic, which was supported by the XRD measurements (Table 4-3). It was also assumed that these measurements were made in the principal directions. This should be the case when considering residual strains caused by shot peening as the three principal directions should lie with one normal to the surface and two in-plane.

The unstressed lattice parameter (a_o or interplanar spacing d_o) was found as discussed previously in Section 4.6.1.2, which followed the procedure recommended by Noyan and Cohen [35]. The major causes for change in the lattice of a crystalline metallic material include alloying additions and residual stresses. Although a gradient in zinc concentration was found to exist within PM7075 (Figure 4-4 (a)), this did not appear to have any significant effect on the lattice parameter of the system as noted earlier. As such, a single value for the unstressed lattice parameter was used for all the strain calculations by ND as a function of depth. This value was a_o = 4.0548 Å; an average value of the measurements completed on PM7075-T6 per Figure 4-6.

Knowing this unstressed lattice parameter and the measured peak positions as a function of depth via ND, the lattice strain was found using Eq 4-2:

$$\varepsilon = \frac{d - d_o}{d_o} = \frac{\sin\theta_o}{\sin\theta} - 1 \qquad (Eq\ 4-2)$$

In Eq 4-2, *d* is the plane spacing, here for the {311} plane in the stressed condition, with a corresponding scattering angle of 2θ, and d_o is the stress-free {311} plane spacing, corresponding to a scattering angle of $2\theta_o$. The residual lattice strains (in-plane and normal) in shot peened PM7075-T6 are plotted in Figure 4-11.

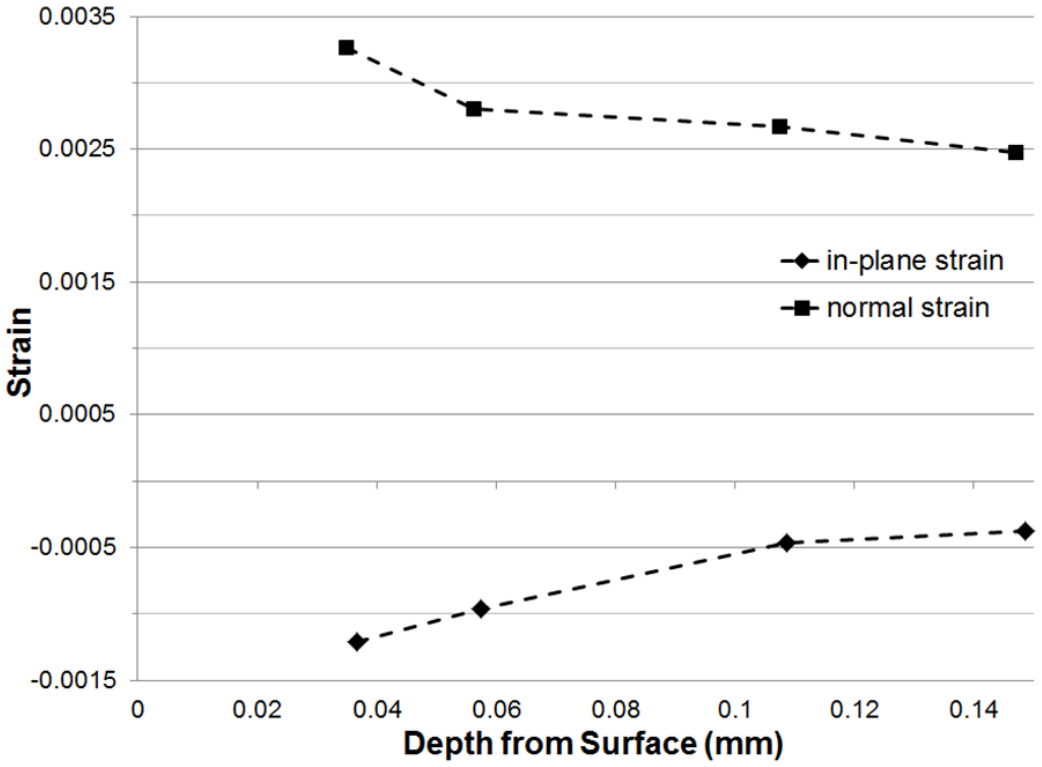

Figure 4-11 In-plane and normal strains measured in shot peened PM7075-T6.

As expected, the peening resulted in compressive in-plane residual strain at the surface. This was a result of plastic deformation, causing the surface material to flow laterally.

This lateral flow was resisted by inner material, leaving the surface layer in a compressive state. Due to the Poisson effect, the strain perpendicular to the surface was then in a tensile state. However, the level of tensile residual strain was quite surprising, with the magnitude being considerably higher than the in-plane compressive residual strain (Figure 4-11). XRD measurements were used to confirm this result. Here, a peened sample was scanned using XRD normal to the surface with Cu and Co radiation sources. Comparing the measured peak positions to the unstressed lattice parameter of the system, normal strain values of 0.002351 and 0.001910 were deduced for Cu and Co radiation respectively. Although XRD measurements are usually regarded as surface measurements, there is in fact a probed volume associated with the analysis due to x-ray absorption. Hence, a particular strain measurement derived through XRD does not correspond to a true surface measurement, but actually to a narrow depth beneath it.

To determine the actual depth value, the maximum depth probed by the x-rays was first quantified using Eq 4-3:

$$I_x = I_o e^{-\left(\frac{\mu}{\rho}\right)\cdot \rho \cdot x} \qquad (Eq\ 4-3)$$

Where I_x is the transmitted intensity, I_o is the incident intensity, μ/ρ is the mass absorption coefficient found for PM7075 (50.81 cm^2/g for Cu radiation and 78.22 cm^2/g for Co radiation based on chemical composition), ρ is the alloy density (2.79 g/cm^3) and x is the distance traveled through the material.

Eq 4-3 is based on the maximum distance an x-ray will travel through a material when the incident trajectory is normal to the material surface. Hence, when the incident beam is non-orthogonal (as is the case in diffraction measurements) the actual probed depth will differ from the calculated maximum. To account for this factor, the true maximum penetration depth was found for each radiation source using Eq 4-4 and the known diffraction angle θ for the plane in question ({422} using Cu radiation and {331} for Co):

$$d = \tfrac{1}{2} x \sin\theta \qquad (Eq\ 4-4)$$

Where *d* is the depth of the probed volume, *x* is the distance traveled by the x-ray and θ is the angle of diffraction.

From Eq 4-3 and 4-4, the true penetration depth that would have accounted for 99.9% of the diffracted x-rays (I_x = 0.1, I_o = 100) was determined. The corresponding values were calculated to be 226 μm and 152 μm for Cu and Co radiation respectively. Although these particular depths were those associated with 99.9% of the diffracted x-rays, a disproportionately large fraction of the diffracted beam would originate from a region close to the surface. Hence, to determine the average depth of the measurement, Eq 4-3 and 4-4 were then combined and integrated with respect to the depth, *d*, resulting in Eq 4-5:

$$\int I_o e^{-\mu/\rho \cdot \rho \cdot 2d/sin\theta}\, dd = \frac{-I_o sin\theta}{2 \cdot \frac{\mu}{\rho} \cdot \rho} e^{-\mu/\rho \cdot \rho \cdot 2d/sin\theta} \Bigg]_0^{depth} \qquad (Eq\ 4-5)$$

This solution gives the area under the curve of the transmitted intensity equation. By solving Eq 4-5 based on the total depth that the diffracted beam probes (per Eq 4-4) the area can then be divided by two so as to determine the true average depth probed. Hence, it was found that the average depth of the XRD measurement was 22.6 μm for Cu radiation and 15.2 μm for Co radiation.

The values for the normal component of strain found by XRD are summarized in Table 4-4. These XRD-derived measurements were consistent with the ND data (Figure 4-11). Hence, combining data from the two techniques yielded a plot with the expected trend for normal strain versus depth. While the normal strain at the surface will not necessarily fall to zero, it should be a minimum at this position due to the free surface. It should then increase with depth into the material, reach a maximum, and finally decrease to a static value. The measured values of this study showed this very trend (Figure 4-12).

Table 4-4 Summary of the normal strains and the corresponding measurement depths within peened PM7075-T6 found using Cu and Co radiation.

Radiation Source	**Cu**	**Co**
Diffraction Peak {hkl}	422	331
Angle of Diffraction 2θ, °	136.4	147.3
Mass Absorption Coefficient μ/ρ, cm^2/g	50.81	78.22
Depth Associated with 99.9% of Diffracted Beam, μm	226	152
Average Depth of Measurement, μm	22.6	15.2
Normal Strain, mm/mm	0.002351	0.001910

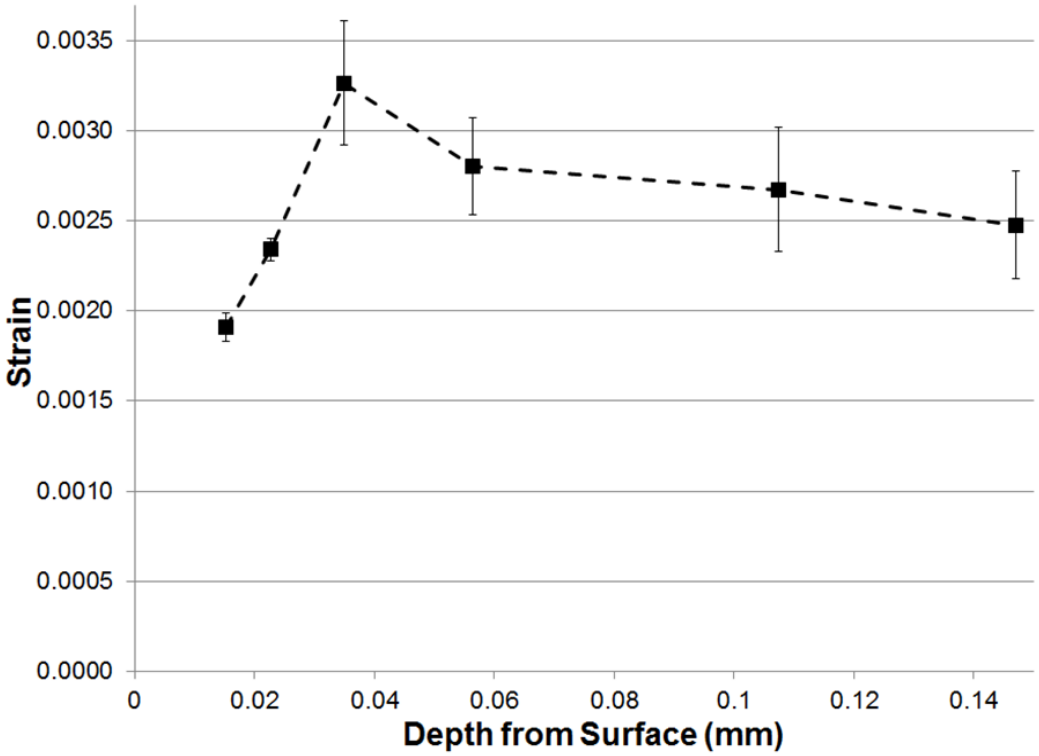

Figure 4-12 Normal component of strain measured in shot peened PM7075-T6. The first two points correspond to XRD data and the remainder to ND data.

Once the strain values were known, the residual stress within the system could be determined using linear elastic theory. The expanded forms of Hooke's law for the three principal directions are given as Eq 4-6 and 4-7:

$$\sigma_{1,2} = \frac{E}{(1+\nu)(1-2\nu)}\left[(1-\nu)\varepsilon_{1,2} + \nu\left(\varepsilon_{2,1} + \varepsilon_3\right)\right] \qquad (Eq\ 4-6)$$

$$\sigma_3 = \frac{E}{(1+\nu)(1-2\nu)}\left[(1-\nu)\varepsilon_3 + \nu(\varepsilon_1 + \varepsilon_2)\right] \qquad (Eq\ 4-7)$$

Where $\sigma_{1,2}$ represent the principal stresses in-plane, σ_3 represents the principal stress normal to the surface, $\varepsilon_{1,2,3}$ are the corresponding measured principal strain values, and E and ν are Young's modulus and Poisson's ratio for the material, respectively.

The values used for *E* and *v* should be specific to the given diffraction plane used for the measurements; here, the {311} plane for ND work. These values are commonly used in x-ray stress measurements in the form of x-ray elastic constants (XEC) for a specific diffraction direction termed s_1 and $½s_2$ and are defined by Eq 4-8 and 4-9:

$$s_1 = \frac{-\nu_{hkl}}{E_{hkl}} \qquad (Eq\ 4-8)$$

$$½s_2 = \frac{1+\nu_{hkl}}{E_{hkl}} \qquad (Eq\ 4-9)$$

As the majority of x-ray measurements rely only on $½s_2$, published values of both of the XEC's needed to determine the values of *E* and *v* for a given diffraction plane are not easily found. For this reason, a theoretical model was used to calculate *E* and *v* for the {311} diffraction direction. The Kröner model, described in detail by Murray [42], predicts the elastic response of a polycrystalline single phase material for a given diffraction direction. This model uses the single crystal elastic properties of the material, along with bulk properties to determine the anisotropic behaviour of the crystal system. This model assumes a perfectly random grain orientation (no texture) as well as spherical grains. Both of these assumptions are valid for PM materials as no texture would be present due to the nature of press-and-sinter PM processing and the fact that a high quality sinter was observed wherein equi-axed grains prevailed (Figure 4-3). The single crystal elastic constants (C_{ijkl}) used were those for AA7075-T6 given by Logé et al. [43], where C_{1111} = 84.00 GPa, C_{1122} = 39.25 GPa, and C_{1212} = 55.24 GPa. Similarly, bulk values of *E* (71.0 GPa) and *v* (0.33) for AA7075-T6 were taken from ASM Handbook [44] and implemented in the Kröner model. Resultant values of the XEC's for the {311} plane of AA7075 were found to be s_1 = -3.47 x 10^{-6} MPa^{-1} and $½s_2$ = 16.57 x 10^{-6} MPa^{-1}. This

value of $\frac{1}{2}s_2$ also agrees very well with measured values for wrought AA7075 in the {311} diffraction direction by Prevey [45] ($\frac{1}{2}s_2$ = 16.43 x 10^{-6} MPa^{-1}) giving confidence in the calculated XEC values. Using these calculated values along with Eq 4-8 and 4-9, the values for E and v in the {311} diffraction direction were found to be 76.33 GPa and 0.27, respectively.

Due to the chemical similarity of AA7075 and the PM system of interest, the aforementioned values for E{311} and v{311} were used to determine the stresses present in the PM materials of this work. The resultant in-plane residual stress profile is given in Figure 4-13, with the first point representing the value deduced through XRD (Table 4-3). The in-plane residual stress was the only component considered since this is the beneficial stress that opposes tensile loading in the surface of an engineered product. The residual stress was compressive on the surface of the peened specimen and transitioned into a tensile condition at a depth of 60-100 μm. This was in good agreement with published data on wrought AA7075-T651 wherein a compressive layer thickness of approximately 75 μm was measured by Benedetti et al. [24]. Under these peening conditions the wrought alloy experienced a 47% increase in its fatigue endurance limit. As such, research is now ongoing to determine if the comparable compressive surface layer observed in PM7075-T6 will impart tangible gains in the fatigue performance of this PM material as well.

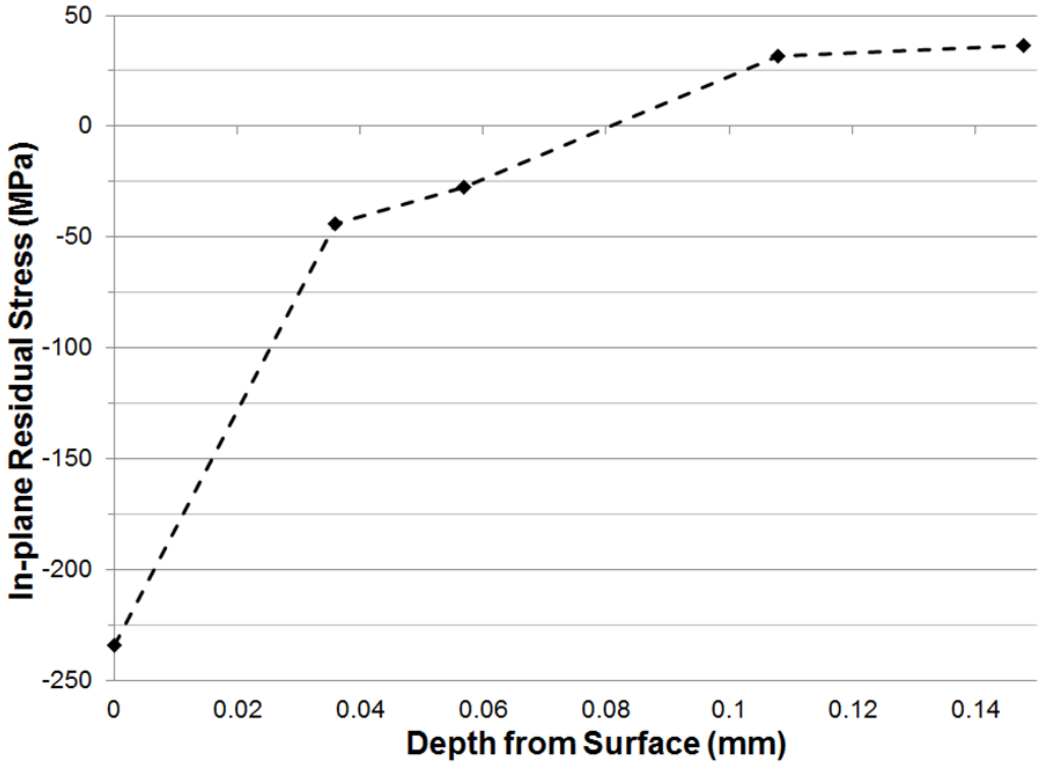

Figure 4-13 Residual stress depth profile determined for shot peened PM7075-T6.

4.7 Conclusions

From the work completed in this study the following conclusions were reached:

1. PM7075 responded very well to industrial processing, resulting in properties on par with laboratory processed specimens despite the appreciably larger size of the industrially manufactured parts.
2. It was found that industrial sintering had induced a heterogeneous loss of zinc from the component surfaces. The lowest concentration of zinc fell to 3.1 wt% but then stabilized to the nominal bulk value (5.6 wt%) at a sub-surface depth of 3 mm.
3. Near surface zinc loss was accompanied by a localized decrease in nanoindentation hardness down to 1.65 GPa from a nominal core value of 2.50 GPa.

4. Shot peening imparted appreciable strain hardening at the surface of PM7075-T6 so as to increase subsurface hardness and thereby offset the softening effect imparted by the evaporative loss of zinc.
5. Shot peening resulted in an appreciable level of compressive residual stress within PM7075-T6. This compressive stress persisted to a total depth of 60-100 μm below the surface and at its peak magnitude, was over four times larger than that instilled in the alloy through heat treatment alone.

4.8 Acknowledgements

The authors would like to acknowledge the financial support provided by the Natural Sciences and Engineering Research Council of Canada via Discovery grant no. 250034 as well as the Postgraduate Doctoral Scholarship (PGS-D) program. The provision of all powdered metals by Dr. Bernd Mais of Ecka Granules is gratefully acknowledged as are machining provided by Dean Grimm and assistance with EPMA by Dr. Dan MacDonald, both of Dalhousie University.

Chapter 5: Effects of Post-Sinter Processing on an Al-Zn-Mg-Cu Powder Metallurgy Alloy

Matthew David Harding[1], **Ian William Donaldson**[2], **Rich Lester Hexemer Junior**[2], **Donald Paul Bishop**[1,*]
1 – Department of Mechanical Engineering, Dalhousie University, Halifax, NS, B3H 4R2, Canada
2 – Advanced Engineering, GKN Sinter Metals LLC , Auburn Hills, MI, 48326, USA
* Corresponding Author – Paul.Bishop@dal.ca; Phone 1.902.494.1520

Status: Published. Metals 2017, vol. 7, iss. 9, 370.

Author Contributions: The experimental procedure was developed jointly by M.D. Harding and D.P. Bishop, with input from I.W. Donaldson and R.L Hexemer Jr. Sintering of the alloy was completed by R.L Hexemer Jr., with all other experimental work carried out and compiled by M.D. Harding, along with first draft of the manuscript. The current state of the manuscript is a result of editing by all four authors.

5.1 Forward to Chapter 5

Keeping with the industrial focus of the work from Chapter 4, key secondary operations required in industry were incorporated (primarily the effects of sizing and heat treatment). Sizing was studied in two distinct sequences, with it being applied in the T1 state followed by a standard T6 heat-treatment (Size-Sol-Age), as well as an interrupted step during the heat-treatment, between quenching and artificial aging (Sol-Size-Age). When applied as an interrupted step, the bars were naturally aged after quench for 30 min prior to sizing being applied. Focus was placed on the fatigue properties of the alloy, with shot peening again considered to increase fatigue strength. With industrial processing a primary concern, fatigue testing was switched from RBF (as undertaken in Chapter 3) to 3-point bend loading, and similar to previous RBF testing was completed in a non-controlled, open atmosphere. This was mainly due to the desire to test the parts

in the press-and-sintered state, avoiding any machining (which is required for RBF testing). As thermal exposure is known to degrade the beneficial compressive residual stress imparted by shot peening, and can be commonly encountered in service, the effects of thermal exposure were also considered.

5.2 Abstract

The objective of this work was to study the effects of several post-sinter processing operations (heat-treatment, sizing, shot peening) on a press-and-sinter 7xxx series aluminum powder metallurgy (PM) alloy. The characterization of the products was completed through a combination of non-contact surface profiling, hardness measurements, differential scanning calorimetry (DSC), transmission electron microscopy (TEM), X-ray diffraction (XRD), tensile, and three-point bend fatigue testing. It was determined that sizing in the as-quenched state imparted appreciable reductions in surface hardness (78 HRB) and fatigue strength (168 MPa) relative to counterpart specimens that were sized prior to solutionizing (85 HRB and 228 MPa). These declines in performance were ascribed to the annihilation of quenched in vacancies that subsequently altered the nature of precipitates within the finished product. The system responded well to shot peening, as this process increased fatigue strength to 294 MPa. However, thermal exposure at 80°C and 160°C then reduced fatigue performance to 260 MPa and 173 MPa, respectively, as a result of residual stress relaxation and in-situ over-aging.

5.3 Introduction

Press-and-sinter aluminum powder metallurgy (PM) is an ever-growing industry due to the cost savings associated with high production rates and net shape capabilities

coupled with the advantageous strength-to-weight ratio inherent to aluminum alloys. Much of this growth has been underpinned by the development of improved PM alloy formulations, with most lying within the general scope of 2xxx (Al–Cu–Mg) [46, 47], 4xxx (Al-Si-Cu-Mg) [48], or 7xxx (Al-Zn-Mg-Cu) [3, 49] chemistries. Accordingly, all such systems incorporate precipitation hardening as a key strengthening mechanism. Within this context, new aluminum PM alloys chemically compliant with the 7xxx series offer particularly high strength-to-weight ratios and are of natural commercial interest.

The traditional precipitation sequence believed to occur in wrought 7xxx series aluminum alloys was originally stated as [50]:

$$SSSS \rightarrow GP\ Zone \rightarrow \eta' \rightarrow \eta \qquad (Eq\ 5-1)$$

Here, the metastable super saturated solid solution (SSSS) is formed upon quenching from the solutionization temperature. It then decomposes during natural or artificial aging, through the formation of clusters of solute atoms (so called Guinier–Preston (GP) zones) that eventually transform into the semi-coherent phase η' and finally the fully incoherent phase η ($MgZn_2$). This precipitation model is highly contested, and has been expanded upon with Ryum [51, 52] proposing that hardening actually transpires through multiple reaction sequences:

$$SSSS \rightarrow \eta \qquad \alpha - reaction \qquad (Eq\ 5-2)$$

$$SSSS \rightarrow nuclei \rightarrow \eta' \rightarrow \eta \qquad \beta - reaction \qquad (Eq\ 5-3)$$

$$SSSS \rightarrow GP\ Zone \rightarrow \eta' \rightarrow \eta \qquad \gamma - reaction \qquad (Eq\ 5-4)$$

In Ryum's model, all three precipitation reactions will take place upon aging the SSSS. The traditional model is retained in the γ-reaction, but additional sequences of the SSSS transforming directly to η (α-reaction) along with a tertiary reaction (β) occurring with discrete nuclei providing the precursor to η' formation. Ryum believed that the nucleating agent was some manner of vacancy–solute atom aggregate. This model was further refined by Jiang et al. [53], who proposed the following:

$$SSSS \rightarrow \eta \qquad \alpha - reaction \qquad (Eq\ 5-5)$$

$$SSSS \rightarrow VRC \rightarrow GP\ Zone\ (II) \rightarrow \eta' \rightarrow \eta \qquad \beta - reaction \qquad (Eq\ 5-6)$$

$$SSSS \rightarrow GP\ Zone\ (I) \rightarrow \eta' \rightarrow \eta \qquad \gamma - reaction \qquad (Eq\ 5-7)$$

Jiang believed that the nuclei identified by Ryum within the β-reaction were regions with a high concentration of quenched-in vacancies, and thereby denoted these as vacancy rich clusters (VRC). Such features then purportedly transform into GP-zone (II), which were identified as small regions enriched in vacancies and Zn atoms. It is notable that the GP-zone (I) phase found in the γ-reaction consists of regions high in solute atoms only, which differentiates it from GP-zone (II). Ryum believed that the β-reaction was the dominant sequence in alloys heat-treated to the T6 condition. Hansen et al. [54] concurred with this concept, and noted that peak strength occurred when the β-reaction was able to proceed until η' became the dominant phase present while working with an Al–Zn–Mg–Zr alloy.

Beyond a standard heat-treatment practice of solutionization-quench-artificial aging, the post-sinter processing of aluminum PM products must also include a forming process so as to maintain appropriate dimensional tolerances within the final part. This step (termed "sizing") is typically completed at room temperature utilizing rigid tooling and

press technology comparable to that used during powder compaction. While studies have looked into the mechanisms of sintering-induced distortion [55–57], there exists a clear void in the open literature on the effects of the actual sizing operation itself. Furthermore, the incorporation of post-sinter sizing and heat-treatment processes introduces the unique challenge of whether to apply sizing before, during, or after the heat-treatment cycle. For instance, if the sizing is applied prior to solutionization, any microstructural changes caused by the associated cold work would then be largely annihilated during heat-treatment, and the product may be prone to quench-induced distortion. Similarly, sizing may be implemented in between the quench and artificial aging steps so as to essentially apply a T8 temper. The benefits of a T8 treatment are that cold work is applied when the material is in a soft, malleable state, and that it can eliminate any distortion that may have occurred during quenching.

Although T8 treatments are common in certain aluminum alloys, they are rarely encountered when considering members of the 7xxx series. This largely stems from the dominant precipitation reactions that occur. For example, the θ-precipitation reaction present in the 2xxx series can benefit from cold working prior to artificial aging [58]. A detailed study of the influence of deformation immediately prior to aging on a wrought Al–Zn–Mg alloy [59] has shown that the introduction of dislocations by cold working will change the precipitation reaction upon aging, in some cases resulting in reduced mechanical properties. This is attributed to a reduced likelihood of η’ formation (the main strengthening phase) as a result of direct heterogeneous η formation on dislocations (likely a result of the α-reaction identified by Ryum and Jiang et al.).

Beyond sizing and heat-treatment, shot peening is another post-sinter operation of significant industrial impact, as it is known to increase fatigue performance. Shot

peening is widely utilized across the majority of industries as a means to combat fatigue failure of metals by the introduction of a thin layer of compressive residual stress within the treated surface that helps to resist in-service tensile loads and in turn increase the fatigue performance. Studies have shown varying results for the effectiveness of shot peening to provide fatigue improvements within wrought AA7075. Was [37, 60] conducted two studies considering the effects of shot peening on the fatigue strength of AA7075-T6, with no gains observed for tension–compression fatigue testing while increased fatigue strength was seen for reverse bending fatigue testing. Positive results were found by Benedetti et al. [24] and Wagner et al. [25] for reverse bending testing, while Honda et al. [26] found no improvements in fatigue strength during 3-point bend loading. In work by Harding et al. shot peening of PM7075 was found to impart positive results in rotating–bending fatigue performance, with gains of ~36% instilled through shot peening [29].

Overall, it is clear that post-sinter operations are a necessity within aluminum PM processing, yet detailed knowledge on how they affect the metallurgy of the final products remains largely non-existent within the open literature. Hence, the objective of this study was to initiate fundamental work in this area utilizing a commercially available 7xxx series powder mixture as the base material of interest.

5.4 Materials and Methods

The material of interest in this study was the commercially available aluminum PM system Alumix 431D produced by ECKA Granules (Fürth, Germany). Chemically, the system largely emulates wrought AA7075, but with the addition of a small amount of Sn to aid in sintering. Accordingly, it was denoted as PM7075 throughout this study. A

complete assay for this PM system as measured by ICP-OES (Varian/Agilent Technologies, Santa Clara, CA, USA) is provided in Table 5-1. In addition to the PM system, wrought AA7075 (rolled plate) was also utilized in select instances for comparison purposes. The assay of this material relative to its respective nominal composition is also shown in Table 5-1.

Table 5-1 Measured assays of the raw materials utilized (weight %) relative to the nominal targeted chemistries.

Alloy	Assessment	Al	Cu	Fe	Mg	Si	Sn	Zn
PM7075	Target	Balance	1.6	--	2.5	--	0.2	5.5
	Measured	Balance	1.60	0.08	2.62	0.09	0.14	5.59
AA7075	Target	Balance	1.2-2.0	0.50	2.1-2.9	0.40	--	5.1-6.1
	Measured	Balance	1.55	0.66	2.05	0.14	--	5.44

All PM samples were produced by a standard press-and-sinter approach (i.e., die compaction of raw powder mixture followed by controlled atmosphere liquid phase sintering). Here, an array of test specimen geometries were fabricated, including Charpy bars (75 × 12.7 × 12.7 mm^3) for tensile testing, transverse rupture strength (TRS) bars (31.7 × 12.7 × 12.7 mm^3) for fatigue trials, and discs (30 mm Ø × 5 mm thick) for X-ray diffraction measurements. All samples were compacted in floating rigid die tooling at 400 MPa (pressurization rate of 10 MPa/s) and sintered in a continuous mesh belt furnace (BTU, North Bellerica, USA) under an atmosphere of high purity flowing nitrogen. The nominal thermal cycle consisted of a 20 minute dwell at 400°C for de-lubrication, followed by sintering at 605°C ± 5°C for 20 min and gas quenching to ambient temperature in a water-jacketed section of the furnace. During the sintering process, the atmospheric oxygen content was held at <10 ppm while the dew point was <−60°C.

The sintered compacts then underwent secondary processing, which consisted of various combinations of heat-treatment, sizing, and shot peening. Table 5-2 provides a summary of the specific sequences followed along with the notations utilized throughout this study. In all instances, solutionization was conducted at 470°C for 90 min at temperature followed by quenching into room temperature water. Artificial aging was completed at 125°C for 24 h to attain the T6 temper. Sizing was completed by uni-axially loading lubricated specimens within a closed die tool set. Shot peening was completed using an automated system to an intensity of 0.4 mmN (+5%/−0%) measured using standard N–S Almen strips before and after peening. The peening media was ZrO_2 with a shot diameter of 300 μm.

Table 5-2 Summary of the post-sinter processing sequences considered.

Notation	Processing Sequence
Sol-Age	Solutionize/quench/artificial ageing
Sol-Size-Age	Solutionize/quench/size/artificial ageing
Size-Sol-Age	Size/solutionize/quench/artificial ageing
Size-Sol-Age-Peen	Size/solutionize/quench/artificial ageing/ shot peen

The characterization of the effects of sizing on the material began with measurements of percent reduction in thickness, density, surface roughness, and apparent hardness. The extent of sizing on samples was stated as a % reduction in height, with samples measured directly before and after sizing to 0.001 mm. Densities were measured by a standard Archimedes approach coupled with oil infiltration as per MPIF (Metal Powder Industries Federation) Standard 42 [61]. Surface topography was studied using a Micro-Profiler, model PS50 (Nanovea, Irvine, USA), equipped with a 1.2 mm sensor. Data acquisition was completed using Nanovea 3D software with Nanovea Mountains Pro 3D version 5.0 (Nanovea, Irvine, USA) used for all analyses, including that of surface

roughness. Hardness measurements were completed in the Rockwell B scale (Buehler, Norwood, USA) using a Wilson Rockwell 2000 unit.

The principal means of mechanical testing was fatigue. Here, TRS bars were first set in a 3-point bend fixture. Loading was then applied by a servo-hydraulic frame equipped with a 100 kN load cell. Testing was conducted at a frequency of 25 Hz, an R-ratio of 0.1, and runout taken as 1,000,000 cycles. The staircase method was utilized with fatigue strength and standard deviation calculated based on MPIF Standard 56 [17]. A minimum of 10 tests were completed for each material processing condition of interest. To determine the tensile properties of specimens, Charpy bars were machined into threaded-end round tensile bars per ASTM E8M (American Society for Testing and Materials) [31]. The bars were then tested in an 5594-200HVL (Instron, Norwood, USA) hydraulic frame equipped with a 50 kN load cell. All specimens were loaded at a rate of 5 MPa/s, with strain data collected using an Epsilon model 3542 axial extensometer (Epsilontech, Jackson, USA) that remained attached to the specimen through fracture. As such, the reported values for elongation represent the sum of elastic and plastic strain components.

Microstructural analyses included X-ray diffraction (XRD), differential scanning calorimetry (DSC), and transmission electron microscopy (TEM). XRD was undertaken using a D8 Advance (Bruker, Madison, USA) operated with Co Kα radiation generated at an accelerating voltage of 35 kV and current of 27 mA. For residual stress measurements, the psi-splitting technique was followed with 11 psi-angles from −45° to 45° measured over the {331} aluminum peak. DSC (TA Instruments model SDT Q600, New Castle, USA) was implemented to study precipitation hardening sequences. All such scans were conducted in air with a scanning rate of 5°C/min up to a maximum

temperature of 500°C. In each instance, an equivalent sample of high purity aluminum (99.999 wt% Al) was also scanned. The normalized data from the pure Al trace were subtracted from those acquired from test specimens in an effort to isolate the heat flow effects solely attributable to precipitation-based events. High magnification imaging of precipitates was completed by TEM using a Talos F200X scanning/transmission electron microscope (FEI, Hillsboro, USA) operated with an accelerating voltage of 200 kV. TEM samples were mechanically ground and then electro-polished at 20 V with a solution of 30% HNO_3 in methanol cooled to −30°C. Representative bright field (BF) images and selected area diffraction patterns (SADPs) were recorded in each instance when the beam was closely aligned to the <112> zone axis.

5.5 Results and Discussion

5.5.1 Effects of Sizing on Physical Properties

Sizing is implemented in industry primarily for dimensional control, and it is typically stated as % reduction as defined by the thickness change before and after the sizing operation is completed. While the targeted amount of sizing can vary based on the tolerances required, the extent of sintering-induced distortion, and the geometry of the part in question, values are typically on the order of 3–5%. To identify suitable sizing pressures for PM7075, TRS bars were re-pressed at pressures ranging from 200 to 600 MPa. The Sol-Size-Age and Size-Sol-Age sequences were both evaluated in this manner, as significant differences in formability were anticipated. The effects of sizing pressure on the % reduction in thickness can be seen in Figure 5-1. Both sequences yielded clear and unique trends. The Sol-Size-Age sample showed an immediate rise in % reduction with increased sizing pressure before leveling off at an ~5.7% reduction in thickness for pressures ≥400 MPa. As would be expected, the Size-Sol-Age sample

was more resilient to plastic deformation, with significantly higher pressures required to achieve a particular % reduction. Here, sizing pressures >300 MPa were needed to instill any meaningful level of permanent plastic set. The % reduction then rose gradually with a peak value of 5% realized at the highest pressure that could be safely evaluated (600 MPa). The astute differences in sizing behaviour were a direct consequence of fundamental differences in the yield strength and microstructure of the starting materials. In this sense, Size-Sol-Age samples were processed directly after sintering (T1 temper) whereby the material was in a naturally age-hardened state prior to sizing. The associated microstructure thereby included an abundance of precipitates derived from the η-based solid state reaction sequences [3]. By solutionizing the material immediately before sizing (Sol-Size-Age), the majority of these pre-existing strengthening features would have been eliminated, thereby softening the material and improving formability.

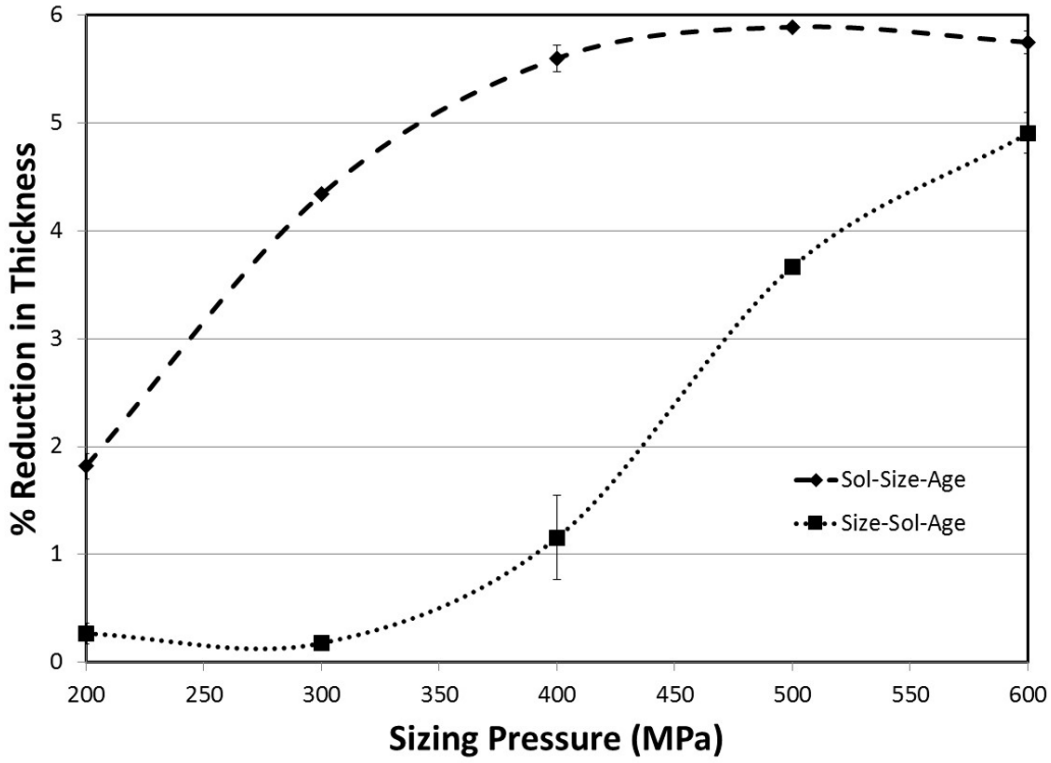

Figure 5-1 Effect of sizing pressure on % reduction in thickness for Sol-Size-Age and Size-Sol-Age processing sequences.

The effect of sizing pressure on the surface roughness of the material was also measured (Figure 5-2). A general decrease in this attribute was noted, with sizing pressure in both sequences resulting in smoother surfaces as compared to those present in the Sol-Age specimens (i.e., unsized). The Sol-Size-Age products offered the lowest surface roughness for all sizing pressures other than 600 MPa, wherein parity with Size-Sol-Age products was observed. The differences here were again ascribed to microstructural differences within the starting materials, with Sol-Size-Age presenting a more formable system.

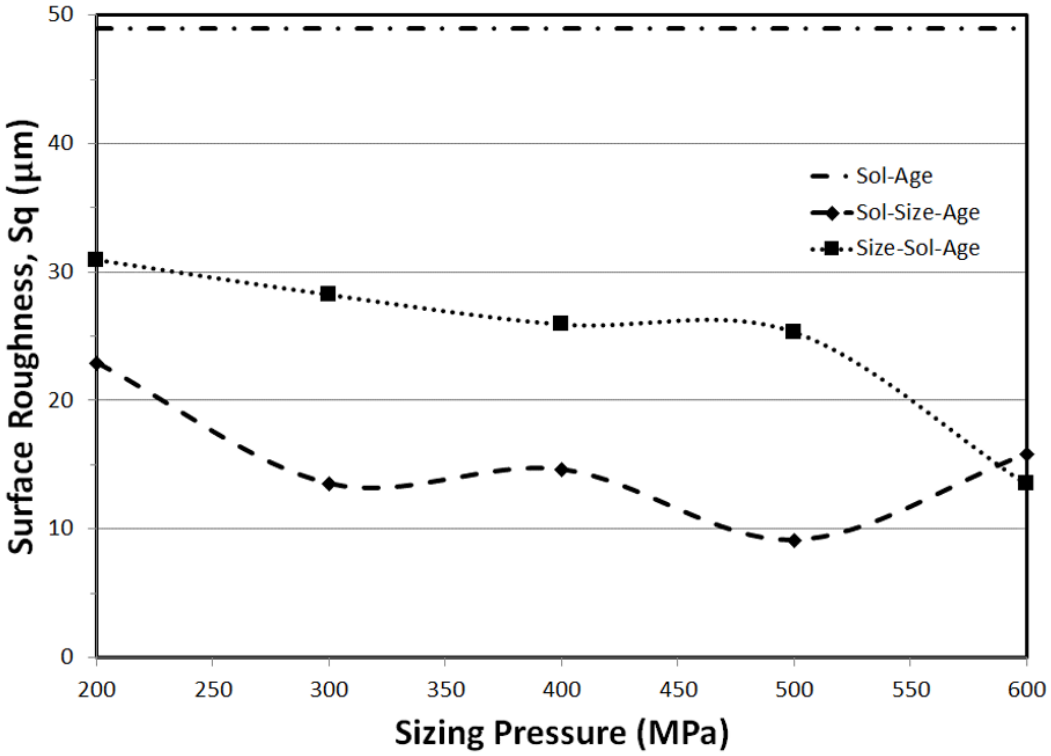

Figure 5-2 Effect of sizing pressure on surface roughness for Sol-Size-Age and Size-Sol-Age processing sequences.

Finally, the densities of numerous specimens in the Sol-Age, Sol-Size-Age, and Size-Sol-Age conditions were measured. Minimal differences were noted, as all values ranged from 2.77 to 2.78 g/cm^3 (representing 99.1%–99.5% theoretical density) irrespective of sizing pressure. This was unsurprising, given that the material was almost fully dense in the sintered state (>99%) and that the deformation from sizing would be highly focused within a thin surface layer of the material. Based on the collective body of physical property data derived for the sized products, it was concluded that the sizing pressures required within the Sol-Size-Age and Size-Sol-Age sequences were 400 and 600 MPa, respectively. Under these conditions, the products from each stream were effectively equivalent in terms of % reduction (≈5%), surface roughness (≈15 µm), and density (≈2.775 g/cm^3).

5.5.2 Effects of Sizing on Mechanical Properties

5.5.2.1 Hardness

In the next stage of research, the effects of sizing on the mechanical properties of the finished products were considered, beginning with apparent hardness (Figure 5-3). In general, the hardness of the Size-Sol-Age specimens was largely unaffected by the extent of sizing, as all values hovered around the nominal measurement for the unsized, Sol-Age counterpart. However, the Sol-Size-Age samples showed a consistently lower hardness than both of these product forms, with the difference becoming more acute at sizing pressures >300 MPa.

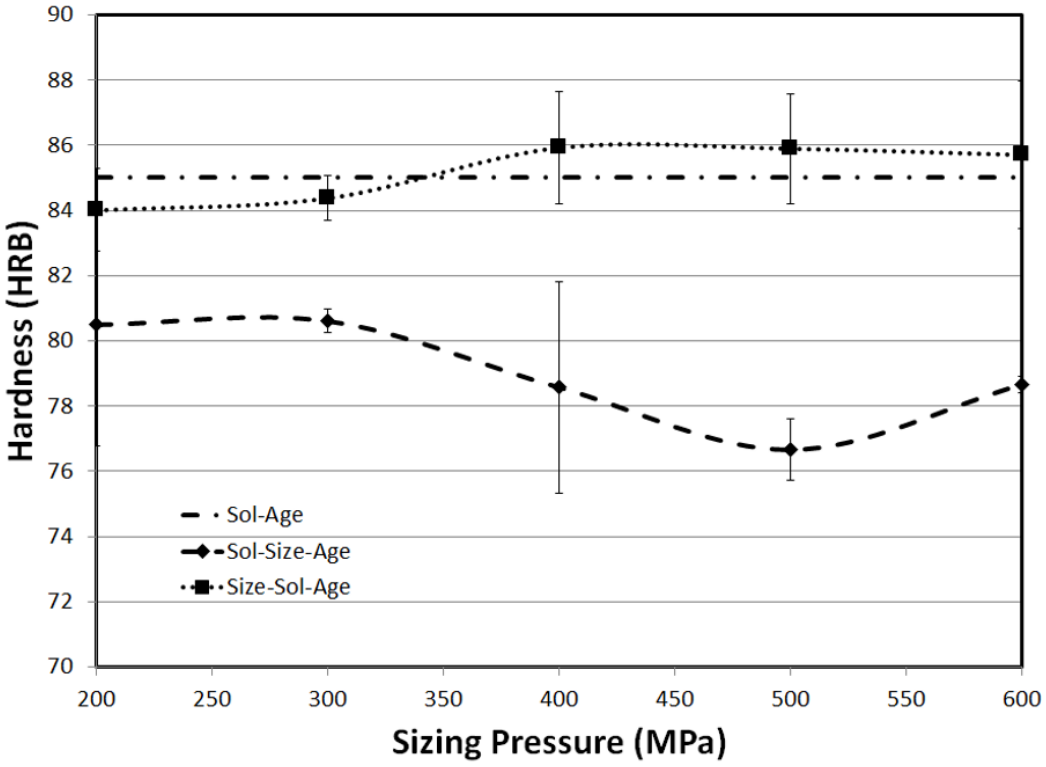

Figure 5-3 Effect of sizing pressure on apparent hardness for Sol-Size-Age and Size-Sol-Age processing sequences.

To determine if changes in the precipitates formed during age hardening may have been responsible for the trends in hardness data, pertinent information was gathered via DSC analyses. Here, samples were processed into the Sol-Size and Size-Sol states and heated in the DSC. In this approach, each specimen was thereby aged in-situ so as to accentuate the thermal events associated with any precipitation hardening mechanism(s) that were operative. The resultant heat flow traces are shown in Figure 5-4, with the principal peaks denoted A to D. With close consideration of the work by Ryum [51, 52], Jiang et al. [53], Ghosh et al. [62] and Berg et al. [63], the precipitation events believed to be associated with these peaks (summarized in Table 5-3) were deduced. The first exothermic peak (A) was attributed to GP-zone (II) formation from vacancy rich clusters (VRC), which consist of regions enriched in vacancies and Zn atoms. It should be noted that GP-zone (I) (i.e., localized regions with heightened concentrations of Zn and Mg atoms) formation occurs at lower temperatures <50°C [53], which is why an exothermic peak corresponding to their formation was not observed in Figure 5-4. The second exothermic peak (B) was due to η' and η formation/growth. Although some studies show discrete peaks associated with the formation of these two phases [34, 53, 64], these could not be distinguished in the present study. The endothermic peak (C) was identified as the dissolution of η' and η, whereas peak (D) was ascribed to the melting of the S or T phase.

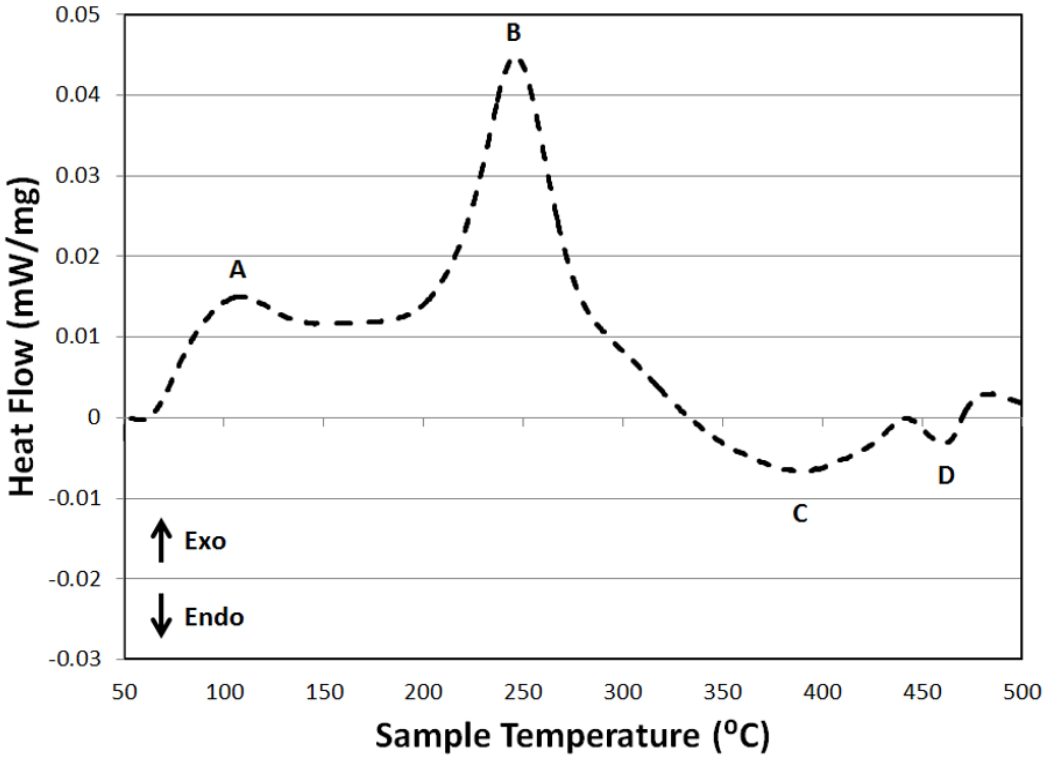

(a)

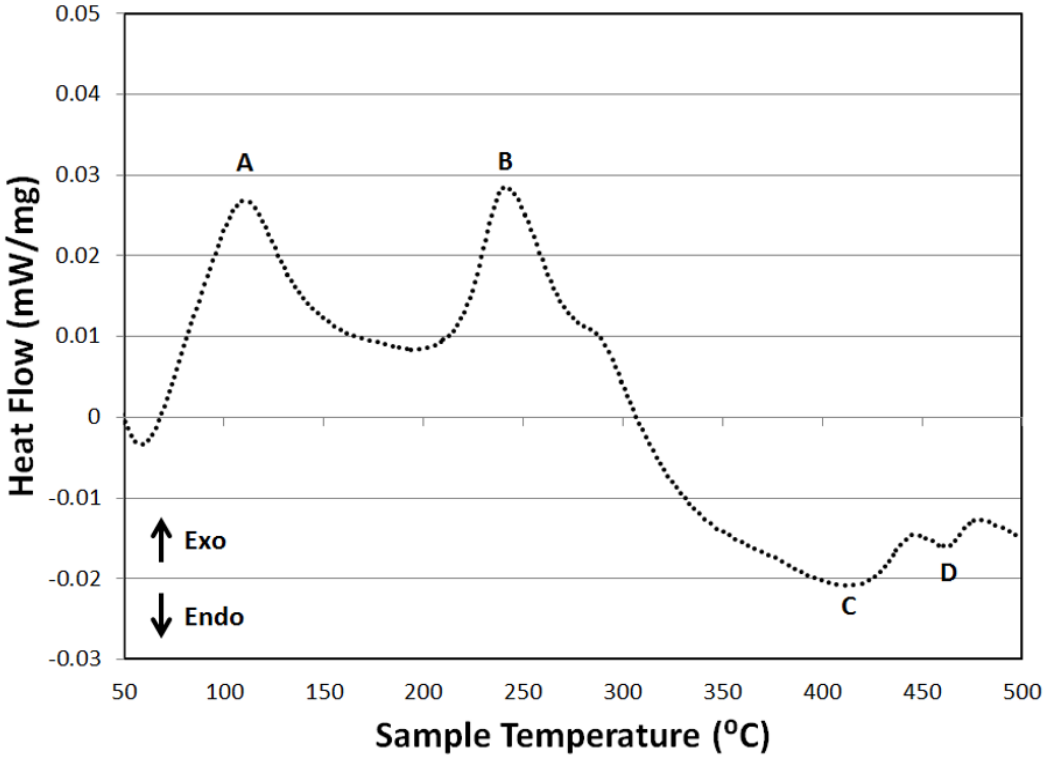

(b)

Figure 5-4 DSC (differential scanning calorimetry) scans recorded from samples of PM7075 (a) immediately after Sol-Size and (b) immediately after Size-Sol processing.

Table 5-3 Summary of the precipitation events observed in Sol-Size and Size-Sol processed specimens.

Peak	Event Description	Temperature (°C)	
		Sol-Size	Size-Sol
A	GP zone (II) formation & growth	108	109
B	η' & η formation	246	241
C	Dissolution of η' & η	388	413
D	Secondary phase melting	460	461

It is common knowledge that the concentration of vacancies within a material scales in a positive and proportionate manner with rising temperature. Hence, water quenching from the solutionization temperature thereby locks in an excess concentration of vacancies within the matrix upon cooling to ambient. Ryum and Jiang's models [51–53] highlight the clear importance of these quenched-in vacancies on the precipitation strengthening of 7xxx series alloys. In particular, they highlight the notion that these vacancies will coalesce to create the VRCs required to activate the β precipitation reaction sequence. However, when sizing is applied to the as-quenched product, the associated deformation would annihilate a portion of the quenched-in vacancies by dislocation movement as a result of plastic deformation. This would then lower the volume fraction of VRCs, and in turn, the propensity for GP-zone (II) formation from the β-reaction. This concept was supported by the DSC results, as peak A within the trace acquired from the Sol-Size specimen (Figure 5-4a) was significantly smaller than that developed from the Size-Sol counterpart (Figure 5-4b). Furthermore, a suppression of the β-reaction sequence would be expected to increase the magnitude of peak B. In this sense, auxiliary solute atoms would now be available for use within the α precipitation sequence such that higher concentrations of η would now be precipitated directly from the SSSS. This concept was also obvious when comparing the Sol-Size and Size-Sol traces (Figure 5-4). Similar DSC results have been reported by Ghosh et al. [62] in a

study looking at applying high pressure torsion to a 7150 alloy between quench and artificial aging, with a comparable, but much more intense decrease in the peak associated with GP-zone (II) formation along with an increase in intensity in the η'/η peak.

Additional samples were then prepared through the complete processing sequences (Sol-Size-Age and Size-Sol-Age) and run in the DSC (Figure 5-5). Similar to the data gathered from unaged specimens, the reactions A'–D' also stem from specific events related to in-situ changes to the underlying precipitates as summarized in Table 5-4. The first endothermic peak (A') was associated to the dissolution of GP-zones. It should be noted that this likely involved the dissolution of both GP-zone (I) and GP-zone (II), as these are indistinguishable events. Next, an exothermic doublet peak (B') was noted. This was attributed to the formation/growth of η' and formation of η. Similar to the Sol-Size and Size-Sol traces (Figure 5-4) the endothermic peak (C') was caused by the dissolution of these precipitates followed by endothermic peak (D') representing the melting of a secondary phase; again, most likely the S or T phase. When comparing the traces shown in Figure 5-5, one striking difference was that endothermic peak A' was substantially smaller in the Sol-Size-Age data. This implied that a lower concentration of GP-zones was present within the starting T6 material, lending further support to the notion that sizing immediately after quench had supressed the formation of a GP-zone (II) through the same mechanism previously discussed. Along with the differences in the A' peak, a clear doublet is present at peak B' in the Size-Sol-Age material, where the Sol-Size-Age material showed a slight shoulder in the peak. Delasi and Adler [34] also saw a similar distinct doublet in AA7075-T651 along with a shoulder in the overaged AA7075-T7351, identifying the first peak as being the formation/growth of η' as well as η formation and the second peak exclusively a result of η growth. This clear doublet in the

Size-Sol-Age material, along with a shoulder in the Sol-Size-Age material, suggests the latter is closer to an overaged condition, with fully developed η present within the microstructure, leading to a reduced likelihood of η growth compared to the Size-Sol-Age material, where fine η formation and growth would take place.

In an effort to substantiate the DSC findings, more direct evidence on the nature of the precipitates was sought by TEM. Representative BF images of samples processed through Sol-Size-Age and Size-Sol-Age are provided in Figure 5-6 along with accompanying <112> SADPs in Figure 5-7. The BF images revealed stark differences between the two samples. The Sol-Size-Age material had precipitates of a high aspect ratio and uniform thickness lying parallel to the {111} planes. These were also quite coarse, with a width in the range of 5–6 nm and length of approximately 11–16 nm. Hence, it was postulated that these represented a plate-like morphology lying on the {111} planes of the aluminum matrix, consistent with the crystallographic orientation of η [51]. In the case of Size-Sol-Age, a much finer, homogenously distributed precipitate structure was observed. Whereas some particles were round (nominal diameter ~2–6 nm), others were thin, rectangular features that lay on {111} planes and had a typical length of 4–6 nm and a uniform thickness (~1 nm). Based on work by Sha and Cerezo [65], η' will exist as plates on the {111} planes within the α-aluminum matrix. Hence, it was postulated that the rectangular precipitates were in fact plates of η' viewed edge-on. Overall, the general appearance of the precipitates within the Size-Sol-Age material was in strong agreement with that found for wrought AA7075-T6 by Guo et al. [66].

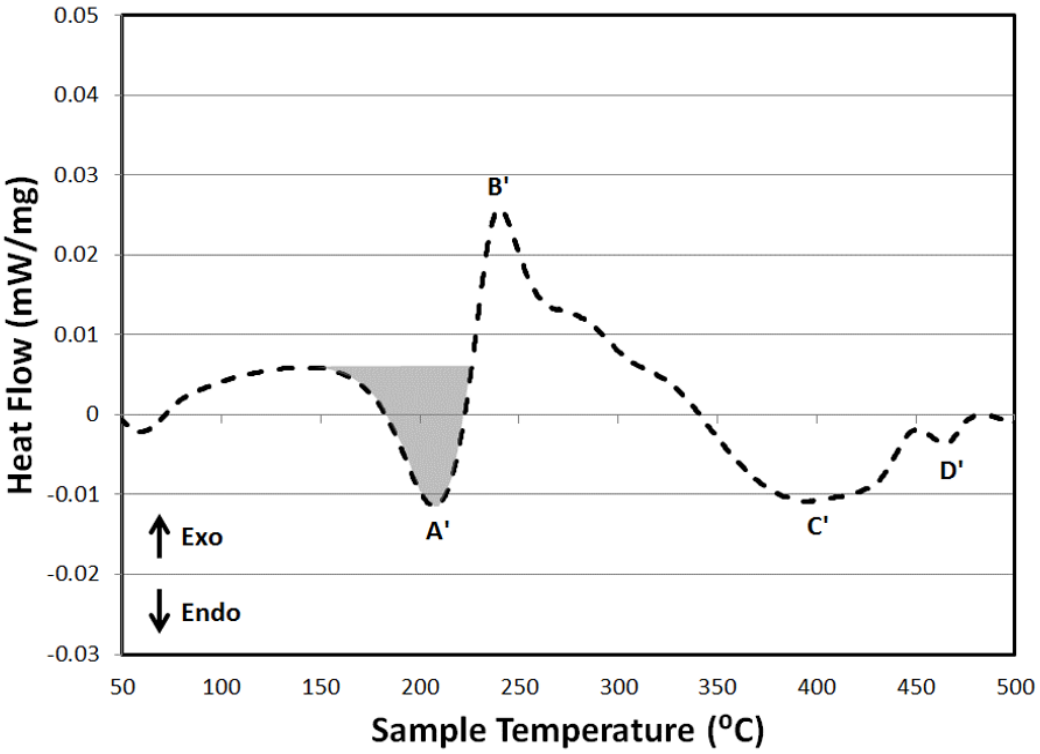

(a)

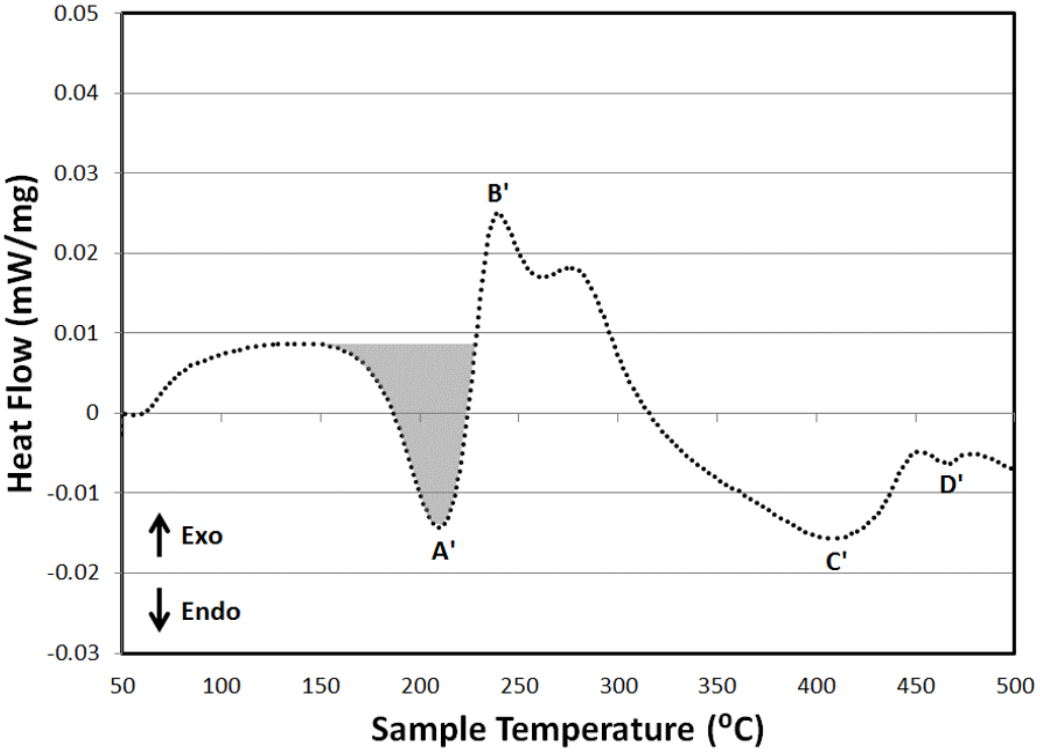

(b)

Figure 5-5 DSC scans recorded from samples of PM7075 after (a) Sol-Size-Age and (b) Size-Sol-Age processing.

Table 5-4 Summary of the precipitation events observed in Sol-Size-Age and Size-Sol-Age processed specimens.

Peak	Event Description	Temperature (°C)	
		Sol-Size-Age	Size-Sol-Age
A'	GP zone dissolution	207	210
B'	η' & η formation	240	239
C'	Dissolution of η' & η	394	407
D'	Secondary phase melting	464	466

Beyond the BF images themselves, the corresponding electron diffraction patterns aligned close to the <112> axis for each sample also showed clear evidence that a secondary phase was present (Figure 5-7). In the case of the Sol-Size-Age material (Figure 5-7a), this came in the form of distinct secondary diffraction points that were thereby attributed to the presence of semi-coherent/incoherent precipitates. The secondary diffraction points lay in rows parallel to the <111> directions (indicated by arrow in Figure 5-7a), such that the resultant pattern was in strong agreement with SADPs devised by Hansen et al for an Al-Zn-Mg alloy containing η' and η phases [54]. In the SADP recorded from the Size-Sol-Age product (Figure 5-7b) discrete secondary diffraction spots were less obvious and relatively intense streaking within the pattern was present (location and direction shown in Figure 5-7b by arrow), indicating that the diffracting phase now maintained an increased level of coherency with the α-aluminum matrix. This implied that fully coherent GP-zones and/or the semi-coherent precipitate η' now dominated the structure.

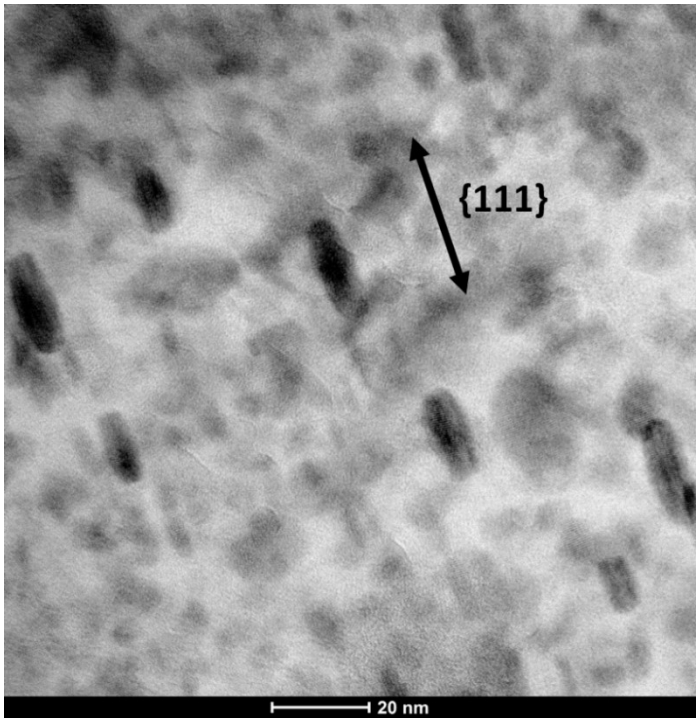

(a)

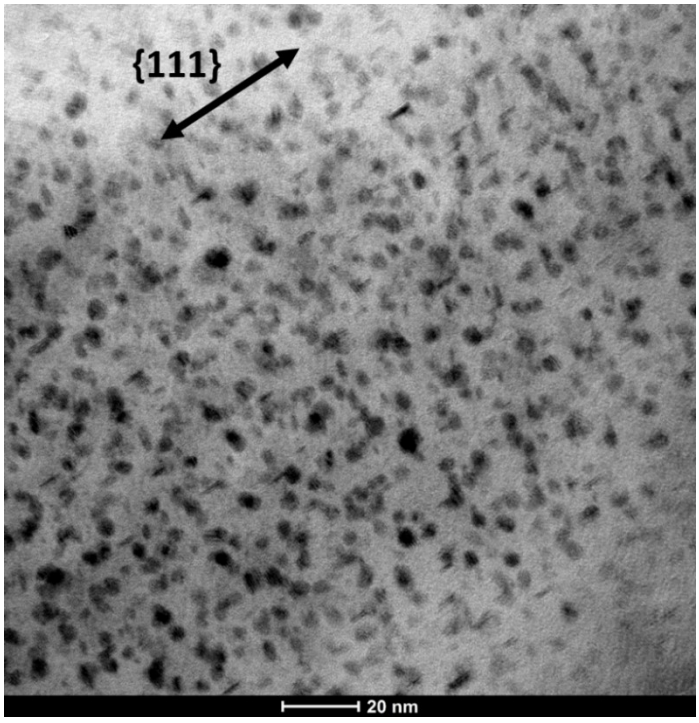

(b)

Figure 5-6 Bright field (BF) TEM images of (a) Sol-Size-Age and (b) Size-Sol-Age processed samples with the beam closely aligned to the <112> zone axis.

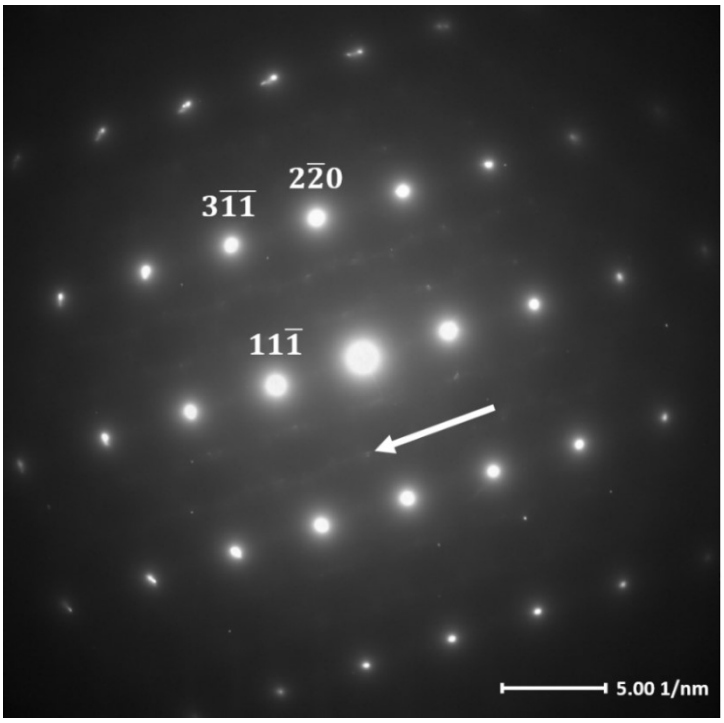

(a)

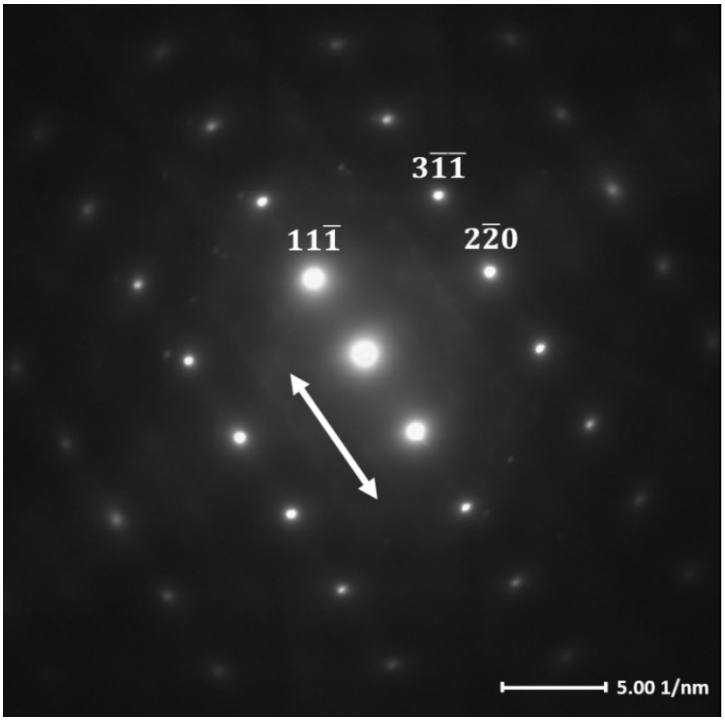

(b)

Figure 5-7 Selected area diffraction patterns (SADPs) recorded from (a) Sol-Size-Age and (b) Size-Sol-Age processed samples with the beam closely aligned to the <112> zone axis.

Based on the combination of TEM and DSC findings, the Size-Sol-Age material appeared to have a microstructure largely comprised of an α-aluminum matrix along with a combination of GP-zone and η' precipitates. This differed from the Sol-Size-Age material, as it was effectively in an overaged state given the increased size of the precipitates and a more acute presence of the fully incoherent η phase within the microstructure. These microstructural differences were in direct agreement with the hardness results (Figure 5-3), as the Sol-Size-Age material was measurably softer.

5.5.2.2 Fatigue Testing

In the next phase of testing, the fatigue performance of PM7075 was evaluated under the different processing streams of interest. A summary of the staircase results is presented in Table 5-5. The highest fatigue durability was noted when sizing was applied before the full heat treatment cycle. Here, sizing was found to invoke a minor gain in fatigue strength (~5%) relative to the specimens processed without any sizing at all (Sol-Age). Prior data indicated that these two materials were comparable in terms of bulk density and hardness (Figure 5-3), presumably eliminating these attributes as influential factors. The one tangible difference was in that of surface roughness (Figure 5-2), whereby an improved value was noted for the Size-Sol-Age products compared to those of Sol-Age. This equated to a smoother exterior surface that would have contained a reduced presence of crack-inducing surface asperities and benefitted fatigue durability. It was also possible that sizing had closed a portion of the near-surface porosity, which has been shown to act as fatigue crack initiation sites within other aluminum PM materials [67]. Overall, it was concluded that the surface condition differential was a key factor of influence.

Table 5-5 Fatigue strength of PM7075 after the application of Sol-Age, Sol-Size-Age, and Size-Sol-Age processing.

Process	σ_a(50%)[1] (MPa)	n[2]	SD[3] (MPa)	vs. Sol-Age
Sol-Age	218	14	5	--
Size-Sol-Age	228	10	4	+5%
Sol-Size-Age	168	10	4	-23%

1 – Fatigue strength; 50% passing as determined through MPIF Standard 56
2 – Number of samples tested
3 – Standard deviation (SD) calculated in accordance with MPIF Standard 56

Interestingly, a large decrease in fatigue behaviour ensued when sizing was implemented as an intermediate step between solutionization/quench and aging. When comparing the metallurgical attributes of the Sol-Size-Age and Size-Sol-Age specimens assessed to this point, the principal difference was a reduced hardness (Figure 5-3) as driven by changes in the strengthening precipitates present (Figure 5-6). As such, a drop in fatigue performance seemed logical. However, given the magnitude of the fatigue decline, it was prudent to complete additional characterization work to determine if auxiliary factors were at play. In particular, it was prudent to determine if sizing-derived microcracks and/or different states of residual stress existed within the materials. Regarding the former, the manner of sizing applied clearly resulted in plastic deformation. Furthermore, it was conceivable that this would be more acute at the surfaces of the bar, as lateral flow would be less constrained here than at regions within the bulk interior. This scenario could thereby facilitate microcracking and a concomitant decline in fatigue performance. To assess this possibility, specimens produced by Sol-Size-Age and Size-Sol-Age were mounted, polished, and examined extensively at high magnifications by SEM. No evidence of microcracking was discovered in any of these specimens, thereby confirming that this was not a contributing factor.

In standard T6 (i.e., Sol-Age) processing, it is well documented that 7xxx series aluminum alloys will have compressive residual stress within the surface of the part instilled by quenching after solution heat-treatment [39, 40]. Such stresses are beneficial to fatigue behaviour, as they act to resist in-service tensile loads. During solution heat-treatment, the large thermal gradients created from water quenching from the solutionization temperature result in the surface of the sample cooling quicker than that of the interior. Once the interior begins to cool, the surface material will resist thermal contraction of the inner material, so that the surface is ultimately in a state of compression while the interior is in tension. The measured surface in-plane residual stresses within the samples processed by Sol-Size-Age and Size-Sol-Age are shown in Figure 5-8. It can be seen that Sol-Size-Age yielded a product with a lower level of compressive surface residual stress. This drop upon sizing after quench was believed to be caused by the plastic deformation acting similar to a stress-relieving process (such as stretching). With regard to Size-Sol-Age processing with the sizing operation performed prior to the heat-treatment, the developed residual stresses within the compact are solely a result of the thermal gradients developed during quenching, and should therefore be similar to the case of a standard T6 treatment.

In the case of Sol-Size-Age processing, it was plausible that the reduction in this advantageous attribute had contributed to the noted decline in fatigue strength in the samples, along with the previously discussed effects of precipitation hardening differences within the system.

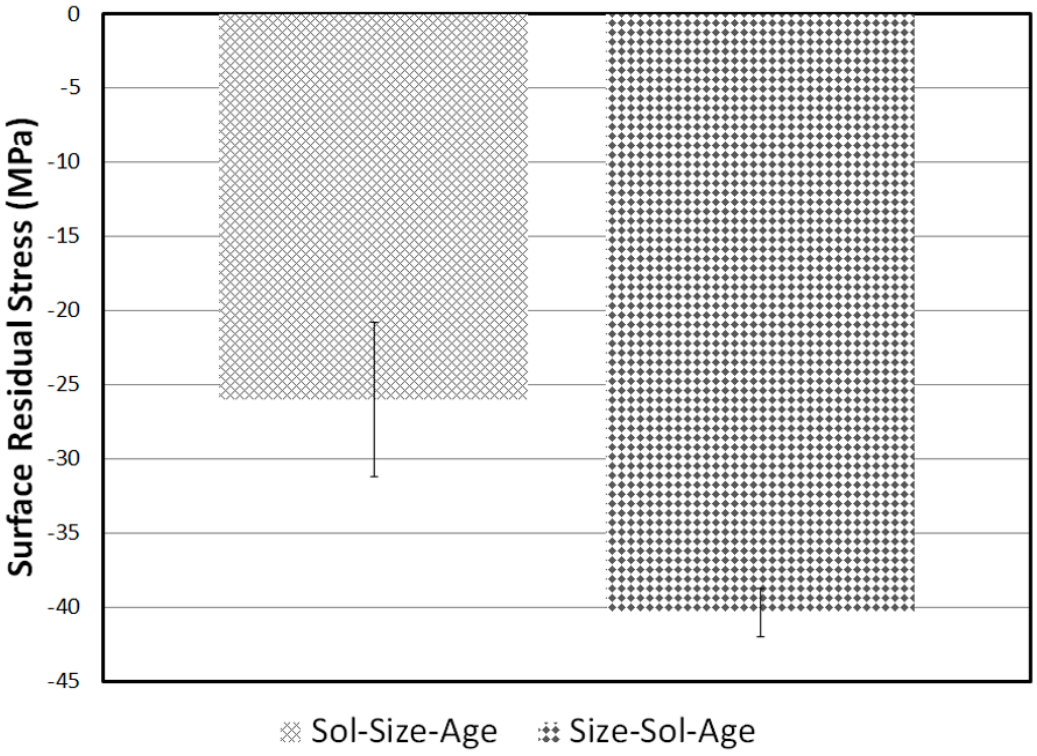

Figure 5-8 Surface residual stress measured in PM7075 as a result of Sol-Size-Age and Size-Sol-Age processing.

To determine if the fatigue differences were unique to PM7075, equivalent processing/testing was completed on the wrought counterpart AA7075. Here, test bars of the material were processed through Sol-Age and Sol-Size-Age sequences, utilizing the same sizing pressure applied during PM7075 Sol-Size-Age processing (400 MPa). The resultant data on fatigue performance are given in Table 5-6. Akin to PM7075, Sol-Size-Age processing again resulted in lower fatigue strength. However, the drop was much less pronounced, which implied that the underlying mechanism was exacerbated in the PM system and/or that additional factors were contributing. As would be expected, the wrought alloy exhibited considerably higher fatigue strengths relative to the data previously acquired for the PM products studied (Table 5-5).

It was postulated that these transitions in fatigue behaviour were underpinned by fundamental differences in microstructure. In this sense, aluminum PM and wrought materials differ in that the former contain higher concentrations of porosity as well as a network of oxides that stems from the starting raw powders. As both attributes are known to serve as preferential sites for crack initiation and thereby lower fatigue resistance, the general inferiority of PM7075 was as expected. However, these same features would also serve as stress concentrators during deformation (i.e., sizing). This would thereby prompt localized increases in the extent of plastic deformation, and concomitantly abnormally high levels of vacancy annihilation within their vicinity. The capacity to form vacancy rich clusters (VRC) would then be heterogeneously reduced, and in turn, so too would the net concentration of the most influential strengthening precipitate, GP-zone (II), as formed through the β-reaction sequence. This scenario would preferentially weaken the alloy near pores and oxides so as to further exacerbate the ease at which fatigue cracks would nucleate and grow. Given that wrought AA7075 is largely devoid of porosity and oxide networks, Sol-Size-Age processing thereby imparted a more prolific fatigue decline in the PM material.

Table 5-6 Fatigue strength of wrought AA7075 processed to Sol-Age and Sol-Size-Age conditions.

Process	**σ_a(50%)[1] (MPa)**	**n[2]**	**SD[3] (MPa)**	**vs. Sol-Age**
Sol-Age	366	12	9	---
Sol-Size-Age	344	10	5	-6%

1 – Fatigue strength; 50% passing as determined through MPIF Standard 56
2 – Number of samples tested
3 – Standard deviation calculated in accordance with MPIF Standard 56

5.5.2.3 Effects of Shot Peening

Beyond sizing and heat-treatment, shot peening is also considered as a secondary operation widely utilized and accepted in industry to combat fatigue-based failure within materials. Given the aforementioned trends in fatigue behaviour, emphasis was restricted to the most advantageous means of processing PM7075: Size-Sol-Age. With shot peening applied to the specimens, an increase in fatigue strength of 29% compared to the unpeened counterpart was found (Table 5-7). These gains in fatigue strength can be attributed to the induced compressive residual stresses caused by inner material resisting the plastic deformation as a result of shot impacting the surface of the sample. The surface in-plane residual stress was measured by XRD (as described in Section 5.4) to be -297 MPa (standard deviation 8 MPa), which has been shown to persist to a depth of approximately 80 μm in samples processed and peened in a similar manner [68]. This ≈30% increase in fatigue strength from shot peening was also in line with similar studies completed through rotating bending fatigue [29] as well as published results for wrought 7075 [16, 24, 37] (showing 20-50% gains).

Table 5-7 Effect of shot peening on the fatigue strength of Size-Sol-Age processed specimens of PM7075.

Process	**σ_a(50%)[1] (MPa)**	**n[2]**	**SD[3] (MPa)**	**vs. Size-Sol-Age**
Size-Sol-Age-Peen	294	10	4	+29%

1 – Fatigue strength; 50% passing as determined through MPIF Standard 56
2 – Number of samples tested
3 – Standard deviation calculated in accordance with MPIF Standard 56

5.5.3 Effects of Thermal Exposure

It is well-understood that thermal exposure is a problematic operating condition for 7xxx aluminum alloys. For instance, when temperatures approach or exceed that utilized for aging (125°C), precipitation and coarsening of the η phase is exacerbated, leading to in-

situ over-aging and a concomitant decline in mechanical properties. Likewise, if the alloy is shot peened, the associated fatigue gains can deteriorate during thermal exposure via a relaxation of the underpinning compressive residual stress. It is for this reason that a maximum operating temperature of 93°C is recommended for shot-peened aluminum alloys [9]. Hence, the effects of thermal exposure at temperatures below (80°C) and above (160°C) these important thresholds were assessed.

Commencing with tensile testing, samples were processed into the Sol-Age condition and exposed. Sizing was not considered in these particular tests, as the machining needed to convert the sized rectangular blank into a round bar would completely remove the sized surface, thereby omitting the development of an accurate correlation to the effects of this process variable. The resultant tensile data are shown in Table 5-8. Exposure at 80°C for 1000 h imparted minimal changes. A higher thermal exposure of 160°C showed a drastic decrease in both yield and ultimate tensile strength coupled with a significant increase in elongation to fracture. Such differences were expected, since the higher temperature should have facilitated excessive over-aging. This was substantiated through XRD analyses (Figure 5-9) as the 80°C sample only exhibited diffraction peaks that matched the α-aluminum matrix phase. No evidence of the incoherent η phase was detected within the system, indicating that the material remained in a peak hardened state. This was as expected given that the exposure temperature was well below the aging temperature applied during Sol-Age processing 125°C. Conversely, the 160°C exposure samples showed distinct diffraction peaks that corresponded to η ($MgZn_2$). As such, the material had most certainly over-aged under these conditions synonymous with the steep decline in tensile properties (Table 5-8).

Table 5-8 Effects of thermal exposure (1000 h at indicated temperature) on the tensile properties of PM7075 initially processed into the Sol-Age condition.

Process	σ_{yield} (MPa)	σ_{UTS} (MPa)	E (GPa)	Elongation (%)
Sol-Age	466 ± 7	496 ± 9	64.7 ± 2.4	1.5 ± 0.2
Sol-Age + 80°C	474 ± 14	480 ± 20	65.1 ± 1.5	1.1 ± 0.5
Sol-Age + 160°C	237 ± 4	323 ± 8	64.5 ± 2.5	4.3 ± 0.6

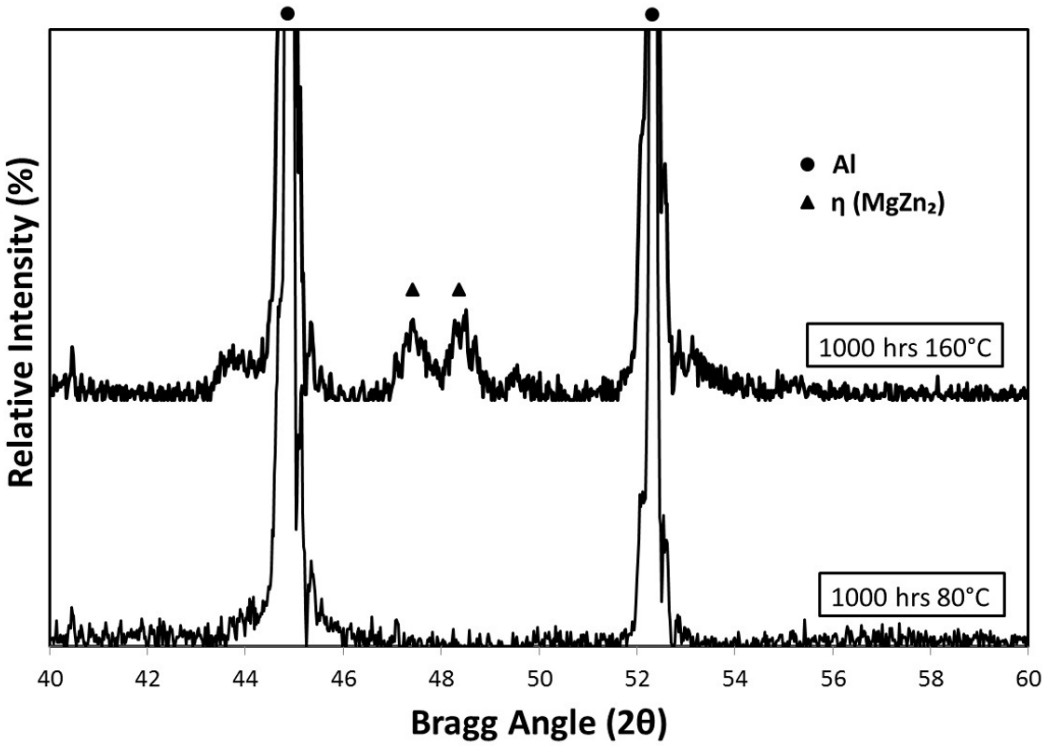

Figure 5-9 XRD traces acquired from Sol-Age samples exposed to 80°C and 160°C for 1000 h.

Data illustrating the effects of thermal exposure on the fatigue of samples originally processed into the Size-Sol-Age state are shown in Table 5-9. Those exposed to 80°C showed no apparent loss in fatigue performance consistent with the trends in tensile data (Table 5-8). Interestingly, this same exposure temperature actually invoked a measurable decrease in fatigue performance for the Size-Sol-Age-Peen specimens, declining from 294 MPa (Table 5-7) to 260 MPa (representing a loss of ≈12% fatigue

strength). As exposure at 80°C progressed, it was determined that a gradual reduction in residual stress also occurred (Figure 5-10). This culminated in a final level of -200 MPa, which represented a loss of ≈30%. Hence, it was presumed that this was the principal factor responsible given that no changes to the underlying precipitate structure were anticipated under these conditions per the data in Table 5-8 and Figure 5-9.

Upon exposure to 160°C, a significant reduction in fatigue strength was seen in the Size-Sol-Age-Peen material, dropping to 173 MPa from 294 MPa (Table 5-7), representing a loss of approximately 41% due to the elevated temperature exposure. This significant drop in fatigue strength is due to a combination of over-aging of the material (supported by tensile and XRD analysis, Table 5-8 and Figure 5-9) along with an essentially full relaxation of the compressive residual stresses imparted by shot peening. As shown in Figure 5-10, we can see that the Size-Sol-Age-Peen material dropped from a starting compressive residual stress value of ≈310 MPa to ≈40 MPa after 1000 h at 160°C with all the peening-induced residual stress wiped out, resulting in a level approximately equal to the residual stress resulting solely from the heat-treatment process (Figure 5-8).

Table 5-9 Fatigue strength of thermally exposed PM7075 Size-Sol-Age and Size-Sol-Age-Peen.

Process	**σ_a(50%)[1] (MPa)**	**n[2]**	**SD[3] (MPa)**	**vs. Size-Sol-Age**
Size-Sol-Age 80ºC	225	10	4	-1%
Size-Sol-Age-Peen 80ºC	260	10	4	+14%
Size-Sol-Age-Peen 160ºC	173	10	4	-24%

1 – Fatigue strength; 50% passing as determined through MPIF Standard 56
2 – Number of samples tested
3 – Standard deviation calculated in accordance with MPIF Standard 56

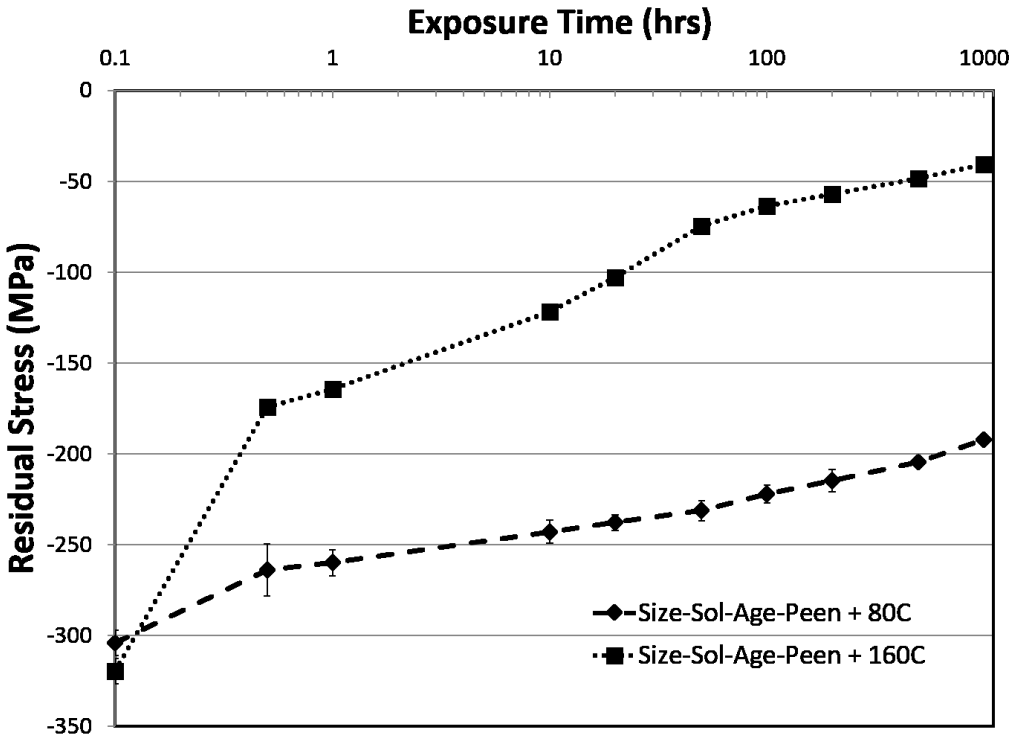

Figure 5-10 Residual stress as a function of elevated temperature exposure for Size-Sol-Age-Peen samples.

5.6 Conclusions

The application of post-sinter sizing, heat-treatment, and shot peening operations to PM7075 was studied in this work. Each process influenced the finished product such that the following conclusions could be drawn:

1) Sizing reduced the surface roughness in all scenarios considered from ≈50 μm to ≈15 μm (Sq) but did not impart a measurable change in the density of the finished products.
2) When test bars were sized in the T1 state and then heat-treated to the T6 condition, the product exhibited a slight gain in fatigue strength (~5%) relative to the standard unsized counterpart. This small gain was principally attributed to the improved surface roughness instilled through sizing.

3) If sizing was applied directly after quenching, the product exhibited declines in apparent hardness (~7 HRB) and fatigue strength (-23%) relative to the unsized counterpart. It was determined that sizing in this manner had catalyzed precipitate growth, leading to larger precipitates and an increased concentration of incoherent η in the product. This processing sequence was also found to have reduced the compressive residual stress from -40 MPa to -25 MPa.
4) Shot peening successfully instilled a relatively large compressive residual stress at the surface of PM7075 (-293 MPa) that improved 3-point bending fatigue by 29%. However, these gains were weakened by thermal exposure at 80°C, and completely eliminated when the temperature was raised to 160°C.

5.7 Acknowledgments

The authors would like to acknowledge the Auto21 Networks of Centres of Excellence and the Natural Sciences and Engineering Research Council of Canada, (NSERC) for financial support via grant C502-CPM and the doctoral post-graduate scholarship program. Bernd Mais (Ecka Granules) is acknowledged for the provision of the Alumix 431D powder employed, along with William Caley, Arjun Kaushal, and Abdul Kahn of the Manitoba Institute for Materials (University of Manitoba, Winnipeg, MB, Canada) for help with the TEM work.

Chapter 6: Fatigue Fracture Assessment

Beyond the quantified drop in fatigue strength observed with Sol-Size-Age processing, fatigue fractures showed qualitative differences when compared to Sol-Age and Size-Sol-Age processed samples. Representative macroscopic fatigue fractures from Sol-Age and Size-Sol-Age processed samples are shown in Figure 6-1. All such samples showed similar macroscopic fatigue fractures, with initiation appearing to begin at the surface, near the centre of the bar (indicated by arrows). Fracture then propagated through the material with fatigue crack growth transpiring in a semi-circular pattern as would be expected (region A), followed by fast fracture (region B). Interestingly, the majority of Sol-Size-Age processed samples show very clear differences in the macroscopic fatigue fracture (Figure 6-2). Here, the initiation location appeared to be shifted off centre towards an outer corner of the bar, and in some cases multiple initiation sites appear to exist (indicated by arrows). The fatigue crack growth (region A) also advanced further through the material before the final fast fracture transpired (region B). It should be noted that since all fatigue testing was completed by the staircase method, these fractures did come from different loads, with the Sol-Age and Size-Sol-Age samples run in the range of 215-235 MPa while the Sol-Size-Age samples were loaded to 165-175 MPa. With the lowered applied load, it was logical that in the Sol-Size-Age samples more extensive fatigue crack growth would occur prior to final fast fracture.

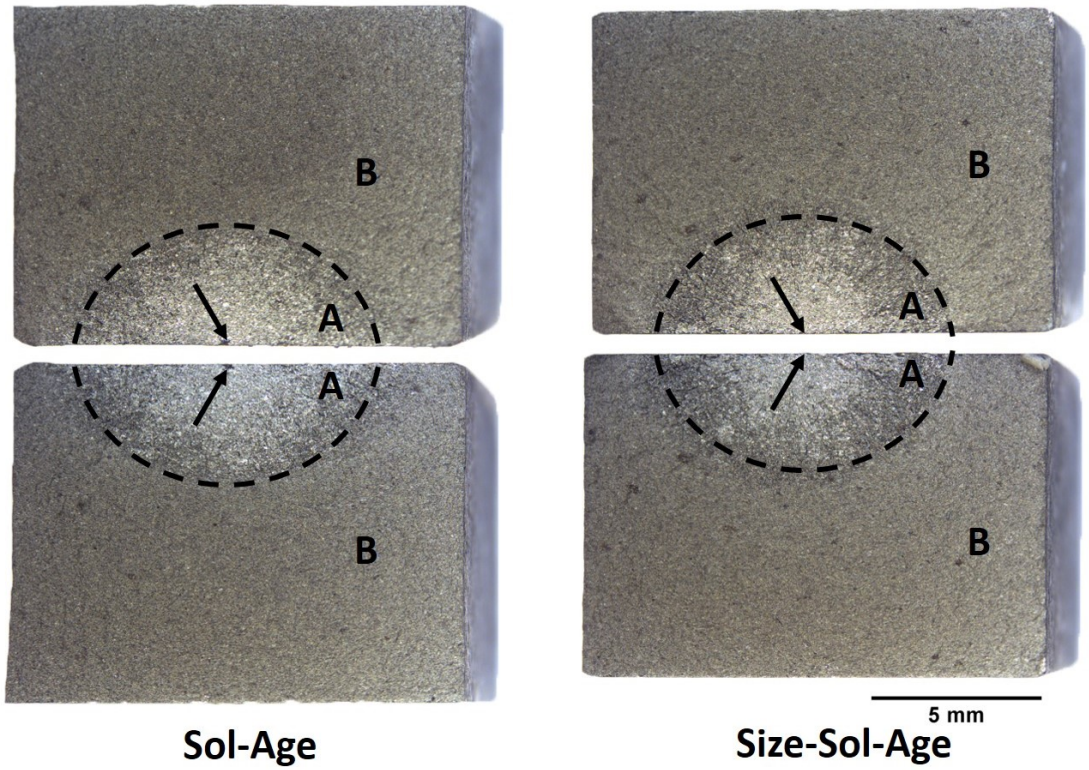

Figure 6-1 Macroscopic fatigue fractures of Sol-Age and Size-Sol-Age samples.

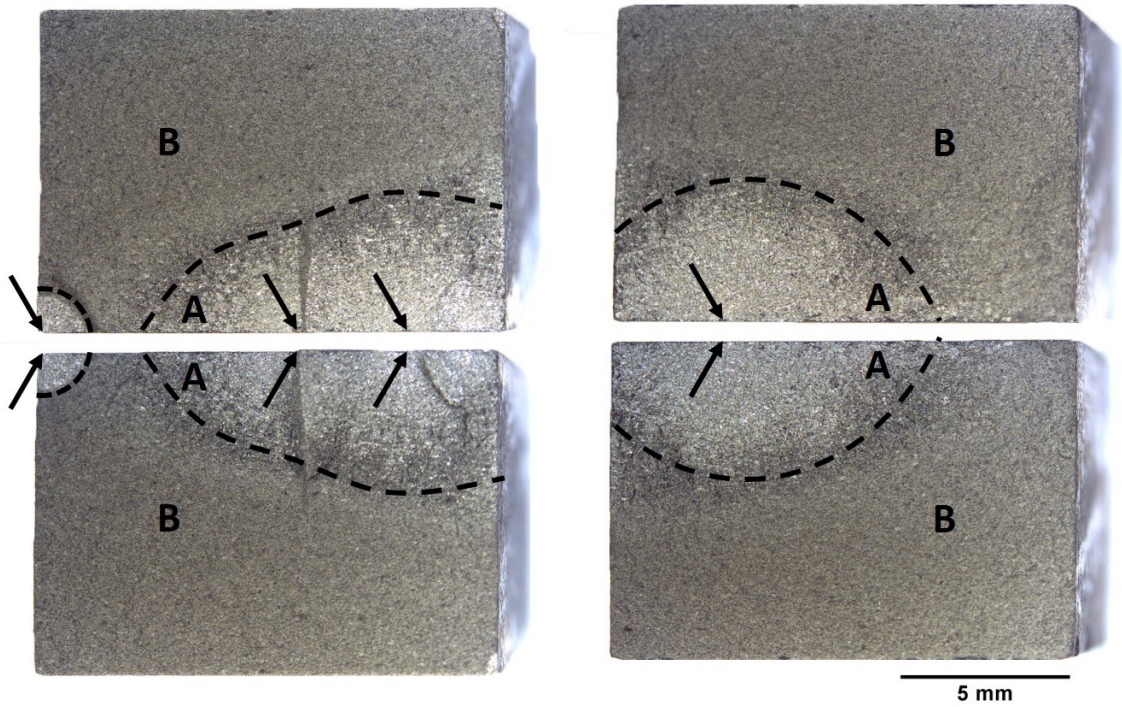

Figure 6-2 Macroscopic fatigue fracture of two Sol-Size-Age samples.

The apparent shift in the point of fatigue crack initiation off centre in the Sol-Size-Age samples is believed to show a high sensitivity within the material with regards to the extent of sizing seen by the bar. PM7075 undergoes densification and shrinkage during sintering, resulting in a sintered bar with elevated edges compared the bulk of the material (i.e. the surface will tend to “cup”). This can been seen visually within the surface profiles recorded from Sol-Age and Sol-Size-Age specimens, shown in Figure 6-3. In the former, it was clear that the bar had elevated edges around the perimeter. Upon sizing, these edges would undergo a higher degree of deformation than the bulk surface resulting in a flattened edge around the perimeter. From a metallurgical perspective, this would have instilled a heterogeneous distribution of newly formed dislocations within the bar immediately after sizing, thereby weakening the material in this localized region in light of a lowered tendency for the formation of GP zone (II) precipitates, as described in Section 5.6.2.1.

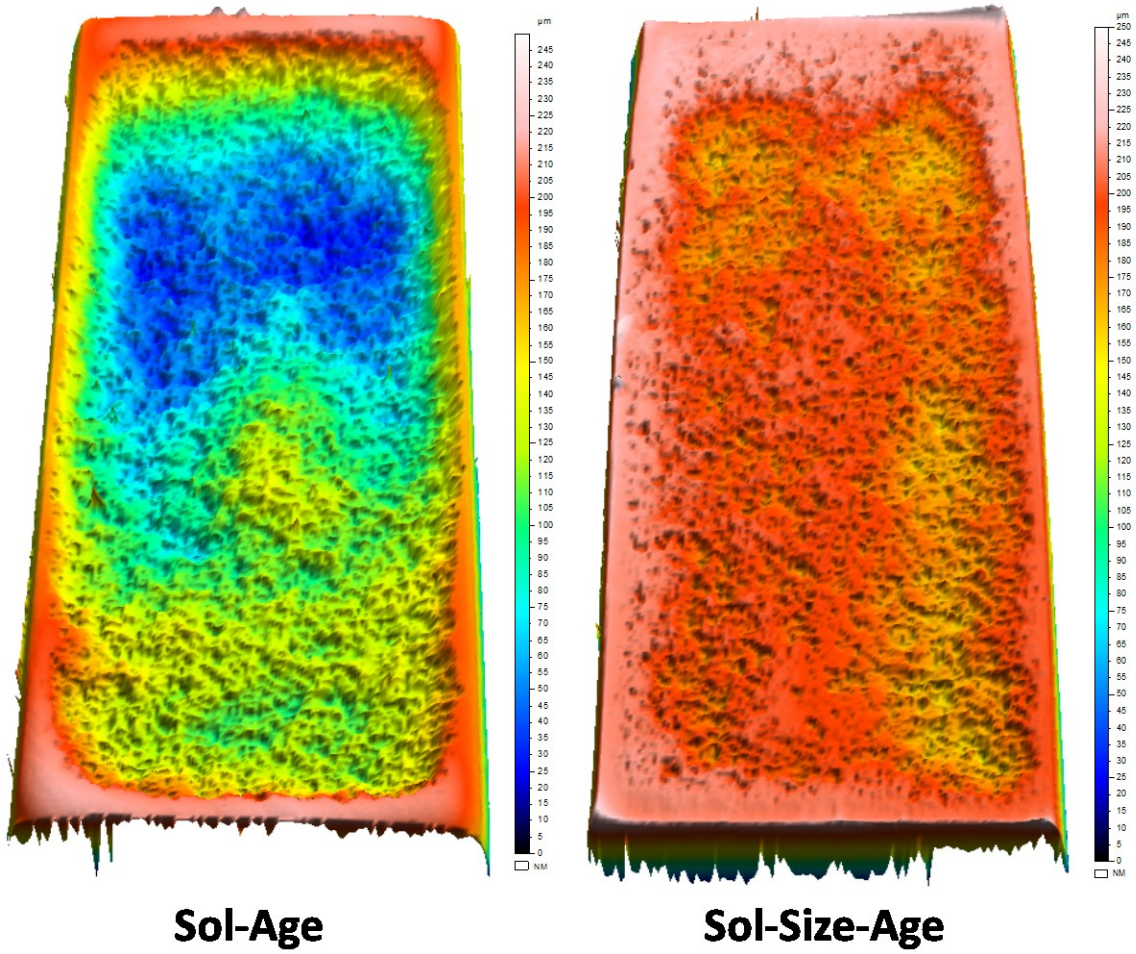

Figure 6-3 Surface profiles of Sol-Age and Sol-Size-Age samples.

It is also conceivable that outer edge flattening promoted an enhanced reduction in the surface compressive residual stresses compared to the bulk of the bar as found and discussed in Section 5.6.2.2. With the weakening of the alloy through reduced precipitation hardening and/or a more prolific reduction in surface compressive residual stresses, fatigue crack initiation would be expected to shift towards the edge. Both of these factors would indicate a high sensitivity of the alloy to the extent of sizing the part undergoes, which could have significant industrial implications if a Sol-Size-Age process was utilized. For instance, when complex parts are sized, varying degrees of deformation would be anticipated throughout the part due to the geometry itself and

sintering-induced deformation. It is believed areas within the part undergoing a higher degree of deformation than the bulk, would be in a weakened state, and prime locations for premature fatigue failure. Although these theories are supported by the data obtained to date, further investigation could shed light on the materials sensitivity to degree of deformation, which will be discussed further in Section 7.1 Suggested Future Work.

Chapter 7: Conclusions and Future Work

This project began primarily as a study to determine the gains attainable by shot peening of PM7075. Although this remained as a primary goal over the course of the work, the scope grew considerably to emphasize a comprehensive understanding of the industrial processing response of the system and the interdependencies of critical secondary operations (sizing and heat treatment).

In order to ensure consistent shot peening intensity from sample to sample, an automated system was required. The setup used a linear actuator and track which was found to produce very consistent peening intensity from run to run, with a tolerance of +5%/-0%, well within the industry standard of +20%/-0%. Three peening intensities were considered, 0.2 mmN, 0.4 mmN and 0.2 mmA. The low intensity peening showed little deformation within the treated surface, while the high intensity peening of 0.2 mmA showed clear damage around the shot impact sites in the form of peened surface extrusion folds (PSEF). Peening of PM7075-T6 to 0.4 mmN showed clear plastic deformation on the treated surface while little to no damage was evident. Peening of cylindrical samples in a linear fashion followed by rotation of the bar by 90° showed consistent surface roughness cylindrically, inferring consistent imparted compressive residual stresses. The orientation of peening was also tracked during rotating bending fatigue (RBF) testing, with failure occurring at various locations around the circumference, providing further evidence that the linear peening of cylindrical samples was consistent around the circumference of the bar. Shot peening to 0.4 mmN of hour-glass specimens in this fashion resulted in an increase in fatigue strength of ~36% over similar unpeened material as measured by RBF testing.

PM7075 slugs were produced industrially (GKN Sinter Metals, Conover NC), in the form of relatively large coupons measuring 100 x 75 x 17 mm. Characterization of the industrially produced specimens revealed a close correlation with laboratory processed counterparts in terms of sinter density, sinter quality, hardness and tensile properties. It was found that Zn had preferentially evaporated from the surface of the parts during sintering, with the loss being most pronounced at the free surface of the puck dropping to 3.1 wt% before stabilizing at a depth of approximately 3 mm to the bulk chemical assay of ≈5.6 wt%. This loss was attributed to the high volatility of Zn, along with the flowing nitrogen atmosphere maintained during sintering. The composition of Zn again decreased towards the belt side of the puck, although the depth and extent of loss was less pronounced compared to the free surface. This was logical in that the free surface would have had no obstruction of the flowing nitrogen, while the belt would interfere with flow and in turn, lessen evaporative Zn loss. The localized depletion of Zn was believed to weaken the surface of the sintered part due to an acute dependence on the precipitation of Mg/Zn-based phases as the principal strengthening features. This was quantified by a reduced Rockwell hardness on the surface on the puck along with sub-surface transitions in nanoindentation hardness. The nano-hardness was found to drop to ≈1.65 GPa before stabilizing at a depth of approximately 2 mm to ≈2.50 GPa.

Shot peening was found to induce strain hardening within the treated surface, increasing the surface nano-hardness in line with the bulk material to a value of ≈2.50 GPa. Through XRD measurement, the surface in-plane residual stress was found to increase from ≈-60 MPa in the T6 treated material to ≈-230 MPa upon shot peening to 0.4 mmN. Depth profiling of the induced compressive residual stresses from shot peening was measured by ND. Strain measurements were made in the 3 assumed principal

directions over the {311} diffraction peak for aluminum at CNBC. The strain measurements, coupled with a theoretical model predicting the elastic response of the material in the {311} crystallographic orientation allowed the in-plane residual stress to be calculated as a function of depth, finding the compressive layer transitioning to tensile stresses at a depth of 60-100 μm.

Sizing was incorporated into the study as the process is required in industry to meet final part dimensional tolerances. Two processing routes that incorporated sizing were considered: (a) sizing in the T1 state, followed by solution heat treatment (Size-Sol-Age) and (b) sizing in the quenched state prior to artificial aging of the alloy (Sol-Size-Age); essentially a T8 treatment. These two processing routes were compared to a standard T6 treatment (Sol-Age) devoid of sizing. Sizing in either the T1 or quenched state resulted in a reduction of surface roughness over Sol-Age processing (decreasing from ≈50 to ≈15 μm, Sq) while no changes in the density of the parts was found (all showed densities >99% theoretical). It was found that sizing in the quenched state (Sol-Size-Age) resulted in consistently reduced hardness over Sol-Age and Size-Sol-Age. This reduction was attributed an alteration of precipitation hardening by the annihilation of quenched in vacancies via dislocation generation/movement instilled through sizing. DSC analyses showed that Sol-Size-Age processed specimens had a reduced likelihood of GP zone (II) formation (with a higher prevalence of η'/η precipitation) during artificial aging compared to Size-Sol-Age counterparts. With GP zone (II) formation being the preferred strengthening mechanism for the alloy, the lowered concentration in Sol-Size-Age processing could explain the reduced hardness compared to Sol-Age and Size-Sol-Age processing. This was also supported by TEM and SADP's showing coarser precipitates to exist within the Sol-Size-Age material compared to that processed via Size-Sol-Age.

In keeping with the industrial focus of the work, fatigue testing was switched to 3-point bending fatigue in order to test press-and-sintered parts directly, avoiding the requirement of machining for RBF. It was found that Size-Sol-Age processing resulted in a slight increase (≈5%, 228 MPa) in the 3-point bend fatigue strength of the alloy compared to Sol-Age processing (218 MPa). This minor gain was believed to be attributed to the reduced roughness of the bar as a result of sizing. Similar to hardness, the fatigue strength of Sol-Size-Age was found to decrease compared to Sol-Age and Size-Sol-Age processed samples, although the decrease of 23% (to 168 MPa) was somewhat surprising. In addition to the observed changes in precipitation hardening, it was also discovered that the in-plane surface compressive residual stresses induced by quenching were reduced during Sol-Size-Age processing (≈25 MPa vs. ≈40 MPa in the Size-Sol-Age samples), which may also have attributed to the reduction in fatigue strength as surface compressive residual stresses will be beneficial in 3-point bend fatigue loading.

Shot peening was found to impart a high level of compressive residual stress within the surface of Size-Sol-Age processed bars (≈297 MPa), increasing the fatigue strength to 294 MPa (+29%). As residual stress relaxation will occur at elevated temperatures, the compressive residual stress and fatigue strength of shot peened Size-Sol-Age bars was assessed after exposure to 80 and 160°C for 1 000 hrs. Upon exposure to the lower temperature, the compressive residual stresses was reduced to ≈200 MPa, a loss of ≈30%, along with a drop of approximately 12% in fatigue strength (260 MPa). This drop in fatigue strength was believed to be solely due to reduced compressive residual stress in the surface, as tensile testing showed no changes in the static strength of the material at exposure to 80°C. After exposure to 160°C for 1 000 hrs, the compressive residual

stress was effectively eliminated (reduced to -40 MPa), while a significant drop in fatigue strength, from 294 MPa to 173 MPa (loss of ≈41%), was found. This reduction was due not only to the full relaxation of surface compressive residual stress, but also overaging of the alloy as supported by tensile testing and XRD analyses.

Finally, based on macroscopic fatigue fractures of Sol-Age, Size-Sol-Age, and Sol-Size-Age samples, it was believed that the material may be highly sensitive to extent of deformation when sizing is completed in the as-quenched state. By shifting of the fatigue crack initiation site from the centre of the bars in Sol-Age and Size-Sol-Age samples towards the edge in Sol-Size-Age samples, it is theorized that the highly-deformed edge is being either further weakened by increased dislocation movement compared to the bulk, and/or the surface residual stresses are being altered due to higher deformation locally. This could have significant consequences if Sol-Size-Age processing was implemented industrially, as complex parts would likely undergo spatially varying levels of deformation, creating weakened areas within the part.

7.1 Suggested Future Work

As with many studies, as this project progressed many additional questions were developed. Although many of these were investigated, due to time constraints and available equipment others remained unanswered. The paragraphs below outline some aspects of the project that the author believes to be worthy of future study.

Although early in the work various peening intensities were considered, the method of selecting the chosen intensity of 0.4 mmN was not exhaustive and additional gains may be realized by further tailoring the intensity for the alloy. One interesting possibility

which came up was the use of a higher intensity peening which would result in a high degree of plastic deformation (and in turn likely damage to the surface) followed by a lighter intensity peening in an attempt to smooth the surface after the high level of plastic deformation during high intensity peening. Studies applying this concept to wrought aluminum showed minimal benefit, although considerably deeper compressive layers were seen. This may indicate that the high intensity peening resulted in a high degree of damage that persisted after the light peening. The interesting aspect of this type of approach with PM in mind is the possibility of increasing the density in the near surface layer and closing surface and near-surface pores, of which are prime locations for fatigue crack initiation. Additionally, with increased fatigue performance in mind other peening methods may present increased gains, most notably laser peening. The largest issue seen is the cost and availability of laser peening compared to the wide spread availability and use of standard shot peening.

The preferential Zn loss from the surface during sintering presents a very unique challenge during PM processing of 7xxx series aluminum alloys. PM is likely the only processing route where this free surface during sintering would result in this scenario. As 7xxx series aluminum alloys rely on the precipitation hardening from Zn and Mg alloying additions the loss of Zn should reduce the strength of the material near surface, supported by the reduced hardness seen. The reduced strength, especially in this critical area where fatigue failure will begin in bend loading, could be reducing the performance of the material. This may be combated by sintering in a Zn rich atmosphere or by creating a barrier to reduce the likelihood of Zn evaporation, although this type of approach may not be economically feasible in an industrial setting.

The effect of sizing is believed to be the most interesting result during this study and although the root cause was explored, many interesting questions remain. The effects of varying the amount of sizing on the fatigue strength is recommended. Also, it was speculated that Sol-Size-Age processing of PM7075 showed a greater decrease in fatigue strength than wrought AA7075 because of acute vacancy annihilation around pores and the inherent oxide network within the PM system. This could be verified if TEM imaging could be completed around a pore and/or the oxide network in the material. It may also be interesting to see directly through TEM the extent of precipitate coarsening with varying levels of sizing.

The prospect of sizing in the quenched state is likely to be more attractive in an industrial setting as the loads required to instill the desired permanent set in the part would be lower. Also, by sizing in the quenched state any distortion within a part during quenching could be rectified. Whether these benefits out way the significant drop in fatigue strength would be up to the designer, although completing a thermomechanical treatment of solutionization-quench-initial age-sizing-final age could provide a good balance in turns of performance and industrial processing. If an initial age was completed prior to sizing, the precipitation reaction could be started, which may reduce the likelihood of vacancy annihilation and in turn possibly result in increased hardening over Sol-Size-Age processing.

With regards to the fatigue fractures, the speculation of the fatigue crack initiation site being shifted due to higher deformation along the edge resulting in either a weakened state and/or changes to the residual stress state could be verified by TEM analysis to compare the precipitate structure in the centre vs the edge of the bar, along with residual stress profiling of the surface. It would also be very interesting to look at more complex

geometries to see if varying local deformations produce an inhomogeneous structure. The fatigue fractures were imaged at higher magnification (not presented here, by SEM) with no clear differences regarding crack initiation or growth, although fractography is a complex field. If the fractures were viewed by someone with more knowledge of the subject, notable differences in how the fatigue cracks initiate and grow with various processing routes may be distinguishable.

REFERENCES

[1] I. Polmear, *Light Alloys: From Traditional Alloys to Nanocrystals*, Forth Edit. Oxford, UK: Elsevier Ltd., 2006.

[2] DuckerWorldwide, “2015 North American Light Vehicle Aluminum Content Study: Executive Summary,” Troy, MI, 2014.

[3] A. D. P. LaDelpha, H. Neubing, and D. P. Bishop, “Metallurgical assessment of an emerging Al–Zn–Mg–Cu P/M alloy,” *Mater. Sci. Eng. A*, vol. 520, no. 1–2, pp. 105–113, Sep. 2009.

[4] J. E. Hatch, Ed., *Aluminum: Properties and Physical Metallurgy*. Metals Park, OH: American Society for Metals, 1990.

[5] M. P. Groover, *Fundamentals of Modern Manufacturing: Materials, Processes, and Systems*, Third Edit. John Wiley & Sons Inc., 2006.

[6] R. M. German, *Powder Metallurgy Science*, Second Edi. Princeton, NJ: Metal Powder Industries Federation, 1994.

[7] R. M. German, *Sintering Theory and Practice*. New York, NY: John Wiley & Sons Inc., 1996.

[8] ASTM, “Standard Specification for Sintered Aluminum Structural Parts,” *ASTM Vol 02.05*, 2005.

[9] SAE, “SAE Manual on Shot Peening HS-84.” Society of Automotive Engineers, Inc, Warrendale, Pa, 2001.

[10] B. D. Cullity, *Elements of X-Ray Diffraction*, Second Edi. Addison-Wesley Publishing Company Inc., 1978.

[11] DuckerWorldwide, “2009 Update on Aluminum Content in North American Light Vehicles: Phase I,” Troy, MI, 2008.

[12] I. a. MacAskill, a. D. P. LaDepha, J. H. Milligan, J. J. Fulton, and D. P. Bishop, “Effects of cold and hot densification on the mechanical properties of a 7XXX series powder metallurgy alloy,” *Powder Metall.*, vol. 52, no. 4, pp. 304–310, Dec. 2009.

[13] ASM, *ASM Handbook Vol 7: Powder Metal Technologies and Applications*. ASM International, 1998.

[14] E. Ilia, R. A. Chernenkoff, and K. T. Tutton, “Improvement in Fatigue Performance of Powder-Forged Connecting Rods by Shot Peening,” *Int. J. Powder Metall.*, vol. 45, no. 3, pp. 55–61, 2009.

[15] R. A. Chernenkoff, “The Effects of Surface Modification on the Fatigue Performance of Powder-Forged Steel,” in *Advances in Powder Metallurgy and Particulate Materials*, 2001, pp. 1194–1204.

[16] ASM, “ASM Handbook - Vol 5 Surface Engineering, Desktop Edition.” ASM International, pp. 278–302, 1994.

[17] MPIF, “Determination of Rotating Beam Fatigue Endurance Limit of Powder Metallurgy (PM) Materials.” MPIF Standard 56, 2011.

[18] SAE, “Aerospace Material Specification ASM-S-13165.” SAE International, 1997.

[19] ASTM, “Standard Specification for Automated Controlled Shot Peening of Metallic Articles Prior to Nickel , Autocatalytic Nickel , or Chromium Plating , or as Final Finish,” vol. 02.05. ASTM International, pp. 1–9, 2004.

[20] J. Solis-Romero, “A Note on the Detrimental Effects of Peened Aluminum Alloys,” *Met. Finish. News*, vol. 10, no. July, 2009.

[21] J. M. Martín and F. Castro, “Liquid phase sintering of P/M aluminium alloys: effect of processing conditions,” *J. Mater. Process. Technol.*, vol. 143–144, pp. 814–821, Dec. 2003.

[22] M. Azadbeh and Z. Razzaghi, “Properties evolution during transient liquid phase sintering of PM Alumix 431,” *Adv. Mater. Sci. …*, vol. 2009, pp. 1–5, 2010.

[23] T. Pieczonka, J. Kazior, A. Szexczyk-Nykiel, M. Hebda, and M. Nykiel, “Effect of atmosphere on sintering of Alumix 431D powder,” *Powder Metall.*, vol. 55, no. 5, pp. 354–360, 2012.

[24] M. Benedetti, V. Fontanari, P. Scardi, C. L. A. Ricardo, and M. Bandini, “Reverse bending fatigue of shot peened 7075-T651 aluminium alloy: The role of residual stress relaxation,” *Int. J. Fatigue*, vol. 31, no. 8–9, pp. 1225–1236, 2009.

[25] L. Wagner, M. Mhaede, M. Wollmann, I. Altenberger, and Y. Sano, “Surface layer properties and fatigue behavior in Al 7075-T73 and Ti-6Al-4V Comparing results after laser peening, Shot peening and ball-burnishing,” *Int. J. Struct. Integr.*, vol. 2, no. 2, pp. 185–199, 2011.

[26] T. Honda, M. Ramulu, and A. S. Kobayshi, “Shot Peening and Fatigue Crack Growth in 7075-T7351 Aluminum,” in *Key Engineering Materials*, 2005, vol. 297–300, pp. 72–77.

[27] S. Grendahl, D. Snoha, and B. Hardisky, “Shot-Peening Sensitivity of Aerospace Materials,” 2007.

[28] K. Oguri, “Fatigue life enhancement of aluminum alloy for aircraft by Fine Particle Shot Peening (FPSP),” *J. Mater. Process. Technol.*, vol. 211, no. 8, pp. 1395–1399, Aug. 2011.

[29] M. D. Harding, D. P. Bishop, and I. W. Donaldson, “Effects of Shot Peening on Aluminum Powder Metallurgy Alloys,” in *Advances in Powder Metallurgy and Particulate Materials*, 2010, pp. 629–640.

[30] SAE, “SAE Standard J442.” SAE International, 1995.

[31] ASTM, “Standard Test Method for Tension Testing of Metallic Materials [Metric].” ASTM E 8M - 07, 2007.

[32] L. Clapham, S. White, and R. Rogge, “Neutron diffraction investigation of fluid end cracking in well stimulation pump fluid ends,” *Int. J. Press. Vessel. Pip.*, vol. 83, no. 2, pp. 118–122, 2006.

[33] E. A. Brandes, *Smithells Metals Reference Book*, 6th ed. Butterworth & Co Ltd, 1983.

[34] R. DeIasi and P. Adler, “Calorimetric Studies of 7000 Aluminum Alloys: I. Matrix Precipitate Characterization of 7075,” *Metall. Trans. A*, vol. 8A, pp. 1177–1183, 1977.

[35] I. C. Noyan and J. B. Cohen, *Residual Stress: Measurement by Diffraction and Interpretation*. Springer, 1987.

[36] A. Molinari, E. Santuliana, I. Cristofolini, A. Rao, S. Libardi, and P. Marconi, “Surface modifications induced by shot peening and their effect on the plane bending fatigue strength of a Cr – Mo steel produced by powder metallurgy,” *Mater. Sci. Eng. A*, vol. 528, pp. 2904–2911, 2011.

[37] G. S. Was and R. M. Pelloux, “The Effect of Shot Peening on the Fatigue Behavior of Alloy 7075-T6,” *Metall. Trans. A*, vol. 10, no. 5, pp. 656–658, 1979.

[38] C. Rodopoulos, “Optimisation of the fatigue resistance of 2024-T351 aluminium alloys by controlled shot peening—methodology, results and analysis,” *Int. J. Fatigue*, vol. 26, no. 8, pp. 849–856, Aug. 2004.

[39] J. S. Robinson, D. A. Tanner, C. E. Truman, A. M. Paradowska, and R. C. Wimpory, “The influence of quench sensitivity on residual stresses in the aluminium alloys 7010 and 7075,” *Mater. Charact.*, vol. 65, pp. 73–85, Mar. 2012.

[40] J. S. Robinson, D. A. Tanner, S. van Petegem, and A. Evans, “Influence of quenching and aging on residual stress in Al-Zn-Mg-Cu alloy 7449,” *Mater. Sci. Technol.*, vol. 28, no. 4, pp. 420–30, 2012.

[41] R. Becker, M. E. Karabin, J. C. Liu, and R. E. Smelser, “Distortion and residual stress in quenched aluminum bars,” *J. Appl. Mech.*, vol. 63, no. 3, pp. 699–705, 1996.

[42] C. E. Murray, “Equivalence of Kröner and weighted Voigt-Reuss models for x-ray stress determination,” *J. Appl. Phys.*, vol. 113, p. 153509, 2013.

[43] R. E. Logé, H. S. Turkmen, M. P. Miller, R. Rogge, and P. R. Dawson, “Modelling the distribution of lattice strains following plastic deformation of a polycrystal. Application to aluminum AA 7075 T6,” in *Materials Science Forum*, 2002, pp. 69–76.

[44] ASM, *ASM Handbook Vol 2: Properties and Selection: Nonferrous Alloys and Special-Purpose Materials*. ASM International, 1990.

[45] P. S. Prevey, “A method of determining the elastic properties of alloys in selected crystallographic directions for x-ray diffraction residual stress measurement,” in *Advances in X-Ray Analysis*, 1977, pp. 345–354.

[46] C. D. Boland, R. L. Hexemer Jr, I. W. Donaldson, and D. P. Bishop, “Development of an aluminum PM alloy for ‘press-sinter-size’ technology,” *Int. J. Powder Metall.*, vol. 47, no. 1, pp. 39–48, 2011.

[47] R. W. Cooke, R. L. Hexemer, I. W. Donaldson, and D. P. Bishop, “Press-and-sinter processing of a PM counterpart to wrought aluminum 2618,” *J. Mater. Process. Technol.*, vol. 230, pp. 72–79, 2016.

[48] D. W. Heard, I. W. Donaldson, and D. P. Bishop, “Metallurgical assessment of a hypereutectic aluminum-silicon P/M alloy,” *J. Mater. Process. Technol.*, vol. 209, no. 18–19, pp. 5902–5911, 2009.

[49] G. B. Schaffer and S. H. Huo, “On development of sintered 7xxx series aluminum alloys,” *Powder Metall.*, vol. 42, pp. 219–226, 1999.

[50] L. F. Mondolfo, N. A. Gjostein, and D. W. Levinson, “Structural Changes During the Aging in An Al-Mg-Zn Alloy,” *J. Met.*, vol. 206, pp. 1378–1385, 1956.

[51] N. Ryum, “Precipitation Kinetics in an Al-Zn-Mg-Alloy,” *Z Met.*, vol. 66, no. 6, pp. 338–343, 1975.

[52] N. Ryum, “Further Investigation on the Precipitation Kinetics in an Al-Zn-Mg-Alloy,” *Z Met.*, vol. 66, no. 6, pp. 344–346, 1975.

[53] X. J. Jiang, B. Noble, B. Holme, G. Waterloo, and J. Tafto, “Differential Scanning Calorimetry and Electron Diffraction Investigation on Low-Temperature Aging in Al-Zn-Mg Alloys,” *Metall. Mater. Trans. A*, vol. 31, no. 2, pp. 339–348, 2000.

[54] V. Hansen, K. Stiller, G. Waterloo, J. Gjonnes, and X. Z. Li, “Structure and Transformations During Artificial Aging of an Industrial 7xxx-Series Al-Zn-Mg-Zr Alloy,” *Mater. Sci. Forum*, vol. 396–402, no. 2, pp. 815–820, 2002.

[55] J. Liu and R. M. German, “Densification and Shape Distortion in Liquid-Phase Sintering,” *Metall. Mater. Trans. A*, vol. 30, pp. 3211–3217, 1999.

[56] X. N. Yuan, S. H. Huo, G. B. Schaffer, and M. Qian, “Distortion in a 7xxx Aluminum Alloy during Liquid Phase Sintering,” *Metall. Mater. Trans. A Phys. Metall. Mater. Sci.*, vol. 45, no. 2, pp. 1010–1018, 2014.

[57] R. W. Cooke, D. P. Bishop, R. L. Hexemer Jr, and I. W. Donaldson, “Effects of Zirconium Additions on the Sintering Response of an Aluminum—Copper—Magnesium Alloy,” *Int. J. Powder Metall.*, vol. 49, no. 1, pp. 37–46, 2013.

[58] J. M. Papazian, “A Calorimetric Study of Precipitation in Aluminum Alloy 2219,” *Metall. Trans. A*, vol. 12, no. 2, pp. 269–280, 1981.

[59] A. Deschamps, F. Livet, and Y. Bréchet, “Influence of Predeformation on Ageing in an Al–Zn–Mg alloy—I. Microstructure Evolution and Mechanical Properties,” *Acta Mater.*, vol. 47, no. 1, pp. 281–292, 1999.

[60] G. S. Was, R. M. Pelloux, and M. C. Frabolot, “Effect of Shot Peening Methods on the Fatigue of Alloy 7075-T6,” in *Proceddings of 1st International Conferance on Shot Peening*, 1982, pp. 445–451.

[61] MPIF, “Determination of Density of Compacted or Sintered Powder Metallurgy (PM) Products.” MPIF Standard 42, 2008.

[62] K. S. Gosh, N. Gao, and M. J. Starink, “Characterization of high pressure torsion processed 7150 Al-Zn-Mg-Cu alloy,” *Mater. Sci. Eng. A*, vol. 552, pp. 164–171, 2012.

[63] L. K. Berg *et al.*, “GP-zones in Al-Zn-Mg alloys and their role in artificial aging,” *Acta Mater.*, vol. 49, no. 17, pp. 3443–3451, 2001.

[64] D. Wang, D. R. Ni, and Z. Y. Ma, “Effect of pre-strain and two-step aging on microstructure and stress corrosion cracking of 7050 alloy,” *Mater. Sci. Eng. A*, vol. 494, pp. 360–366, 2008.

[65] G. Sha and A. Cerezo, “Early-stage precipitation in Al-Zn-Mg-Cu alloy (7050),” *Acta Mater.*, vol. 52, no. 15, pp. 4503–4516, 2004.

[66] W. Guo *et al.*, “Evolution of precipitate microstructure during stress aging of an Al-Zn-Mg-Cu alloy,” *Mater. Sci. Eng. A*, vol. 634, pp. 167–175, 2015.

[67] G. N. Grayson, G. B. Schaffer, and J. R. Griffiths, “Fatigue crack propagation in a sintered 2xxx series aluminium alloy,” *Mater. Sci. Eng. A*, vol. 434, no. 1–2, pp. 1–6, 2006.

[68] M. D. Harding, I. W. Donaldson, R. L. Hexemer, M. A. Gharghouri, and D. P. Bishop, “Characterization of the microstructure, mechanical properties, and shot peening response of an industrially processed Al-Zn-Mg-Cu PM alloy,” *J. Mater. Process. Technol.*, vol. 221, pp. 31–39, 2015.

Appendix A: Copyright Release

MPIF Release (Chapter 3)

April 25, 2017

PowderMet2010 Conference Proceedings
Metal Powder Industries Federation
105 College Road East
Princeton, NJ 08540-6692

I am preparing my PhD thesis for submission to the Faculty of Graduate Studies at Dalhousie University, Halifax, Nova Scotia, Canada. I am seeking your permission to include a manuscript version of the following paper(s) as a chapter in the thesis:

"Effects of Shot Peening on Aluminum Powder Metallurgy Alloys", M.D. Harding, I.W. Donaldson, D.P. Bishop, Advances in Powder Metallurgy & Particulate Materials—2010, compiled by M. Bulger and B. Stebick, Metal Powder Industries Federation, Princeton, NJ, 2010, vol. 1, part 6, pp. 29–40.

Canadian graduate thesis are reproduced by the Library and Archives of Canada (formerly National Library of Canada) through a non-exclusive, world-wide license to reproduce, loan, distribute, or sell theses. I am also seeking your permission for the material described above to be reproduced and distributed by the LAC(NLC). Further details about the LAC(NLC) thesis program are available on the LAC(NLC) website (www.nlc-bnc.ca).

Full publication details and a copy of this permission letter will be included in the thesis.

Yours sincerely,

Matthew Harding

Permission is granted for:

a) the inclusion of the material described above in your thesis.

b) for the material described above to be included in the copy of your thesis that is sent to the Library and Archives of Canada (formerly National Library of Canada) for reproduction and distribution.

Name: Turner Abbott Title: Manger, Office Services

Signature: [redacted] Date: April 25, 2017

ELSEVIER RELEASE (CHAPTER 4)

ELSEVIER LICENSE
TERMS AND CONDITIONS

Apr 25, 2017

This Agreement between Matthew Harding ("You") and Elsevier ("Elsevier") consists of your license details and the terms and conditions provided by Elsevier and Copyright Clearance Center.

License Number	4095950655629
License date	Apr 25, 2017
Licensed Content Publisher	Elsevier
Licensed Content Publication	Journal of Materials Processing Technology
Licensed Content Title	Characterization of the microstructure, mechanical properties, and shot peening response of an industrially processed Al–Zn–Mg–Cu PM alloy
Licensed Content Author	M.D. Harding,I.W. Donaldson,R.L. Hexemer,M.A. Gharghouri,D.P. Bishop
Licensed Content Date	July 2015
Licensed Content Volume	221
Licensed Content Issue	n/a
Licensed Content Pages	9
Start Page	31
End Page	39
Type of Use	reuse in a thesis/dissertation
Portion	full article
Format	both print and electronic
Are you the author of this Elsevier article?	Yes
Will you be translating?	No
Order reference number	
Title of your thesis/dissertation	Industrial Processing of an Al-Zn-Mg-Cu Powder Metallurgy Alloy
Expected completion date	Aug 2017
Estimated size (number of pages)	200
Elsevier VAT number	GB 494 6272 12

Requestor Location	Matthew Harding 1360 Barrington St Department of Mechanical Engineering Rm C360 Halifax, NS B3H 4R2 Canada Attn: Matthew Harding
Total	0.00 CAD

Terms and Conditions

INTRODUCTION

1. The publisher for this copyrighted material is Elsevier. By clicking "accept" in connection with completing this licensing transaction, you agree that the following terms and conditions apply to this transaction (along with the Billing and Payment terms and conditions established by Copyright Clearance Center, Inc. ("CCC"), at the time that you opened your Rightslink account and that are available at any time at http://myaccount.copyright.com).

GENERAL TERMS

2. Elsevier hereby grants you permission to reproduce the aforementioned material subject to the terms and conditions indicated.
3. Acknowledgement: If any part of the material to be used (for example, figures) has appeared in our publication with credit or acknowledgement to another source, permission must also be sought from that source. If such permission is not obtained then that material may not be included in your publication/copies. Suitable acknowledgement to the source must be made, either as a footnote or in a reference list at the end of your publication, as follows:
"Reprinted from Publication title, Vol /edition number, Author(s), Title of article / title of chapter, Pages No., Copyright (Year), with permission from Elsevier [OR APPLICABLE SOCIETY COPYRIGHT OWNER]." Also Lancet special credit - "Reprinted from The Lancet, Vol. number, Author(s), Title of article, Pages No., Copyright (Year), with permission from Elsevier."
4. Reproduction of this material is confined to the purpose and/or media for which permission is hereby given.
5. Altering/Modifying Material: Not Permitted. However figures and illustrations may be altered/adapted minimally to serve your work. Any other abbreviations, additions, deletions and/or any other alterations shall be made only with prior written authorization of Elsevier Ltd. (Please contact Elsevier at permissions@elsevier.com). No modifications can be made to any Lancet figures/tables and they must be reproduced in full.
6. If the permission fee for the requested use of our material is waived in this instance, please be advised that your future requests for Elsevier materials may attract a fee.
7. Reservation of Rights: Publisher reserves all rights not specifically granted in the combination of (i) the license details provided by you and accepted in the course of this licensing transaction, (ii) these terms and conditions and (iii) CCC's Billing and Payment terms and conditions.
8. License Contingent Upon Payment: While you may exercise the rights licensed immediately upon issuance of the license at the end of the licensing process for the transaction, provided that you have disclosed complete and accurate details of your proposed use, no license is finally effective unless and until full payment is received from you (either by publisher or by CCC) as provided in CCC's Billing and Payment terms and conditions. If full payment is not received on a timely basis, then any license preliminarily granted shall be deemed automatically revoked and shall be void as if never granted. Further, in the event that you breach any of these terms and conditions or any of CCC's Billing and Payment terms and conditions, the license is automatically revoked and shall be void as if never granted. Use of materials as described in a revoked license, as well as any use of the materials beyond the scope of an unrevoked license, may constitute copyright infringement and publisher reserves the right to take any and all action to protect its copyright in the materials.

9. Warranties: Publisher makes no representations or warranties with respect to the licensed material.
10. Indemnity: You hereby indemnify and agree to hold harmless publisher and CCC, and their respective officers, directors, employees and agents, from and against any and all claims arising out of your use of the licensed material other than as specifically authorized pursuant to this license.
11. No Transfer of License: This license is personal to you and may not be sublicensed, assigned, or transferred by you to any other person without publisher's written permission.
12. No Amendment Except in Writing: This license may not be amended except in a writing signed by both parties (or, in the case of publisher, by CCC on publisher's behalf).
13. Objection to Contrary Terms: Publisher hereby objects to any terms contained in any purchase order, acknowledgment, check endorsement or other writing prepared by you, which terms are inconsistent with these terms and conditions or CCC's Billing and Payment terms and conditions. These terms and conditions, together with CCC's Billing and Payment terms and conditions (which are incorporated herein), comprise the entire agreement between you and publisher (and CCC) concerning this licensing transaction. In the event of any conflict between your obligations established by these terms and conditions and those established by CCC's Billing and Payment terms and conditions, these terms and conditions shall control.
14. Revocation: Elsevier or Copyright Clearance Center may deny the permissions described in this License at their sole discretion, for any reason or no reason, with a full refund payable to you. Notice of such denial will be made using the contact information provided by you. Failure to receive such notice will not alter or invalidate the denial. In no event will Elsevier or Copyright Clearance Center be responsible or liable for any costs, expenses or damage incurred by you as a result of a denial of your permission request, other than a refund of the amount(s) paid by you to Elsevier and/or Copyright Clearance Center for denied permissions.

LIMITED LICENSE

The following terms and conditions apply only to specific license types:
15. **Translation**: This permission is granted for non-exclusive world **English** rights only unless your license was granted for translation rights. If you licensed translation rights you may only translate this content into the languages you requested. A professional translator must perform all translations and reproduce the content word for word preserving the integrity of the article.
16. **Posting licensed content on any Website**: The following terms and conditions apply as follows: Licensing material from an Elsevier journal: All content posted to the web site must maintain the copyright information line on the bottom of each image; A hyper-text must be included to the Homepage of the journal from which you are licensing at http://www.sciencedirect.com/science/journal/xxxxx or the Elsevier homepage for books at http://www.elsevier.com; Central Storage: This license does not include permission for a scanned version of the material to be stored in a central repository such as that provided by Heron/XanEdu.
Licensing material from an Elsevier book: A hyper-text link must be included to the Elsevier homepage at http://www.elsevier.com . All content posted to the web site must maintain the copyright information line on the bottom of each image.

Posting licensed content on Electronic reserve: In addition to the above the following clauses are applicable: The web site must be password-protected and made available only to bona fide students registered on a relevant course. This permission is granted for 1 year only. You may obtain a new license for future website posting.
17. **For journal authors:** the following clauses are applicable in addition to the above:

Preprints:
A preprint is an author's own write-up of research results and analysis, it has not been peer-reviewed, nor has it had any other value added to it by a publisher (such as formatting, copyright, technical enhancement etc.).
Authors can share their preprints anywhere at any time. Preprints should not be added to or enhanced in any way in order to appear more like, or to substitute for, the final versions of articles however authors can update their preprints on arXiv or RePEc with their Accepted Author Manuscript (see below).
If accepted for publication, we encourage authors to link from the preprint to their formal publication via its DOI. Millions of researchers have access to the formal publications on ScienceDirect, and so links will help users to find, access, cite and use the best available version. Please note that Cell Press, The Lancet and some society-owned have different preprint policies. Information on these policies is available on the journal homepage.
Accepted Author Manuscripts: An accepted author manuscript is the manuscript of an article that has been accepted for publication and which typically includes author-incorporated changes suggested during submission, peer review and editor-author communications.
Authors can share their accepted author manuscript:

- immediately
    - via their non-commercial person homepage or blog
    - by updating a preprint in arXiv or RePEc with the accepted manuscript
    - via their research institute or institutional repository for internal institutional uses or as part of an invitation-only research collaboration work-group
    - directly by providing copies to their students or to research collaborators for their personal use
    - for private scholarly sharing as part of an invitation-only work group on commercial sites with which Elsevier has an agreement
- After the embargo period
    - via non-commercial hosting platforms such as their institutional repository
    - via commercial sites with which Elsevier has an agreement

In all cases accepted manuscripts should:

- link to the formal publication via its DOI
- bear a CC-BY-NC-ND license - this is easy to do
- if aggregated with other manuscripts, for example in a repository or other site, be shared in alignment with our hosting policy not be added to or enhanced in any way to appear more like, or to substitute for, the published journal article.

Published journal article (JPA): A published journal article (PJA) is the definitive final record of published research that appears or will appear in the journal and embodies all value-adding publishing activities including peer review co-ordination, copy-editing, formatting, (if relevant) pagination and online enrichment.
Policies for sharing publishing journal articles differ for subscription and gold open access articles:
Subscription Articles: If you are an author, please share a link to your article rather than the full-text. Millions of researchers have access to the formal publications on ScienceDirect, and so links will help your users to find, access, cite, and use the best available version.
Theses and dissertations which contain embedded PJAs as part of the formal submission can be posted publicly by the awarding institution with DOI links back to the formal publications on ScienceDirect.

If you are affiliated with a library that subscribes to ScienceDirect you have additional private sharing rights for others' research accessed under that agreement. This includes use for classroom teaching and internal training at the institution (including use in course packs and courseware programs), and inclusion of the article for grant funding purposes.
Gold Open Access Articles: May be shared according to the author-selected end-user license and should contain a CrossMark logo, the end user license, and a DOI link to the formal publication on ScienceDirect.
Please refer to Elsevier's posting policy for further information.
18. **For book authors** the following clauses are applicable in addition to the above: Authors are permitted to place a brief summary of their work online only. You are not allowed to download and post the published electronic version of your chapter, nor may you scan the printed edition to create an electronic version. **Posting to a repository:** Authors are permitted to post a summary of their chapter only in their institution's repository.
19. **Thesis/Dissertation**: If your license is for use in a thesis/dissertation your thesis may be submitted to your institution in either print or electronic form. Should your thesis be published commercially, please reapply for permission. These requirements include permission for the Library and Archives of Canada to supply single copies, on demand, of the complete thesis and include permission for Proquest/UMI to supply single copies, on demand, of the complete thesis. Should your thesis be published commercially, please reapply for permission. Theses and dissertations which contain embedded PJAs as part of the formal submission can be posted publicly by the awarding institution with DOI links back to the formal publications on ScienceDirect.

Elsevier Open Access Terms and Conditions
You can publish open access with Elsevier in hundreds of open access journals or in nearly 2000 established subscription journals that support open access publishing. Permitted third party re-use of these open access articles is defined by the author's choice of Creative Commons user license. See our open access license policy for more information.
Terms & Conditions applicable to all Open Access articles published with Elsevier:
Any reuse of the article must not represent the author as endorsing the adaptation of the article nor should the article be modified in such a way as to damage the author's honour or reputation. If any changes have been made, such changes must be clearly indicated.
The author(s) must be appropriately credited and we ask that you include the end user license and a DOI link to the formal publication on ScienceDirect.
If any part of the material to be used (for example, figures) has appeared in our publication with credit or acknowledgement to another source it is the responsibility of the user to ensure their reuse complies with the terms and conditions determined by the rights holder.
Additional Terms & Conditions applicable to each Creative Commons user license:
CC BY: The CC-BY license allows users to copy, to create extracts, abstracts and new works from the Article, to alter and revise the Article and to make commercial use of the Article (including reuse and/or resale of the Article by commercial entities), provided the user gives appropriate credit (with a link to the formal publication through the relevant DOI), provides a link to the license, indicates if changes were made and the licensor is not represented as endorsing the use made of the work. The full details of the license are available at http://creativecommons.org/licenses/by/4.0.
CC BY NC SA: The CC BY-NC-SA license allows users to copy, to create extracts, abstracts and new works from the Article, to alter and revise the Article, provided this is not done for commercial purposes, and that the user gives appropriate credit (with a link to the formal publication through the relevant DOI), provides a link to the license, indicates if changes were made and the licensor is not represented as endorsing the use made of the work. Further, any new works must be made available on the same conditions. The full details of the license are available at http://creativecommons.org/licenses/by-nc-sa/4.0.